# Forward-Backward asymmetry in top pair production at the ILC

Muhammad Sohail Amjad

LAL 14-10

# Forward-Backward asymmetry in top pair production at the ILC.

par

M. Sohail Amjad

Université Paris-Sud 11

École Doctorale : Particules, Noyaux et Cosmos - ED 517

Laboratoire de l'accelérateur linéaire

Centre Scientifique d'Orsay, Bâtiment 200 - BP 34, 91898 Orsay CEDEX - France

**Discipline: Physique des Particules.**
**Directeur de thèse: M. Roman PÖSCHL (LAL)**

Thèse de doctorat pour obtenir le grade de

Docteur en Science de Université Paris-Sud 11

soutenue le **04 Février 2014**

devant le jury, composé de:

| | | |
|---|---|---|
| Prof. | Achille STOCCHI | Président du Jury |
| Prof. | Klaus DESCH | Rapporteur |
| Prof. | Hafeez HOORANI | Rapporteur |
| Prof. | Ben KILMINSTER | Examinateur |
| Prof. | Marcel VOS | Examinateur |
| Prof. | Francois RICHARD | Membre Invité |

*Dedicated to Prof. Abdus Salam* [1]

[1] The legendary Pakistani physicist, renowed for the electroweak theory.

# *Acknowledgements*

My biggest thanks will go to Prof. Achille Stocchi and Dr. Roman Pöschl, for welcoming me in LAL, and letting me complete my PhD. It would not have been possible without their guidance and support throughout the tough period of two years. I equally benefited from the wealth of experience, possessed by Prof. Francois Richard. He was very kind and gentle. The informal discussions, exchange of ideas with him and hints to proceed helped me along. I am also thankful to the jury members Prof. Hafeez Horrani, Prof. Klaus Desch, Prof. Marcel Vos and Prof. Ben Kilminster, for agreeing to judge my work. My group mates, Thibault Frisson, Jeremy Rouene, and Naomi van der Kolk were a cheerful group of guys to be with. The hard journey became very enjoyable in their company, and I owe a big thanks to all of them.

Outside the lab, the life wasn't an easy one, but was made pleasant by my friends and family. My parents and my sisters always helped me, encouraged me and supported me to keep going. It would not have been a successful venture, without all the love they poured upon me. My friends, whom I visited at 'Darbar e Luxembourg', were a precious company to gather all the energy I needed. Qasim Malik looked after me when I needed him the most. He was an inspiration, to learn a lot of things. He visited me when I was in bed, because of health problems, cooked for me, and stayed a night while combating the bed bugs. Mubeen Kamboh and Rana Iftikhar always treated me like younger brother. During my language course at Royan, I had a wonderful time with Kashif Bhatti and Zulfiqar Umrani. It was during that stay, that Khurram Yaqoob became a close buddy of mine. I shared many troublesome events with Yousuf Raza, who was always there to listen to me. It would take an immensely long story to thank the people like Abdul Wahab Malik, Qasim Raza and Junaid Ali Khan. Asad Hussain, Iftikhar Chaudhary, Asif Niazi, Qamar Saeed and Anzar Khaliq deserve hearitest thanks for being such good mates. What more could I miss than the very short discussion and company with Maqsood Gill, Bushra Maqsood and Soha Maqsood. The cheerful family brought a lot of cheers, whenever I saw them.

The expression of gratitude will only be complete, when I thank my always caring, helpful, and supportive Dr. Tehreem Ali. All the stress of work, my bad evenings and good days, my little successes and short term problems, and the consequences of a harsh day reflecting in my bad mood were shared by her. I would never have been there, without her. On the day of my thesis defense, the person I missed the most was her. If anybody is the happiest of my achievement, it's she, and I wish to share all the happiness in future, with her.

# *Abstract*

This thesis is done in the framework of the ILC. The determination of the electroweak couplings of the top quark, is one of the tasks at the ILC. The thesis is dedicated to the measurement of the Forward-backward asymmetry in top quark pairs, at 500 GeV, using two beam polarization configurations, in the fully hadronic decay channel. The top quark almost exclusively decays to a $b$ quark and a $W$ boson. The 6 jet final state is analyzed using full detector simulation. Two jets with highest b-tag are taken as $b$ jets and the remaining four jets are used to reconstruct the $W$s. The identification of the top and anti-top quarks is done by using the vertex charge of the $b$ quark. Precisions on the production cross sections are also calculated. It is found that using these parameters, the ILC will be capable of measuring the electroweak couplings of top quark, with a precision of less than 0.5%.

This thesis also includes a chapter on the optimization of the Si-W Electromagnetic calorimeter of the International Large Detector (ILD), one of the two detectors at the ILC. The ECAL of ILD, will consist of alternate layers of Silicon and Tungsten, where Silicon layers are active layers, while Tungsten is passive material. The Silicon layers are divided into wafers, surrounded by guard rings, to avoid the leakage currents. The analysis is focused to optimize the guard ring size. The results indicate that a guard ring of size up to 2mm, does not degrade the energy resolution performance of ECAL, considerably.

The thesis is divided into 6 chapters. The first chapter gives a brief over view of the Standard Model and emphasis on the need of a lepton collider for precision measurements. The second chapter is dedicated to the theoretical aspects of the top quark physics at the ILC. A detailed description of the ILD and its sub-detectors is given in the 3rd chapter. The 4th chapter presents the studies of the optimization of Si-W ECAL guard ring size. The 5th chapter contains the details of analysis of $t\bar{t}$ production at ILC, the measurement of the $A^t_{FB}$ and cross section $\sigma_{t\bar{t}}$. The last chapter contains summary of the results.

# Contents

**Acknowledgements** iv

**Abstract** vi

**1 Standard Model** 1
- 1.1 Introduction . . . 1
- 1.2 Interactions in the Standard Model . . . 3
  - 1.2.1 Electromagnetic Interactions . . . 4
  - 1.2.2 Strong Interactions . . . 4
  - 1.2.3 Electroweak Interactions . . . 5
- 1.3 Higgs Physics . . . 7
  - 1.3.1 Spontaneous Symmetry Breaking . . . 7
  - 1.3.2 Higgs Mechanism . . . 8
  - 1.3.3 Two Higgs Doublet Models (2HDM) . . . 10
- 1.4 Open Questions in Particle Physics . . . 12
- 1.5 Motivation for a lepton collider . . . 13

**2 Top quark physics at the ILC** 17
- 2.1 Introduction . . . 17
- 2.2 Searches and Discovery of the top quark . . . 18
  - 2.2.1 Properties of Top Quark . . . 18
- 2.3 Electroweak couplings of top quark . . . 21
- 2.4 Cross sections . . . 24
- 2.5 Forward Backward Asymmetry . . . 25

**3 International Large Detector (ILD)** 28
- 3.1 Introduction . . . 28
- 3.2 The International Linear Collider . . . 28
- 3.3 The Particle Flow Algorithm (PFA) . . . 30
- 3.4 The ILD detector concept . . . 31
  - 3.4.1 Vertex Detectors (VTX) . . . 31
  - 3.4.2 Central Tracking . . . 33
    - 3.4.2.1 Silicon Tracking . . . 34
    - 3.4.2.2 The Time Projection Chamber (TPC) . . . 35
  - 3.4.3 The ILD Calorimeter System . . . 36
    - 3.4.3.1 The Silicon Tungsten Electromagnetic Calorimeter (Si-W ECAL) . . . 37

3.4.3.2 Alternatives for ECAL . . . 39
3.4.3.3 The Hadronic Calorimeter (HCAL) . . . 39
3.4.4 The Magnetic Coil and The Muon Chamber . . . 41
3.5 Softwares and tools. . . . 42

**4 Optimization of the Si-W ECAL guard ring size 43**
4.1 Introduction . . . 43
4.2 Motivation . . . 44
4.3 Optimization studies of the guard rings . . . 46
4.4 Wafer Scan . . . 46
4.5 Physics Channels at the ILC . . . 48
4.5.1 $Z \to q\bar{q}$ Jets at 91 GeV . . . 49
4.5.2 $Z \to e^-e^+$ Channel. . . . 51
4.6 Summary . . . 53

**5 Top quark forward backward asymmetry at the ILC 55**
5.1 Introduction . . . 55
5.2 Asymmetries at hadron colliders . . . 55
5.3 Asymmetries at the ILC . . . 56
5.4 Production cross sections at the ILC and beam polarizations. . . . 57
5.5 Studies . . . 59
5.6 LCFIPlus . . . 60
5.7 Analysis and Kinematic Cuts . . . 61
5.8 Standard Model background . . . 65
5.9 Charge of the b quark . . . 66
5.9.1 Quality of the charge reconstruction . . . 67
5.9.2 $\gamma\gamma$ background . . . 67
5.10 Mis-tagging of $c$-jets as $b$-jets . . . 69
5.11 Identification of top quarks . . . 71
5.12 Determination of the forward backward asymmetry $\mathbf{A_{FB}^t}$ . . . 74
5.13 Form Factors . . . 76
5.14 Discussion of results . . . 78

**6 Summary and outlook 81**
6.1 The optimization of Si-W ECAL . . . 81
6.2 Forward-backward asymmetry in top quark pairs . . . 82

**A Vertex Charge 84**

# Chapter 1

# Standard Model

## 1.1 Introduction

The Standard Model (SM) is the most comprehensive description of elementary particles and their laws of interactions in the world of particle physics today. Along with explaining the properties of already discovered particles, it has made deeply tested predictions over the years. The model has an excellent success in describing the building blocks of matter. According to the model, matter is made up of fermions, spin 1/2 particles which interact via bosons. According to current knowledge, these fermions are elementary particles and they are further classified into leptons and quarks, depending on the type of interaction, in which they take part. There are six leptons and six quarks which are grouped into three doublets. The leptons and some of their properties are given in the table below,

| Family | Particle | L | B | $Q_e$ | Mass |
|---|---|---|---|---|---|
| $1^{st}$ | e | 1 | 0 | -1 | 511keV |
| | $\nu_e$ | 1 | 0 | 0 | $<$2eV |
| $2^{nd}$ | $\mu$ | 1 | 0 | -1 | 105.66 MeV |
| | $\nu_\mu$ | 1 | 0 | 0 | $<$0.19MeV |
| $3^{rd}$ | $\tau$ | 1 | 0 | -1 | 1.78GeV |
| | $\nu_\tau$ | 1 | 0 | 0 | $<$18.2MeV |

TABLE 1.1: Currently known leptons, in the framework of the Standard Model, along with their properties.

where L,B and $Q_e$ represent lepton number, baryon number and electric charge respectively. The following table lists the quark doublets and their properties,

The numbers represented here, are taken from [24].

| Family | Particle | L | B | $Q_e$ | Mass |
|---|---|---|---|---|---|
| $1^{st}$ | u | 0 | 1/3 | 2/3 | 2.3 $^{+0.7}_{-0.5}$ MeV |
| | d | 0 | 1/3 | -1/3 | 4.8 $^{+0.5}_{-0.3}$ MeV |
| $2^{nd}$ | c | 0 | 1/3 | 2/3 | 1.275 ±0.025 GeV |
| | s | 0 | 1/3 | -1/3 | 95±5 MeV |
| $3^{rd}$ | t | 0 | 1/3 | 2/3 | 173.07 ±0.52 GeV |
| | b | 0 | 1/3 | -1/3 | 4.18 ±0.018 GeV |

TABLE 1.2: Currently known quarks in the Standard Model. The masses represented here are their constituent masses, as the free quarks do not exist.

| Interaction | Particle | Charge(electric) | Spin | Mass (GeV/c$^2$) |
|---|---|---|---|---|
| Weak | Z | 0 | 1 | 91.2 |
| | $W^{\pm}$ | ±1 | 1 | 80.4 |
| E.M | $\gamma$ | 0 | 1 | 0 |
| Strong | $g$ | 0 | 1 | 0 |

TABLE 1.3: Gauge bosons of the Standard Model, and their properties. The respective interactions of which these bosons are mediators, are also shown.

Leptons and quarks interact through force carrier particles. These particles, also called the mediators, are spin 1 particles or gauge bosons. The gauge bosons are summarized here.

The elementary particles can be summarized in pictorial form, as presented in figure 1.1.

The interactions among these particles are divided into three types;

- Electromagnetic interactions are described by Quantum Electrodynamics (QED). The photon ($\gamma$) is the mediator of this interaction.
- The weak interaction is the one in which all fermions take part. The associated gauge Bosons are $W^{\pm}$ and $Z$.
- Quarks and gluons interact through the strong interaction as they carry a color charge. Gluons are the mediators of the strong interaction and are self-interacting as well. This interaction is described by Quantum Chromodynamics (QCD).
- The Standard Model is completed by the Higgs boson, that couples to all massive particles.

Currently, the Standard Model does not incorporate gravity, though it is regarded as one of the fundamental forces of Nature.

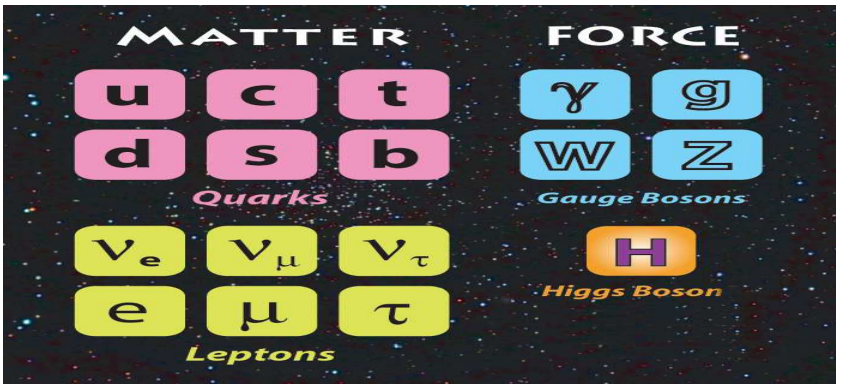


FIGURE 1.1: Elementary particles of the Standard Model. The recently discovered Higgs boson is also included.

## 1.2 Interactions in the Standard Model

asym Quantum Field Theory (QFT) is the mathematical basis of the Standard Model. The equations of QFT are obtained by the principle of least action and gauge symmetries.

In the Standard Model, a Lagrangian describes the dynamics of a particular interaction. The particles taking part in that interaction are represented as dynamical fields in space-time. Generally this Lagrangian $\mathcal{L}$ is a function of fields and of their derivatives.

The fermion fields, which represent matter particles, are represented by $\psi$, which can be further decomposed to left and right parts as follows;

$$\psi^{Left} = \frac{1}{2}(1-\gamma_5)\psi\psi^{Right} = \frac{1}{2}(1+\gamma_5)\psi \tag{1.1}$$

Here $\gamma_5$ is the 5th gamma matrix. $(1 \pm \gamma_5)$ is the Chirality operator. Under the weak Isospin $SU(2)$ transformation, the left-handed particles are weak Isospin doublets, while the right-handed particles are singlets.

The mathematical model is gauge invariant and is based on $SU(3)_C \otimes SU(2)_L \otimes U(1)_Y$ symmetry. Here $SU(2)_L \otimes U(1)_Y$ represents the electroweak symmetry; $SU(2)_L$ is the weak Isospin symmetry group and $U(1)_Y$ is the component for weak hypercharge symmetry. The weak hypercharge $(Y)$ is defined as

$$Q = I_3 + \frac{1}{2}Y, \tag{1.2}$$

where $I_3$ is the third component of $SU(2)_L$ Isospin, and Q is the electric charge. $I_3 = \pm 1/2$ for left-handed fermions, while $I_3 = 0$ for right-handed fermions. $SU(3)_C$ represents the color symmetry group which is related to strong interactions.

The Standard Model is a chiral theory, as the Lagrangian contains only massless fields. The particles of left Chirality are treated differently, by gauge interactions, from the ones of right Chirality. The interactions in the framework of the Standard Model are described in this chapter.

### 1.2.1 Electromagnetic Interactions

The laws of electromagnetic interactions are described by QED [8]. The simple Lagrangian for this interaction, involving a fermion field $\psi$ and a massless photon field $A_\mu$, can be written as,

$$\mathcal{L}_{QED} = \bar{\psi}(i\gamma^\mu D_\mu)\psi - \frac{1}{4}F_{\mu\nu}F^{\mu\nu} \tag{1.3}$$

Where $D_\mu = \partial_\mu - iQeA_\mu$ is the covariant derivative, with e the electric charge and $A^\mu$ is the covariant four-potential of the electromagnetic field. $\gamma^\mu$ are the Dirac matrices and $F_{\mu\nu} = \partial_\mu A_\nu - \partial_\nu A_\mu$ is the electromagnetic field tensor. QED is an abelian gauge theory with the symmetry group U(1), which implies that the photon is not a self-interacting particle. The photon itself does not carry any electric charge.

The strength of the electromagnetic field is expressed by the running coupling constant $\alpha$, whose value depends on the momentum transfer during the interaction. The value for zero momentum transfer is $\alpha = \frac{e^2}{4\pi\epsilon_0} \simeq \frac{1}{137}$.

### 1.2.2 Strong Interactions

QCD [9], the non-abelian gauge theory, is the mathematical formulation which describes the strong interaction among quarks and gluons. The theory is represented by $SU(3)_c$ group and because it is a non-abelian theory, gluons can self interact. Unlike the photons, which carry no electromagnetic charge, gluons carry color charge themselves. There are 3 color charges, carried by quarks and gluons.

The gauge invariant Lagrangian of QCD for a quark field q, can be written as following,

$$\mathcal{L}_{QCD} = \bar{q}(i\gamma^\mu D_\mu)q - \frac{1}{4}G^a_{\mu\nu}G^{\mu\nu}_a \tag{1.4}$$

Here $D_\mu = \partial_\mu - ig_s T_a G^a_\mu$ is the covariant derivative and q is a massless quark field, interacting via the gluon field $G^a_\mu, a = (1, 2, 3...8)$. $T_a$ are the generators of SU(3) and $g_s$ is the dimensionless coupling strength, analogous to 'e' in QED. Both fields are expressed in SU(3) representation. $G_{\mu\nu}$ is the QCD analog of $F_{\mu\nu}$ in QED, and is called the strong field tensor. It can be expressed as $G^a_{\mu\nu} = \partial_\mu G^a_\nu - \partial_\nu G^a_\mu + g f^{abc} G^b_\mu G^c_\nu$, where $f^{abc}$ are the structure constants of SU(3).

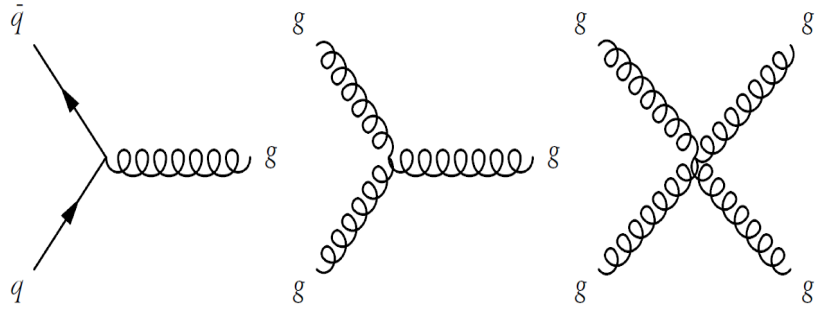


FIGURE 1.2: Vertices of the QCD, at the tree level. The quark-quark, quark-gluon and gluon-gluon couplings are represented in terms of Feynman diagrams.

The behavior of the strong coupling constant $\alpha_s = \frac{g^2}{4\pi}$ is different than that of the electromagnetic coupling constant. The force present between two quarks is smaller at a smaller distance but it increases by increasing the distance between them, prohibiting the existence of free quarks. The energy used to separate the quarks, is converted into $q\bar{q}$ pairs. This phenomenon is called "confinement". It implies that the quarks interact with other quarks to form hadrons (except the top quark). This is called "hadronization". The hadrons are color neutral and can be classified as mesons or baryons depending on their spin. Mesons are bosons, consisting of $q\bar{q}$ pairs, for example pions $(\pi^+, \pi^-, \pi^0)$. Baryons are fermions consisting of $qqq$, for example protons $(uud)$ and neutrons $(udd)$. The other distinct feature of QCD is "asymptotic freedom", which implies that at high energies (small distances), quarks propagate as free particles. The basic interactions of QCD are shown in figure 1.2.

### 1.2.3 Electroweak Interactions

Abdus Salam[7], Sheldon Glashow[5], and Steven Weinberg [6] unified the electromagnetic and weak interaction, calling it the electroweak interaction [1]. The experimental verification of the theory came through the discovery of neutral currents in 1973 [2] and later with the discovery of the W and Z bosons at the Super Proton Synchrotron (SPS) in 1983.

To start with, the $\beta$ decay is described by the Fermi theory, which conserves the parity. The parity violation was observed by Madame Wu [38], observing a correlation between direction of electrons and spin of neucleus. This correlation was interpreted as electron being left-handed, thus violating the Parity. The $V-A$ theory was developed by Feynman and Gell-Mann in 1958. It treats the neutrinos as massless particles, and takes the parity violation into account. It modifies the Fermi theory by subtracting the axial vector

current from the vector current. For example, the neutrino part in the Fermi theory is replaced as

$$\bar{e}(x)\gamma_\mu\nu_e(x) \longrightarrow \bar{e}(x)\gamma_\mu\frac{1}{2}(1-\gamma_5)\nu_e(x) \tag{1.5}$$

$$= \underbrace{\frac{1}{2}\bar{e}(x)\gamma_\mu\nu_e(x)}_{\text{Vector Current}} - \underbrace{\frac{1}{2}\bar{e}(x)\gamma_\mu\gamma_5\nu_e(x)}_{\text{Axial Vector Current}} \tag{1.6}$$

$$= \frac{1}{2}\left(V_\mu^{(e)}(x) - A_\mu^{(e)}(x)\right). \tag{1.7}$$

$$\tag{1.8}$$

The Standard Model electroweak theory is described by the $SU(2)_L \otimes U(1)_Y$ symmetry group. It contains three massless bosons $W^i, i = (1,2,3)$, associated with SU(2) and 1 massless boson associated with U(1). The Lagrangian for these bosons can be written as,

$$\mathcal{L}_{EW} = -\frac{1}{4}W^{i\mu\nu}W^i_{\mu\nu} - \frac{1}{4}B^{\mu\nu}B_{\mu\nu} + \bar{\psi}i\gamma^\mu D_\mu\psi \tag{1.9}$$

Here $B^{\mu\nu} = \partial_\mu B_\nu - \partial_\nu B_\mu$ and $W^{i\mu\nu} = \partial_\mu W_\nu - \partial_\nu W_\mu - g\vec{W}_\mu \times \vec{W}_\nu$. They are field strength tensors for weak hypercharge $Y$ and Isospin $I_L$ respectively. $D_\mu$ is the covariant derivative which can be expressed as,

$$D_\mu = \partial_\mu + i\frac{g}{2}\tau_j W^j_\mu + 2ig'YB_\mu \tag{1.10}$$

where $g'$ and $g$ are the coupling constants related to fields $B$ and $W_j, j = (1,2,3)$, respectively. The $\tau_j$ are Pauli spin matrices in $SU(2)_L$ space as given below,

$$\tau_1 = \begin{pmatrix} 0 & 1 \\ 1 & 0 \end{pmatrix}, \tau_2 = \begin{pmatrix} 0 & -i \\ i & 0 \end{pmatrix}, \tau_3 = \begin{pmatrix} 1 & 0 \\ 0 & -1 \end{pmatrix}. \tag{1.11}$$

The W boson can be obtained from the W fields as following,

$$W^{\mu\pm} = \frac{W_1^\mu \mp iW_2^\mu}{\sqrt{2}} \tag{1.12}$$

To obtain the Z boson ($Z^\mu$) and photon ($A^\mu$) fields we introduce the weak mixing angle $\theta_W$ and the following combinations of $W_3^\mu$ and $B^\mu$ ;

$$Z^\mu = \cos\theta_W W_3^\mu - \sin\theta_W B_\mu \tag{1.13}$$

$$A^\mu = \sin\theta_W W_3^\mu + \cos\theta_W B_\mu \tag{1.14}$$

The couplings of fermions to Z boson are given as,

$$\frac{|q_f|(I_3^f - Q\sin^2\theta_W)}{\sin\theta_W\cos\theta_W} \tag{1.15}$$

$|q_f|$ denotes the fermion charge and $I_3$ is the third component of Isospin. The term $Q\sin^2\theta_W$ allows the coupling of the Z boson to charged right-handed fermions, which is not the case for pure $SU(2)_L$ couplings. The vector and axial vector currents behave differently under the parity transformation. The Z boson couples to the right and left-handed handed fermions while the W boson, also called the charged currents, couples to left-handed fermions only. The W boson makes flavor changing interactions possible in electroweak sector, through the CKM mechanism [3, 4].

The theory is non-abelian like QCD, due to the interaction between Ws.

## 1.3 Higgs Physics

So far, we have considered massless fields while in fact the gauge bosons, $W^{\pm}$ and $Z$, as well as fermions are massive. Mass terms like $m\psi\bar{\psi}$ are forbidden because they do not transform as scalars under $SU(2)_L \otimes U(1)_Y$. The other option of gauge terms, $\frac{1}{2}m_A^2 A_\mu A^\mu$, violates the gauge invariance of the Lagrangian. The mass of fermions and bosons can be generated by spontaneous symmetry breaking and the Higgs Mechanism [10].

### 1.3.1 Spontaneous Symmetry Breaking

The Lagrangian, for a scalar field $\phi$, can be written as:

$$\mathcal{L}_\phi = T - V(\phi) = \frac{1}{2}(\partial_\mu\phi)^2 - (\frac{1}{2}\mu^2\phi^2 + \frac{1}{4}\lambda\phi^4) \tag{1.16}$$

The potential $V(\phi) = \frac{1}{2}\mu^2\phi^2 + \frac{1}{4}\lambda\phi^4$ has a minimum if $\lambda > 0$. The position of this minimum depends on the sign of $\mu^2$.

If $\mu^2 > 0$: this Lagrangian describes a scalar particle with mass $\mu$ and a quartic self coupling. The ground state, $\phi = 0$, respects the transformation $\phi \to -\phi$. This solution is called symmetric, and it is shown in the left part of figure 1.3.

When $\mu^2 < 0$: there is a whole circle of minima in $V(\phi)$, with a radius $\phi = \pm(\sqrt{-2\mu^2/\lambda})$ as shown in the right part of figure 1.3. The $\mu$-term is not a mass term anymore. And it is with this solution, that we can see spontaneous symmetry breaking.

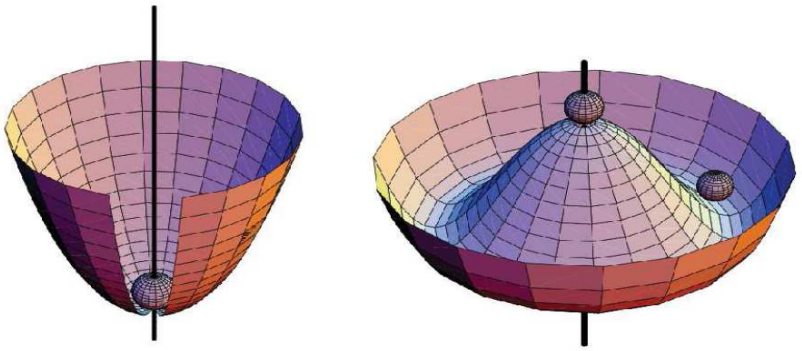

FIGURE 1.3: The potential $V(\phi)$ for two possible solutions with $\mu^2 > 0$ (left) and $\mu^2 > 0$ (right). The image is taken from [11].

### 1.3.2 Higgs Mechanism

The Higgs Mechanism works by applying spontaneous symmetry breaking to a local gauge symmetry. For a complex scalar field Isospin doublet,

$$\phi = \begin{pmatrix} \phi^+ \\ \phi^0 \end{pmatrix} \tag{1.17}$$

the electroweak sector Lagrangian excluding fermions, can be written as:

$$\mathcal{L}_\phi = D_\mu \phi^\dagger D_\mu \phi + \mu^2(\phi\phi^\dagger) - \frac{\lambda}{4}(\phi\phi^\dagger)^2 - \frac{1}{4}W^{i\mu\nu}W^i_{\mu\nu} - \frac{1}{4}B^{\mu\nu}B_{\mu\nu} \tag{1.18}$$

The minimum is at $(\phi^\dagger\phi) = -v^2/\lambda$. We can expand around this minimum by taking

$$\phi(x) = \begin{pmatrix} 0 \\ \frac{v+H(x)}{2} \end{pmatrix} \tag{1.19}$$

Substituting this value of $\phi(x)$ to eq. 1.18 and using $D_\mu = \partial_\mu + i\frac{g}{2}\sigma_j W^j_\mu + 2ig'YB_\mu$ , we get;

$$\mathcal{L}_\phi = \frac{1}{2}(\partial_\mu H \partial^\mu H) - \mu^2 H^2 \tag{1.20}$$

$$-\frac{1}{4}(\partial_\mu W_{i\nu} - \partial_\nu W_{i\mu})(\partial^\mu W_i^\nu - \partial^\nu W_i^\mu) \tag{1.21}$$

$$+\frac{1}{8}g^2v^2(W_{1\mu}W^{1\mu} + W_{2\mu}W^{2\mu}) \tag{1.22}$$

$$+\frac{1}{8}v^2(gW_{3\mu} - g'B_\mu)(gW_3^\mu - g'B^\mu) - \frac{1}{4}B_{\mu\nu}B^{\mu\nu} \tag{1.23}$$

$$\tag{1.24}$$

The first two components of the W field have quadratic terms which implies that these fields are massive with mass $M_W = \frac{gv}{2}$. The third component of the W field mixes with

the B field. This equation can be further expanded using equations 1.12-1.14, to show that 5 bosons appear in the Lagrangian. The theory, thus, predicts the existence of a massive boson, famously known as Higgs boson, a candidate to which has recently been discovered at the LHC [35, 36], at a mass around 126 GeV.

The discovery marked an excellent success of the LHC, and is is the biggest discovery in the domain of the particle physics, in last two decades, after the discovery of the top quark. The two experiments at the LHC, ATLAS and CMS, simultaneously announced the observation of Higgs-like boson. The CMS observed a mass of $125.3 \pm 0.4(stat.) \pm 0.5(syst.)$ GeV [35] and ATLAS reported the mass to be $126.0 \pm 0.4(stat) \pm 0.4(sys)$ GeV [36]. Figure 1.4 shows the respective plots from the two experiments.

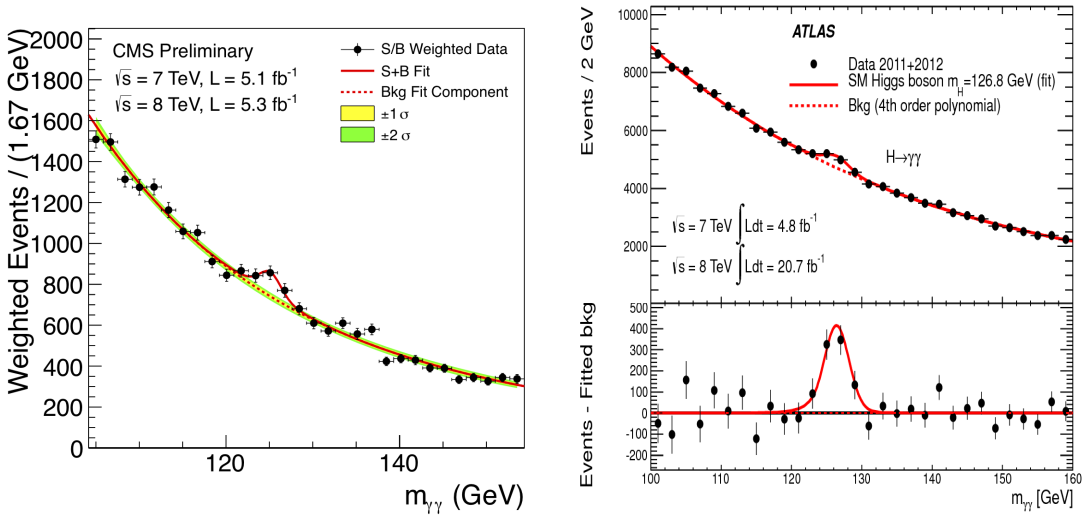


FIGURE 1.4: Left Di-photon ($\gamma\gamma$) invariant mass distribution for CMS data taken in 2011 and 2012 [35]. Right The same from the ATLAS experiment for $\sqrt{s} = 7$ TeV and $\sqrt{s} = 8$ TeV combined [36].

The discovery of a low-mass Higgs implies further precise studies of Higgs boson. One of the areas where the hint of new physics could be found, is the Higgs boson couplings to Standard Model particles. Existence of new particles will modify these couplings and the measurements could diverge from the Standard Model predictions.

Figure 1.5 shows the order of the couplings of the Higgs boson to different particles, including the top quark, which feature in the physics program of the ILC, a future linear collider.

This low mass of the Higgs boson has several implications. One of the major problems it brings is the Hierarchy problem. The scalar field $\phi$ presented in equation 1.16, has a value

$$\langle \phi \rangle = \sqrt{\frac{m_H^2}{2\lambda}}, \tag{1.25}$$

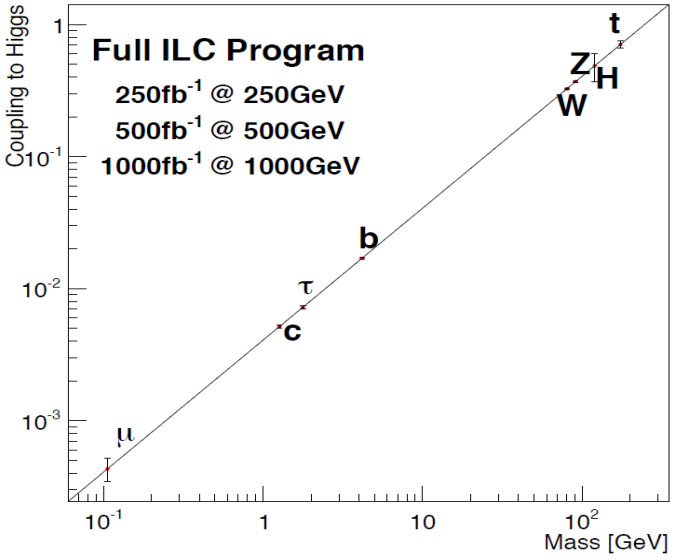


FIGURE 1.5: Higgs boson couplings to different Standard Model particles, as to be measured at the ILC. A precise determination of these couplings could hint at any divergences from the Standard Model predictions, and existence of new physics [40].

where $\mu^2$ has been replaced by $m_H^2$. Since we know experimentally that $<\phi>$ is around 246 GeV, the quantity $m_H^2$ is of the order of (100 GeV) $^2$. The problem with that is that $m_H^2$ receives radiative corrections from all the particles, to which it couples. For example the corrections from a fermion $f$, of mass $m_f$ and coupling to Higgs $\lambda_f$, could be written as [16]:

$$\Delta m_H^2 = -\frac{|\lambda_f|^2}{8\pi^2}\Lambda_{UV}^2 + ... \tag{1.26}$$

Where $\Lambda_{UV}$ is the ultraviolet cut-off, which can be interpreted as the scale to which the Standard Model is valid or a scale at which the effects of new physics appear. If the Standard Model is to be valid upto the Planck scale, the corrections to the $m_H^2$ are around 30 order of the magnitude higher than the required value of -(100 GeV) $^2$. This problem only occurs for the corrections to the mass of Higgs boson, as the masses of fermions and gauge bosons do not have a direct quadratic sensitivity to the $\Lambda_{UV}$. However, they do have an indirect dependence on this parameter, as all the particles in Standard Model, obtain their masses via the interaction to the Higgs boson.

### 1.3.3 Two Higgs Doublet Models (2HDM)

Some solutions have been proposed to solve this problem. Conformal solution [12], within the framework of the Standard Model, and extra dimensions solution [13] are a few options along with the composite Higgs models [14], as in technicolor models [15].

Another solution is Supersymmetry. Here the focus will be on the Two Higgs Doublet Model (2HDM), which can be incorporated in Minimal Supersymmteric extension of the Standard Model (MSSM)[34].

Lets suppose, there exists a complex scalar S, with mass $m_S$ and it couples to Higgs with a Lagrangian term $-\lambda_S|H|^2|S|^2$. Then the correction to $m_H$ could be rewritten as [16]:

$$\Delta m_H^2 = \frac{\lambda_s}{16\pi^2}\left[\Lambda_{UV}^2 - 2m_S^2 \ln\left(\frac{\Lambda_{UV}}{m_S}\right) + ...\right]. \tag{1.27}$$

Note that the contribution becomes positive here because of the fact the fermions will have a negative contribution and bosons a positive one. In turn, the total contribution to the mass will be zero. There are two types of 2HDMs: Type I and Type II, where the two Higgs doublets couple differently. For example in Type I, one doublet couples to the quarks, and the other doesn't. While in Type II, one Higgs doublet may couple to up type quarks, and other to down type quarks. This possibly could explain the mass hierarchy between the $b$ and $t$ quarks. If both of the quarks, obtain their mass via the coupling to the single Higgs doublet, as is the case in Standard Model, it will be difficult to explain this anomaly. On the other hand, if the top quark couples to different Higgs doublet, the hierarchy could be explained.

The Higgs sector of the Minimal Supersymmetric Standard Model (MSSM) is a constrained Type II 2HDM. The two Higgs doublets can be written as follows:

$$H_1 = \begin{pmatrix} H_1^0 \\ H_1^- \end{pmatrix}, \quad H_2 = \begin{pmatrix} H_2^+ \\ H_2^0 \end{pmatrix}, \tag{1.28}$$

The electroweak symmetry is broken when the neutral components of these Higgs fields obtain a vacuum expectation value. The combination of the VEVs is constrained by the following condition:

$$2(\langle H_1^0\rangle^2 + \langle H_2^0\rangle^2) \equiv v^2 \simeq (246GeV)^2 \tag{1.29}$$

But their ratio is not confined and is defined as:

$$\tan\beta = \langle H_2^0\rangle / \langle H_1^0\rangle \tag{1.30}$$

Where $\langle H_2^0\rangle$ and $\langle H_1^0\rangle$ are the vacuum expectation values of the neutral Higgs boson, which couples to $u$ type and $d$ type fermions, respectively. The factor $\tan\beta$, is a free parameter of the SUSY. The searches for SUSY are carried out for different values of $\tan\beta$.

Due to SUSY breaking, that enters in the loops, there are radiative corrections to the tree-level structure of the model. In particular, the effective Lagrangian that describes

the coupling of the Higgs bosons to the third generation quarks, is modified by the Yukawa vertex corrections.

## 1.4 Open Questions in Particle Physics

The Standard Model had excellent success, ever since it started as the fundamental theory for particle physics. The successful predictions of electroweak theory, of existence of gauge bosons $W$ and $Z$, the discovery of third family of quarks, predicted using CKM mechanism, and Higgs boson, the latest feather in the crown of Standard Model, make it a successful model. Precision studies has been carried over various experimental facilities. A recent summary of electroweak precision results, after the discovery of Higgs boson, is shown in the figure 1.6.

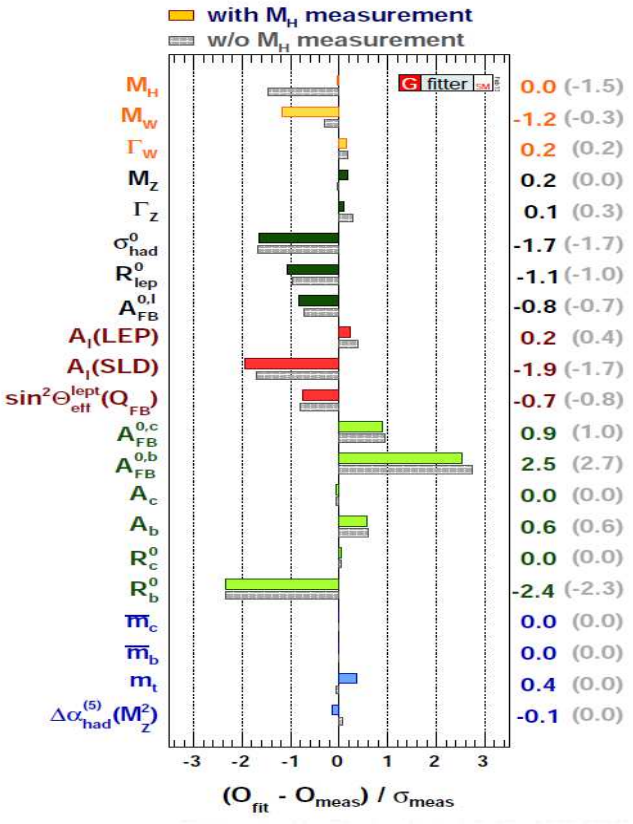


FIGURE 1.6: The figure shows the difference between the measured values of SM parameters, and the predicted values, in units of uncertainty for the fit. The color lines represent the values with mass of the Higgs boson $m_H$, while gray lines are without $m_H$. The image is taken from [33]

.

Despite its success, there are problems which are not understood in the framework of the Standard Model. It has not been able to explain the mass hierarchies in, e.g. the

quark sector. The heaviest quark $t$ is 35 times heavier than the next heavier quark $b$, which happens to be it's Isospin doublet partner as well. This difference of masses is not explained in the Standard Model.

The masses of the particles are introduced by the spontaneous symmetry breaking, as explained previously. The reason for the EWSB is unknown in the framework of the Standard Model. Also, the radiative corrections to the Higgs mass, which depend on top quark mass particle, are larger than the actual Higgs mass. Which implies that the Higgs mass parameter has to be fine-tuned, in order to cancel the quantum corrections.

Another missing explanation from the Standard Model is baryon-anti baryon asymmetry. In the observed universe, it has been found that the quantity of baryonic matter exceeds that of antibaryonic matter by large amount. The Standard Model does not offer any valid explanation for this discrepancy. Though the CP violation proposal is under study, but the Standard Model CP violation is not sufficient is not sufficient to explain the excess of matter.

One of the most important elements, needed to explain the universe is Gravity. The Standard Model does not incorporate a quantum field theory for gravity. Though the possible existence of Graviton, candidate for carrier of gravitational force, is postulated, it remains unobserved.

Related to the Gravitation and astroparticle physics, is another problem of dark matter. The observed rotation of galaxies and the amount of matter observed are not compatible. The solution proposed to this problem is existence of the dark matter. A candidate for the dark matter is missing in the framework of the Standard Model.

The inclusion of gravity to the fundamental interactions will require an explanation for the mass hierarchy. The gravitational mass scale is $1/\sqrt{G} \simeq 10^{19}$ GeV, where G is the Newton constant, while typical masses of electroweak bosons are $\sim 100$ GeV. Another way of looking at the hierarchy problem is that if there exists a Grand Unification Symmetry, it is broken at a scale of $10^{16}$ GeV, while electroweak symmetry is broken at 100 GeV, which is a difference of 14 orders of magnitude.

## 1.5 Motivation for a lepton collider

After the discovery of a Higgs-like boson, important parameters to be studied are the its production cross section, a precise determination of the mass of the Higgs boson ($m_H$), its branching ratios and couplings to other Standard Model particles. The Higgs couplings to other Standard Model particles are of the fundamental importance towards

the discovery of any new physics. The precise determination and any deviation from the Standard Model predictions, could well hint at the possible role of Higgs in new physics.

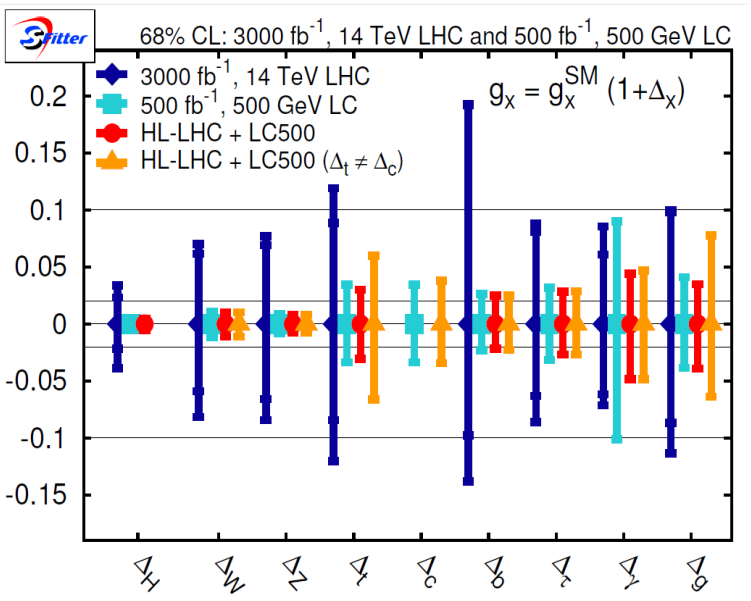


FIGURE 1.7: Comparison of ILC and LHC, for measurements of precision of Higgs couplings to different particles. The plot shows a comparison of precisions (from left to right) of LHC, ILC and High Luminosity LHC, combined with ILC. The inner bars for HL-LHC denote a scenario with improved experimental systematic uncertainties. The image is taken from [56].

As already mentioned, the 2HDM proposes two Higgs doublets instead of one, as in the framework of the Standard Model. The confirmation of the nature of the Higgs boson will require a clean and precise determination of its couplings. Figure 1.7 shows the comparison of precision on couplings of Higgs boson to different particles, as attainable at LHC at nominal center-of-mass energy and the ILC, a proposed future linear collider. Apart from comparing the original precisions, a combination of the two is also shown.

The decay properties of the Higgs boson, make it difficult to precisely analyze all the decay channels at a hadron collider, with the difficulty of separating the decay to $q\bar{q}$ pairs, from the huge amount of QCD background. The model independent Higgs analysis at the ILC, is through the Higgs recoil method, $e^-e^+ \rightarrow HZ$[100]. Given that the ILC could operate at a center-of-mass energy of $\sqrt{s} = 250$ GeV, which corresponds to the peak cross section for the Higgs boson. The precise reconstruction of the $Z$ boson means that the Higgs reconstruction can be done precisely in any mode, including decay to quark pairs and invisible decays. It also provides opportunity to investigate the nature of the Higgs boson itself, including the compositness.

There is a large spectrum of physics processes which could be studied at a lepton collider. For example the two fermion $e^+e^- \rightarrow f\bar{f}$ process, which is of particular interest, at a

lepton collider. The cross section for such processes can be written as:

$$\frac{d\sigma}{d\cos\theta} = \frac{\pi\alpha^2}{2s}\left[A_+(1+\cos\theta)^2 + A_-(1-\cos\theta)^2\right] \tag{1.31}$$

Where the coefficients $A_+ = (1-P_{e^-})(1+P_{e^+})$, $A_- = (1+P_{e^-})(1-P_{e^+})$ depend on the beam polarizations. $P_{e^-}$ and $P_{e^+}$ are the polarization of electron and positron beam respectively.

The models with gravitation effect at TeV scale, propose modification to this cross section. One such example is Randall-Sundrum Models[49]. The proposed future linear collider, ILC, will also be capable of doing the precision measurements in WW, self Higgs coupling and could search for extended Higgs states. A brief summary of different processes, which could be studied at ideal center-of-mass energies, at ILC, is given in figure1.8.

| Energy | Reaction | Physics Goal |
|---|---|---|
| 91 GeV | $e^+e^- \to Z$ | ultra-precision electroweak |
| 160 GeV | $e^+e^- \to WW$ | ultra-precision $W$ mass |
| 250 GeV | $e^+e^- \to Zh$ | precision Higgs couplings |
| 350–400 GeV | $e^+e^- \to t\bar{t}$ | top quark mass and couplings |
| | $e^+e^- \to WW$ | precision $W$ couplings |
| | $e^+e^- \to \nu\bar{\nu}h$ | precision Higgs couplings |
| 500 GeV | $e^+e^- \to f\bar{f}$ | precision search for $Z'$ |
| | $e^+e^- \to t\bar{t}h$ | Higgs coupling to top |
| | $e^+e^- \to Zhh$ | Higgs self-coupling |
| | $e^+e^- \to \tilde{\chi}\tilde{\chi}$ | search for supersymmetry |
| | $e^+e^- \to AH, H^+H^-$ | search for extended Higgs states |

FIGURE 1.8: Tunable center-of-mass energy at ILC, enables study of different processes at nominal center-of-mass energies. The threshold energy makes it possible to precisely measure the mass, width and cross section of different Standard Model particles.

The chiral structure of the Standard Model makes the beam polarization a vital feature of the lepton collider, to study the precision physics. As is evident from the figure 1.6, that the measurement of $A_{FB}^{0,b}$ is $\sim 3\sigma$ away from the Standard Model prediction. The $A_{FB}^{0,b}$, is a relative measure of number b quarks, in forward hemisphere of the detector, as compared to that in backward hemisphere. The measurement of a higher than predicted value suggests that the coupling of the $Z$ boson to the heavy fermions could be modified. This modification could be further amplified while studying the $Zt\bar{t}$ couplings. Though the details on this will be given in 2.3, it is worth mentioning that the direct measurement of this coupling is not possible hadron colliders, due to a different production mechanism

of the top quark pairs. The coupling measurement is only possible through the associated boson production. On the other hand, at a linear collider, such as ILC, the production goes directly through the $Zt\bar{t}$ vertex. Apart from that, the availability of polarization makes it possible to study the helicity related parameters. Also the production cross section, the left-right and forward-backward asymmetry are variables sensitive to the beam polarization. All these measurements could lead to the understanding of electroweak coupling of the heaviest quark.

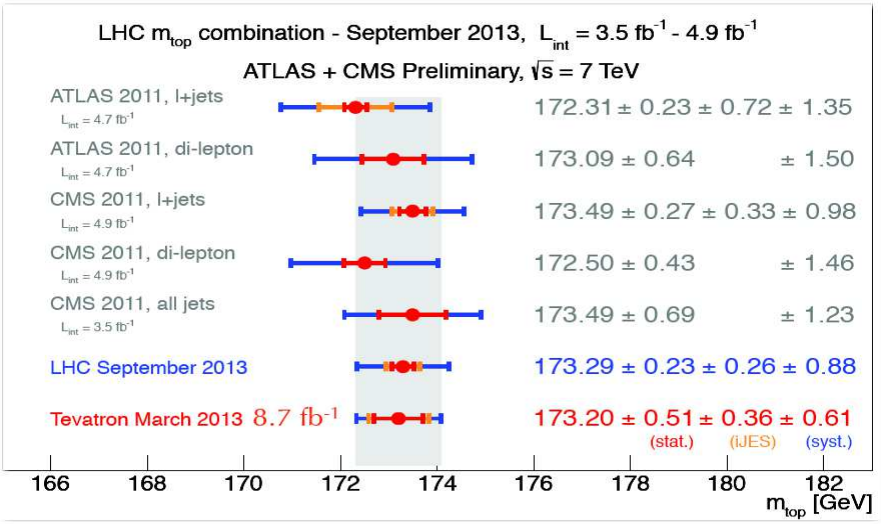


FIGURE 1.9: Recent results on the measurement of the top quark mass, from LHC.

The precise determination of the mass of the top quark, has been a subject of study at the particle colliders since its discovery. The efforts for a more and more precise determination are on going, and the recent results from the LHC experiments are shown in figure 1.9. A very precise determination of this parameter can be made using the top threshold physics. The linear collider operating at a center-of-mass energy of $\sqrt{s} = 2m_t$ provides an idea opportunity to precisely measure the mass $m_t$, width $\Gamma_t$ and production cross section $\sigma_{t\bar{t}}$ of the top quark.

# Chapter 2

# Top quark physics at the ILC

## 2.1 Introduction

The top quark is by far the heaviest known quark. It is much more massive than the other observed quarks and leptons. It is as massive, as a gold atom. A comparison of the mass of top quark, with other known quarks is shown in figure 2.1. In this chapter a review of top quark properties will be given, followed by a specific focus on top quark physics at linear colliders, specially ILC.

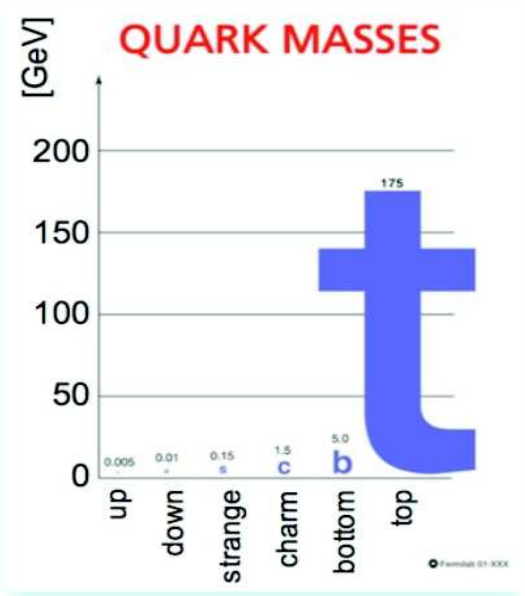


FIGURE 2.1: The mass of the top quark as compared to other quarks in the Standard Model. It is 35 times heavier then the next heavier quark $b$.

## 2.2 Searches and Discovery of the top quark

The existence of the third family of quarks was postulated by Makoto Kobayashi and Toshihide Maskawa [3]. Their prediction was heavily dependent on the GIM mechanism, devised by Glashow, Iliopoulos and Maiani in 1970 [26]. The charm quark was successfully predicted and discovered, through the discovery of $J/\psi$ mesons which is a $c\bar{c}$ bound state[18, 19]. This discovery confirmed the GIM mechanism and provided a lot of credibility to the the prediction of the third family. Soon after, the $\tau$ lepton was discovered at SLAC[17], confirming the existence of the third family of leptons. The discovery of the b quark did not take a long time. In 1977, $\Upsilon$, a $b\bar{b}$ bound state with a mass of 9.5 GeV, was discovered at Fermilab, confirming the existence of the b quark[20].

However, the discovery of the top quark was not that swift. The searches for top quark went on for a few years. One of the reasons for this was that the mass of the top quark could not be predicted in the framework of Standard Model. Search for the top quark began in the late 1970s, at SLAC and DESY, but it did not produce any hint of top quark production. The first searches were carried out at the lepton colliders. For example, at LEP, the indirect measurements put an an upper limit of 45.8 GeV, on the mass of top.The limiting factor for the searches at the lepton colliders was center-of-mass energy. In the 80s, with the start of hadron colliders, this problem was solved. The dominant mode of search initially was $W \rightarrow tb$, which put an upper limit of $\simeq 77GeV$ on the mass of the top quark.

In the early 1980s CERN also became involved through its Super Proton Synchrotron (SPS). In 1988, the experiments concluded that the mass of the top quark must be above 41 GeV. By the end of the decade this limit was pushed to 77 GeV as CERN came to its energy limits with $p\bar{p}$ collisions. The CDF and D0 collaboration at Fermilab, continued searching for the top quark. The D0 experiment started taking data in the beginning of 1992 and by the end of the year, the lower limit on the mass was pushed to 91 GeV. Finally in March 1995, both experiments simultaneously announced the discovery of the top quark [25, 30]. A summary of history of top quark search is given in the following table 2.1.

### 2.2.1 Properties of Top Quark

The top quark has a charge +2/3 and spin 1/2 but its most prominent property is its mass. It is the Isospin doublet partner of the $b$ quark. It acquires its mass via Yukawa couplings to the Higgs boson. There have been various studies to precisely determine the mass of the top quark. Currently the world average is $173.07 \pm 0.52 \pm 0.72GeV$ [24].

| Year | Collider | $\sqrt{s}$ | Beam | Mass Limit (GeV/c$^2$) |
|---|---|---|---|---|
| **Lepton Colliders** | | | | |
| 1979-84 | PETRA(DESY) | 12−46.8 GeV | $e^+e^-$ | >23.3 |
| 1987-90 | TRISTAN(KEK) | 61.4 GeV | $e^+e^-$ | >30.2 |
| 1989-90 | SLC (SLAC), LEP(CERN) | 91.2 GeV ($m_Z$) | $e^+e^-$ | >45.8 (indirect measurment) |
| **Hadron Colliders** | | | | |
| 1984 | SPS(CERN) | 630 GeV | $p\bar{p}$ | >45 |
| 1990 | SPS(CERN) | 630 GeV | $p\bar{p}$ | >69 |
| 1991 | TEVATRON(FNAL) | 1.8 TeV | $p\bar{p}$ | >77 |
| 1992 | TEVATRON(FNAL) | 1.8 TeV | $p\bar{p}$ | >91 |
| 1994 | TEVATRON(FNAL) | 1.8 TeV | $p\bar{p}$ | >131 |

TABLE 2.1: History of the discovery of the top quark, at various particle colliders. The colliders are classified into lepton and haron colliders.

The heavy mass of the top quark implies a short life time, which is of the order of $0.5 \times 10^{-24}$ sec. This life time is smaller than the time needed for the formation of QCD bound states, which is $1/\Lambda_{QCD} \simeq 3 \times 10^{-24}$ sec. So, unlike the other quarks, there do not exist any $t\bar{t}$ bound states. The top quark does not hadronize either, so there do not exist any hadrons containing top quarks. This property of the top quark provides an opportunity to study the properties of a bare quark.

The short life time also implies that the top quark decays before it can depolarize, hence the information on polarization of the top quark, is carried by its decay products.

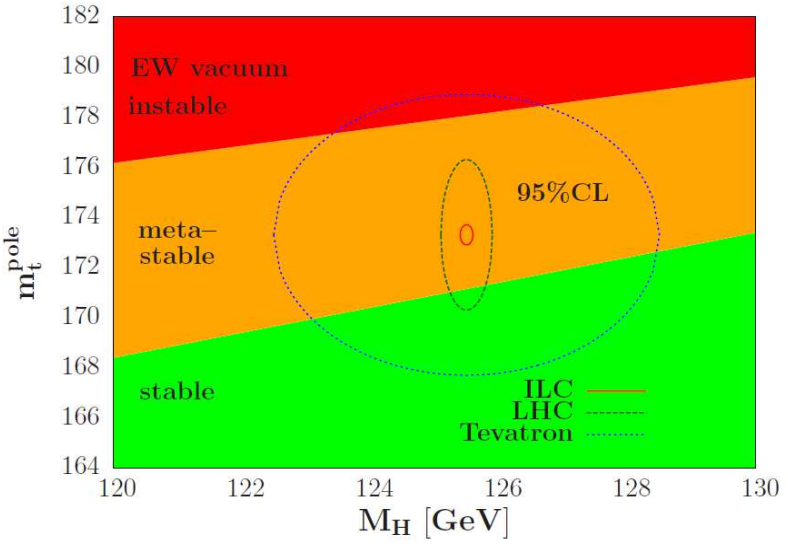


FIGURE 2.2: The stability of the electroweak vacuum, shown in the [$m_H$,$m_t$] plane. The $2\sigma$ ellipses show the precisions obtained at the LHC and Tevatron, and the one obtainable at the ILC, a future linear collider. The image is taken from [57].

| | |
|---|---|
| $t\bar{t} \rightarrow bq\bar{q}\bar{b}q\bar{q}$ | 46.2 % |
| $t\bar{t} \rightarrow bq\bar{q}\bar{b}l\nu_l$ | 43.5 % |
| $t\bar{t} \rightarrow bl\nu_l\bar{b}l\nu_l$ | 10.3 % |

TABLE 2.2: Fractions of different decay modes of $t\bar{t}$ pairs.

It decays through the electroweak interaction, predominantly (99.8 %) into a b quark and a W boson ($t \rightarrow bW^+$). From here on, only this decay vertex will be treated. The W boson can further decay into two quarks or a lepton and a neutrino. The following table presents the probabilities of the different decay modes for $t\bar{t}$.

The first of these is called fully the hadronic decay mode, while the remaining two are called semi-leptonic and fully leptonic, respectively.

The mass of the top quark is also one of the fundamental parameters of the electroweak theory. The precise measurement of top quark mass is important for the measurement of electroweak precisions. For example, the loop corrections to the Higgs boson mass are proportional to $(m_t/m_W)^4$[28].

The importance of the precise determination of the top quark mass can be highlighted in many ways. One of them is that it is strongly related to the stability of the electroweak vacuum, if the Standard Model is valid upto the Planck scale. The figure 2.2 shows the stability curve, in the plane of Higgs boson and top quark masses. Here the pole mass of the top quark is used, which is in fact the mass of the fermion propagator of the top quark. There exist another scheme to describe the mass of the top quark, called $\bar{M}S$ scheme. Along with the close relation of the top quark mass, to the stability of electroweak vacuum, the figure also shows the capability of the hadron colliders (LHC and Tevatron) and the future linear collider (ILC) to precisely determine the Higgs boson and top quark masses.

Due to large Yukawa couplings, the top quark mass is one of the factors constraining the mass of the Higgs boson, recently discovered at LHC. This fact is illustrated in the figure 2.3. A variation of 1 GeV in mass of the top quark, corresponds to a 10 GeV change in the mass of Higgs boson. The uncertainties on the mass of the top quark, thus strongly constrained the efforts to predict the mass of Higgs bosons from LEP experimental data. This constraint can also be interpreted in a different view, that it helps to verify the nature of the Higgs boson. For the Higgs boson to be compatible with the Standard Model, its mass should lie in the electroweak fit represented in 2.3. As there are other theories, which predict the existence of a light Higgs boson(s), at around the same mass, as the one discovered at the LHC. Any deviations from this fit, could hint at the existence

of new physics, beyond Standard Model. The discovered Higgs bosons's mass lies well within the bound, obtained by the fit using $W$ boson mass, and the mass of top quark.

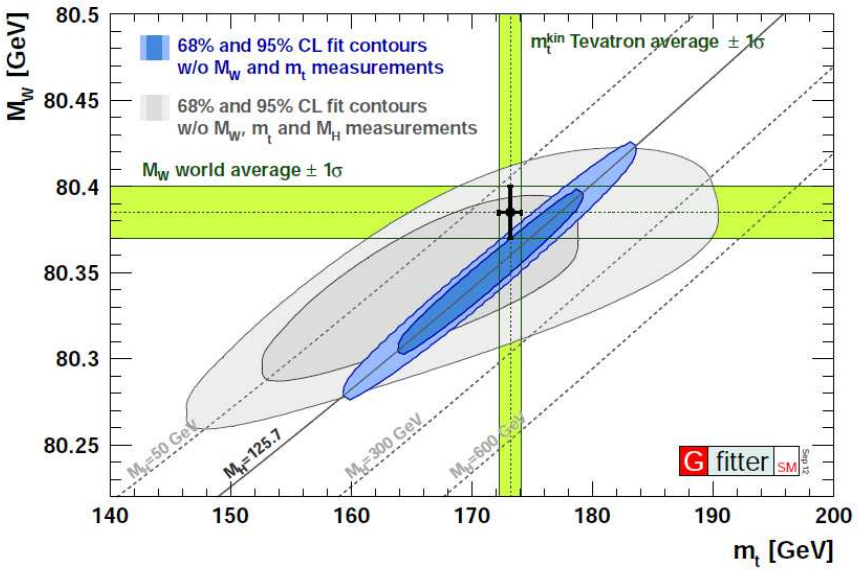


FIGURE 2.3: Indirect constraints on the mass of Higgs boson ($m_H$) with respect to top quark mass($m_t$) and W boson mass($m_W$). The indirect searches at LEP and Tevatron, excluded some regions for the mass of Higgs boson, which are not shown here. [37].

## 2.3 Electroweak couplings of top quark

Although the top quark was discovered 18 years ago, some of its properties still remain undetermined, including the electroweak couplings to gauge bosons. Current data does provide some weak constraints on the EW couplings, specially the LEP data which constraints the $t\bar{t}Z$ couplings indirectly. One of the reasons for this is that so far the top quark has only been studied at hadron colliders, where the production of the $t\bar{t}$ pairs is predominantly either through $q\bar{q}$ pairs ($q\bar{q} \rightarrow g^* \rightarrow t\bar{t}$), or gluon-gluon fusion($gg \rightarrow t\bar{t}$). As the process $q\bar{q} \rightarrow Z*/\gamma^* \rightarrow t\bar{t}$ is greatly suppressed, the couplings can only be indirectly measured in associate production of top pairs. However, the production of $t\bar{t}$ pairs at a lepton collider takes place through electroweak mechanism. The top quark pair production goes directly through the $t\bar{t}Z$ and $t\bar{t}\gamma$ vertices. Absence of concurrent QCD production leads to clean measurement of electroweak couplings of the top quark. The production mechanism is $e^-e^+ \rightarrow (Z/\gamma^*) \rightarrow t\bar{t}$, represented by the Feynman diagrams, in figure 2.4.

The general Lorentz-invariant equation, describing the interaction of a vector boson $X$ and two top quarks, can be written in terms of form factors. The generalized production

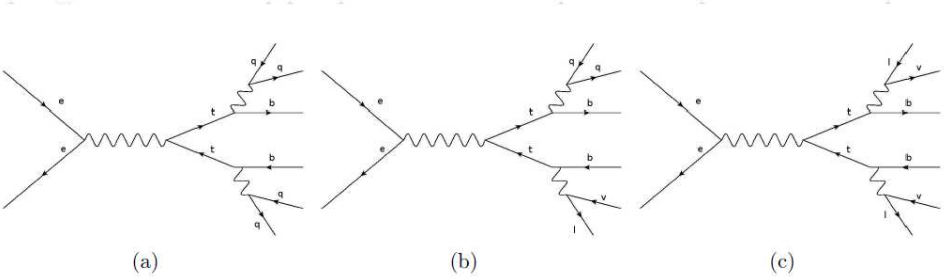


FIGURE 2.4: Feynman diagrams showing the production of $t\bar{t}$ pairs at an electron collider, and their decay. The three possible decay mechanisms a) fully hadronic, b) semi-leptonic and c) fully leptonic are shown.

vertex $ttX$ can be written as [29]:

$$\Gamma_{\mu}^{ttX}(k^2,q,\bar{q}) = ie\left\{\gamma_{\mu}\left(\tilde{F}_{1V}^{X}(k^2)+\gamma_5\tilde{F}_{1A}^{X}(k^2)\right)+\frac{(q-\bar{q})_{\mu}}{2m_t}\left(\tilde{F}_{2V}^{X}(k^2)+\gamma_5\tilde{F}_{2A}^{X}(k^2)\right)\right\} \tag{2.1}$$

Where $e$ is the electron charge, $m_t$ is the mass of top quark, $k^2=(q+\bar{q})^2$ is the four momentum of the gauge boson, $q$ and $\bar{q}$ represent the four vectors of the $t$ quarks. The $\gamma_{\mu}$ are Dirac matrices with $\mu=0,1,2,3$. The subscript $V$ and $A$ represent the vector and axial vector coupling form factors respectively. The term $\gamma_5=i\Pi\gamma_{\mu}$ allows to introduce the axial vector currents into theory.

Using the Gordon identity for the vector and axial vector currents in above equation, one can rewrite it as:

$$\Gamma_{\mu}^{t\bar{t}X}(k^2,q,\bar{q}) = -ie\{\gamma_{\mu}\left(F_{1V}^{X}(k^2)+\gamma_5F_{1A}^{X}(k^2)\right)+\frac{i\sigma_{\mu\nu}}{2m_t}(q+\bar{q})^{\nu}\left(iF_{2V}^{X}(k^2)+\gamma_5F_{2A}^{X}(k^2)\right)\} \tag{2.2}$$

Where $\sigma_{\mu\nu}=i/2(\gamma_{\mu}\gamma_{\nu}-\gamma_{\nu}\gamma_{\mu})$. It must be taken into account that the Gordon identity holds only when both top quarks are on-shell. It can easily be seen that form factors $\tilde{F}_i$ and $F_i$ in above equations, are related to each other as:

$$\tilde{F}_{1V}^{X}=-(F_{1V}^{X}+F_{2V}^{X}),\quad \tilde{F}_{1V}^{X}=F_{1V}^{X},\quad \tilde{F}_{1A}^{X}=-F_{1A}^{X},\quad \tilde{F}_{2A}^{X}=-iF_{2A}^{X} \tag{2.3}$$

In the Standard Model most of these form factors have a zero value and the vector and axial vector couplings of Z, go as $\frac{I_3-2Qs_w^2}{2s_wc_w}$ and $\frac{I_3}{2s_wc_w}$ respectively, where $I_3$ is the third component of the Isospin, taking the following values.

$$I_3(e_L,t_L,e_R,t_R)=(\frac{-1}{2},\frac{1}{2},0,\frac{-1}{2}) \tag{2.4}$$

At the tree level, the non-zero form factors have the following values:

$$F_{1V}^{\gamma} = -\frac{2}{3}, \quad F_{1V}^{Z} = -\frac{1}{4s_w c_w}\left(1 - \frac{8}{3}s_w^2\right), \quad F_{1A}^{Z} = \frac{1}{4s_w c_w} \tag{2.5}$$

Where $c_w$ and $s_w$ represent $\cos\theta_w$ and $\sin\theta_w$ respectively, where $\theta_w$ is the Weinberg Angle.

The above expression for the Born level, six form factors $F_{1A}, F_{1V}, F_{2V}$for $Z$ and $\gamma$ are CP conserving form factors, while the two form factors $F_{2A}$ are the CP violating form factors.

$F_{2V}^{\gamma,Z}$ are the electric and weak magnetic dipole moment form factors, while the $F_{2A}^{\gamma,Z}$ are the electric and weak electric dipole moment form factors.

The sign of the form factor values are sensitive to the interference between the $Z$ and $\gamma$. This limits the precise determination of the electroweak couplings of top quark, at the hadron colliders, where the couplings are to be measured in the associated vector boson production. As is the case at the LHC for example, only the absolute value of the couplings can be determined.

By using the above form factors, and taking into account the helicity of the incoming electrons, one can write new form factors as follows [39]:

$$\mathcal{F}_{ij}^{L} = -F_{ij}^{\gamma} + \left(\frac{\frac{-1}{2} + s_w^2}{s_w c_w}\right)\left(\frac{s}{s - m_Z^2}\right)F_{ij}^{Z} \tag{2.6}$$

$$\mathcal{F}_{ij}^{R} = -F_{ij}^{\gamma} + \left(\frac{s_w^2}{s_w c_w}\right)\left(\frac{s}{s - m_Z^2}\right)F_{ij}^{Z} \tag{2.7}$$

Where $L$ and $R$ represent the helicity of the incoming electrons, $i = 1, 2$ and $j = V, A$ refer to the structure of the form factors. $s$ is the square of the of the center-of-mass energy $\sqrt{s}$.

By using the similar notations, the decay vertex of the top quark $t \to bW$ can be written as follows:

$$\Gamma_{\mu}^{tWb}(k^2, q, \bar{q}) = i\frac{g}{\sqrt{2}}\left\{\gamma_{\mu}\left(F_{1L}^{W}(k^2)P_L + F_{1R}^{W}(k^2)P_R\right) + \frac{i\sigma_{\mu\nu}}{2m_t}(q + \bar{q})^{\nu}\left(iF_{2L}^{W}(k^2)P_R + F_{2R}^{W}(k^2)P_L\right)\right\} \tag{2.8}$$

The strong coupling of the top quark to the electroweak symmetry breaking suggest that top quark studies can be a gateway to new physics. A specific scenario for this case are Randall-Sundrum Models [49]. These models and composite Higgs models have been discussed in detail in Volume 1, section 5.3.1 of [40]. Following the Randall-Sundrum

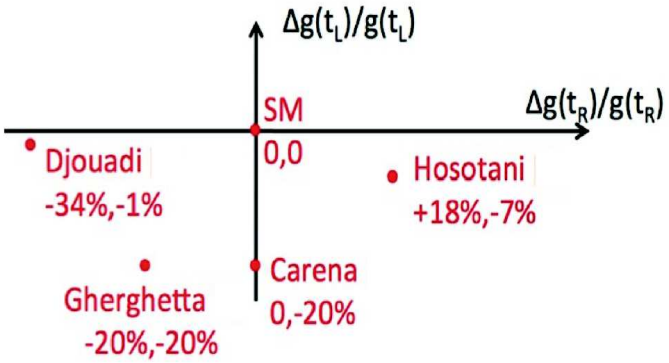


FIGURE 2.5: Divergence of $t\bar{t}Z$ couplings from Standard Model prediction, as predicted by some models, in Randall-Sundrum scenario.

approach, the couplings of the top quark to the Z boson may diverge from the predictions of the Standard Model, due to Z-Z' mixing. Various proposals have been made for these divergences, for example Djouadi [45], Hosotani [46], Ghergheta [47] and Carena [48], as shown in figure 2.5.

## 2.4 Cross sections

The production cross section could be written in terms of the above mentioned form factors. The Born level cross section with electron beam polarization $I = L, R$, can be expressed as:

$$\sigma_I = 2\mathcal{A}N_c\beta\left[(1+0.5\gamma^{-2})(\mathcal{F}_{1V}^I)^2 + (\mathcal{F}_{1A}^{I'})^2 + 3\mathcal{F}_{1V}^I\mathcal{F}_{2V}^I\right] \tag{2.9}$$

Where $\mathcal{A} = \frac{4\pi\alpha^2}{3s}$, $\alpha(s)$ is the electromagnetic running coupling constant, $N_c$ represents the number of quark colors, $\gamma$ is the Lorentz factor, $\beta$ is the velocity and $\mathcal{F}_{1A}^{I'} = \beta\mathcal{F}_{1A}^I$.

Figure 2.6 shows a prediction for the $t\bar{t}$ production cross section at the ILC. Different curves represent the center-of-mass energy loss mechanisms at the ILC, at the interaction point.

Further details on the polarized cross sections and beam polarizations will be given in 5.4.

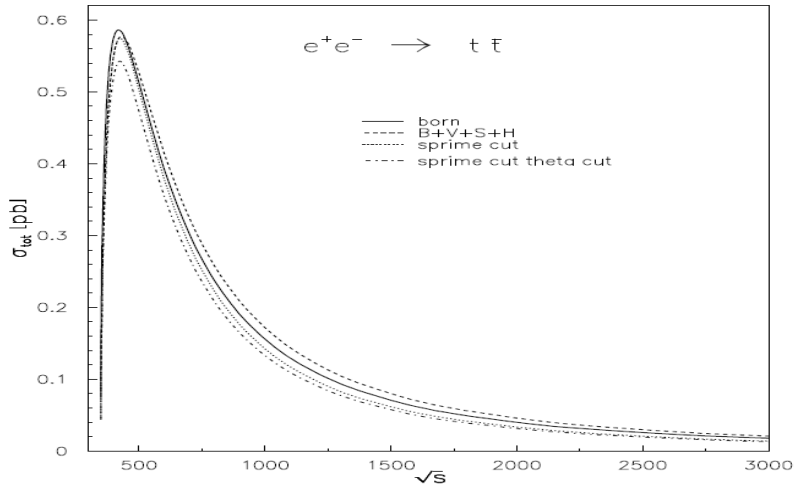


FIGURE 2.6: $t\bar{t}$ production cross section, as a function of center-of-mess energy. The solid curve is for Born level cross section, while the dashed lines show the electroweak cross section. The dotted and dashed-dotted curves take into effect the loss of beam energy mechanisms such as ISR. The figure is taken from [52].

## 2.5 Forward Backward Asymmetry

The above mentioned form factors can also be used to write the Forward-Backward Asymmetry of top quark pair production, as shown in the following equation:

$$(A_{FB}^t)_I = \frac{-3\mathcal{F}_{1A}^{I'}(\mathcal{F}_{1V}^I + \mathcal{F}_{2V}^I)}{2[(1+0.5\gamma^{-2})(\mathcal{F}_{1V}^I)^2 + (\mathcal{F}_{1A}^{I'})^2 + 3\mathcal{F}_{1V}^I\mathcal{F}_{2V}^I]} \tag{2.10}$$

Figure 2.7 shows the $A_{FB}^t$, as a function of $\sqrt{s}$, for unpolarized electron-positron beams.

However, the $A_{FB}^t$ is sensitive to beam polarizations. Using Standard Model values for the form factors, the following values for $A_{fb}^t$ can be deduced, for the respective electron beam polarizations.

$$(A_{FB}^t)_L = 0.38, (A_{FB}^t)_R = 0.47. \tag{2.11}$$

The asymmetric distribution of the fermion in the forward and backward hemispheres of the detectors, is called the Forward-Backward Asymmetry, and it is a characteristic, common to all fermions. The first observations of the parity violation, in the Madame Wu experiment, showed the inhomogeneous distribution of the final state fermions. Since then, it has been observed and measured at various experiments, involving different fermion, notably $b$ quarks and $t$ quarks. The definition of $A_{FB}^t$, in experimental terms,

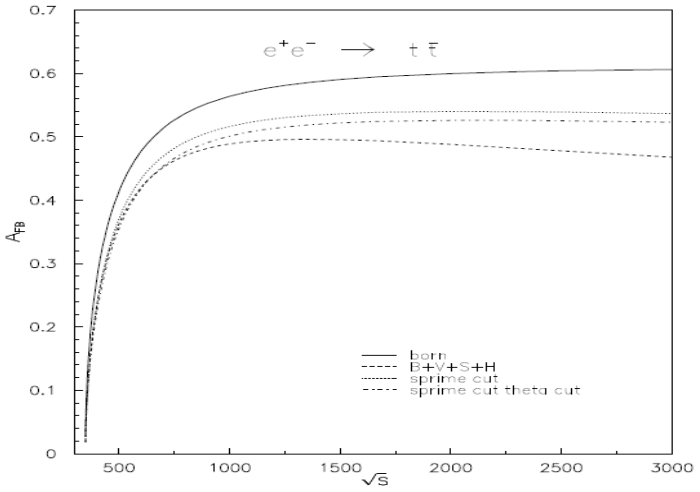


FIGURE 2.7: $A^t_{FB}$ as a function of $\sqrt{s}$. The Born level $A^t_{FB}$ is shown by solid lines. [52].

can be put as follows:

$$A^t_{FB} = \frac{N(0 < \theta_{top} \leq \frac{\pi}{2}) - N(\frac{\pi}{2} < \theta_{top} \leq \pi)}{N(0 < \theta_{top} \leq \frac{\pi}{2}) + N(\frac{\pi}{2} < \theta_{top} \leq \pi)} \tag{2.12}$$

The $A_{FB}$ for the $b$ quarks was measured at LEP [43, 44], and was found to be slightly above the Standard Model expectations. A deviation of $3\sigma$ was observed. Also, a measurement of $t\bar{t}$ forward backward asymmetry $A^t_{FB}$ has been made at the Tevatron[22, 23]. The Standard Model predicts this value to be 0.078[21] but a value of $0.19 \pm 0.0065$ $(stat.) \pm 0.024$ $(syst.)$ is observed[22], which is $2\sigma$ off. However, the value of $A^t_{FB}$ is dependent on the production mechanism of the top quark pairs. These measurements correspond to the QCD production of the $t\bar{t}$ pairs, as Tevatron is a $p\bar{p}$ collider and the $t\bar{t}$ production is dominated by $q\bar{q} \rightarrow t\bar{t}$ . Although LHC is also a hadron collider, but higher center-of-mass energy and $pp$ collisions instead of $p\bar{p}$ imply that the production is dominated by gluon-gluon fusion.

These anomalies have significant implications. The $b\bar{b}$ asymmetry can, for example, be explained by the contributions of Kaluza-Klein excitations of electroweak gauge bosons in warped extra-dimension models. In these models, the gauge interactions of $b$ and $t$ quarks are different from that of light quarks, due to their different behavior in the extra dimensions. But it is more difficult to generate a $t\bar{t}$ forward backward asymmetry through exchanges of Kaluza-Klein gluons because of electroweak precision constraints[45].

All measuements of the $t\bar{t}$ asymmetry were made at hadron collider, so far. A detailed review on the measurement of $A^t_{FB}$ at hadron colliders will be given in Chapter 5. This thesis will concentrate on the study of $A^t_{FB}$, at the ILC, using fully hadronic decays of

$t\bar{t}$ at a 500 GeV center-of-mass energy. The studies are carried out for $t\bar{t}$ decaying to six quarks; $e^-e^+ \to t\bar{t} \to (bW^+)(\bar{b}W^-) \to b\bar{b}q\bar{q}q\bar{q}$.

A linear collider is an ideal machine to study particle physics at a high precision level. Today, the most advanced proposal for a linear collider is the International Linear Collider. Apart from measuring the electroweak couplings of the top quark, studies have been made for the capability of the ILC, to measure the top Yukawa couplings in associated Higgs production, at various center-of-mass energies[53, 54, 55]. The precision level achievable at the ILC, makes it possible to not only study the top quark in details, but also the other physics processes including precision Higgs measurement and W physics. The potential of the ILC to find any hint of the new physics has been shown in the studies with full detector simulations. The details description of ILC and its detector will be given in the next chapter.

# Chapter 3

# International Large Detector (ILD)

## 3.1 Introduction

The physics results achieved at the LHC need to be complemented by high precision measurements, which are achievable with lepton colliders. At lepton colliders, the full beam energy is available in the collision while at hadron colliders it is shared among the constituent quarks of hadrons. Moreover, the undesired QCD background at hadron collisions, can be avoided at lepton colliders.

The best option for a lepton collider, at high energies, is a linear accelerator. Charged particles moving in a circular path, radiate energy which is proportional to $\frac{E^4}{m^4}\frac{1}{r^2}$[58]. This radiation is called synchrotron radiation. Electrons, being lighter than protons, radiate far more energy in a circular accelerator. Upto a certain limit of beam energy, circular colliders can be used for electron beams, for example LEP, but for high beam energies, synchrotron radiation is a very challenging problem to control.

At the moment, there are two main proposals for a linear collider: The International Linear Collider (ILC) and the Compact Linear Collider(CLIC) [59].

The ILC [40] is designed to operate at a center-of-mass energy of $\sqrt{s} = 500$ GeV, later on extendable to 1 TeV, while CLIC is designed to start operating at 500 GeV and can be upgraded upto 3 TeV.

## 3.2 The International Linear Collider

One of the advantages of a linear collider is that it can run at any center-of-mass energy, accessible within its design. The luminosity is approximately proportional to the energy.

| **ILC design parameters** | |
|---|---|
| center-of-mass energy $\sqrt{s}$ | 91-500 GeV |
| Peak Luminosity | $2 \times 10^{34}$ cm$^{-2}$s$^{-1}$ |
| electron beam polarization $P_{e^-}$ | >80% |
| positron beam polarization $P_{e^+}$ | upto 30% |
| Total Length | ~31 km |

TABLE 3.1: Major ILC design parameters. The design allows for an upgrade up to a center-of-mass energy of 1 TeV.

The ILC will collide electrons and positrons, at a center-of-mass energy upto 500 GeV. The accelerator required for this purpose is approximately 31 km in length. It is designed to generate a total of 500 fb$^{-1}$ of data in the first four years of operation. The important design parameters for the ILC[40] are summarized in the following table.

The technology of the ILC is based on 1.3 GHz superconducting RF cavities, which will operate at a gradient of 31.5 MV/m. Polarized electrons are produced by a laser illuminating a photo cathode in a DC gun. A normal conducting structure pre-accelerates these beams to 76 MeV. After-wards, they are accelerated to 5 GeV in superconducting linacs. Superconducting solenoids rotate the spin vectors into the vertical direction, before injecting the beam into damping rings. These damping rings are 6.7 km in circumference as shown in figure 3.1. The beams are then injected into the main linacs which are ~11 km long . Finally, they are focused to very small spot sizes, of the order of a few nanometers, at the collision point, using a beam delivery system which is 2.2 km per side.

The baseline time structure of the beam consists of bunchtrains of 1312 bunches spaced 554 nanoseconds, passing the interaction point at a rate of 5Hz. Each bunch train is about 0.3 millimeter long, with about 200 milliseconds between bunch trains. These parameters are for ILC operating at $\sqrt{s} = 500\,GeV$.

Beam polarization is one of the assets of the ILC. It enables the study of physics parameters involving the spin of particles, for example helicity. The $e^-$ beams can be polarized upto 80% while the $e^+$ beams can be polarized upto 30% without using photon collimators and upto 60% with photon collimators [65]. Longitudinally polarized positron beams are generated from the circularly polarized photons, which are produced by the helical undulator in the ILC accelerator system. This undulator is installed at the end of the main linac beamline. The photons generated by undulator strike the rim of a rotating titanium target, which has a thickness of 0.4 radiation lengths. The electron positron pairs are generated at this point, and positrons are captured by 0.07 mrad transverse dynamic aperture. The polarization of the positron beams is conserved throughout the transportation of the positrons to damping rings.

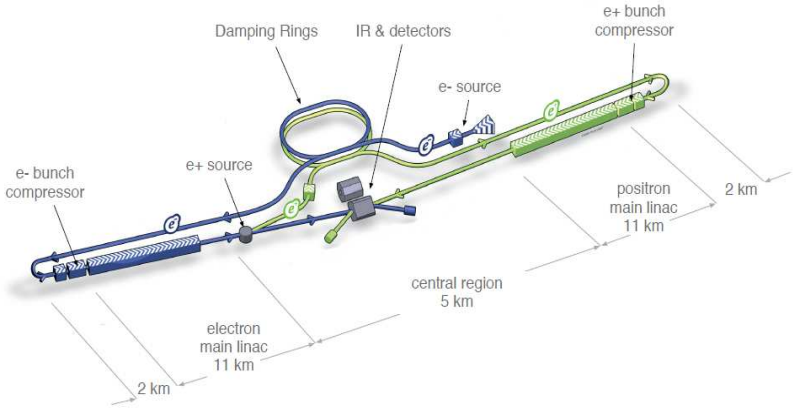


FIGURE 3.1: Accelerator system of the ILC. Damping rings, main linacs and beam delivery system are shown. Blue color represents electron beam system, while green color is for positron beam.[40]

| Particle type | Energy fraction | Detector |
|---|---|---|
| Charged particles | ~60% | Tracker |
| Photons | ~30% | ECAL |
| Neutral hadrons | ~10% | ECAL + HCAL |

TABLE 3.2: Constituents of a typical jet, along with fracation of the jet energy carried by them.

The ILC is proposed to have two detectors, to complement each other for the physics measurements, namely the Silicon Detector (SiD)[60] and the International Large Detector (ILD)[61]. The SiD is a compact detector, based on silicon technology which will operate in a magnetic field of 5T. The design of the ILD results in a large sized detector with a large TPC used for tracking and highly granular calorimeters. It will operate in a lower magnetic field of 3.5 T.

## 3.3 The Particle Flow Algorithm (PFA)

Precision measurements require a good performance from detectors and reconstruction algorithms. The Particle Flow [66] approach will be followed at the ILC to reconstruct final state particles. It will be used to reconstruct quark and gluon jets from their constituent particles. Typically, a jet is composed of different types of particles. The contribution of photons, charged and neutral hadrons to the total jet energy is given in the table below.

The PFA uses the reconstructed energy from these particles, in each sub-detector as shown in the table above, to reconstruct the jet energy. The technique not only requires

an excellent particle identification and granularity from the calorimeter, but also the complementarity of different subdetectors operating together.

While the PFA has been tested at existing experiments for example CMS[70, 71], it determines the design of the detectors at the ILC, that will be optimized for its use. Within the framework of detector R&D for the ILC, the PFA has been already applied to beam test data taken over prototype sub-detectors[69].

## 3.4 The ILD detector concept

The ILD is a multipurpose $4\pi$ detector. Its two main features are: The Particle Flow approach to identify individual particles [68], and a good tracking and vertexing performance. The PF approach requires highly granular calorimeters. An excellent performance from the vertex detectors and trackers is necessary to reconstruct the tracks of charged particles, and to determine their charge. The R&D for the ILD is driven by these factors. A schematic view of the ILD is shown in figure 3.2. It consists of many subdetectors, optimized for different tasks. Along with individual performance, the detectors are required to be complementary to each other. Their detailed description is given in the next sections.

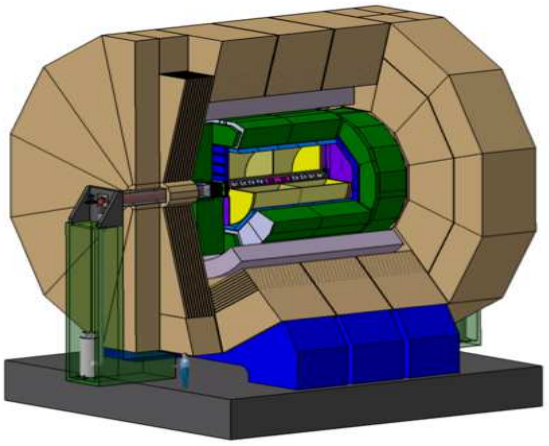

FIGURE 3.2: A Schematic view of the International Large Detector (ILD). The relative dimensional size is exhibited with respect to average height of a human. Different subdetectors of the ILD are shown in different colors.

### 3.4.1 Vertex Detectors (VTX)

The principal goal of a vertex detector is to identify the interaction vertex and vertices of short-lived particles such as D or B mesons and $\tau^{\pm}$. Since it is closest to the interaction

point, it reconstructs the first point of a track. The vertices of short lived particles are traced back by using the track information of their decay products.

It also plays a vital role in reconstructing the jet charge and in flavor tagging. In the analysis described in this thesis, these two parameters have a central importance. The recognition of b-jets and reconstruction of their charge have been used to identify top and anti-top quarks. The analysis will be discussed in detail in chapter 5.

Taking into account these requirements, the following conditions are to be fulfilled at the VTX of the ILD.

- A single point resolution of less than 3 $\mu$m is required.
- The thickness of the material between the first measured point of a track and the IP should be less than 1% of the radiation length $X_0$.
- The first layer of the vertex detector should be $\sim$ 15 mm from the IP.

The impact parameter resolution of the vertex detector, $\sigma_{ip}$, can be expressed as follows:

$$\sigma_{ip} = a \oplus \frac{b}{p \cdot \sin^{2/3}\theta} \mu m \tag{3.1}$$

Here, $p$ is the track momentum, and $\theta$ is the angle of the track with respect to the beam axis. For the VTX at the ILD, the required resolution can be achieved with $a \leq 5$ $\mu$m & $b \leq 10$ $\mu$m. In comparison to previously used vertex detectors, these numbers are almost half of the next achieved number in terms of vertex detector resolution. For example, for the SLC detector, $a \simeq 10$ $\mu m$ and $b = 33$ $\mu m$[75].

The baseline design of the VTX, which should meet these requirements, is in the R&D phase. The VTX consists of 3 concentric layers of double-sided ladders which are $\sim$2 mm apart. Each ladder has a thickness of $\leq 50$ $\mu$m, divided in pixels. The inner-most layer is at 16mm from the IP and the outermost layer is at 60mm. The material of each ladder accounts for 0.15% $X_0$ in total. The VTX provides an overall point resolution of 2.8 $\mu$m. Some parameters of the VTX are listed below. This geometry is called double ladder (VTX-DL).

The alternative geometry for this baseline design is called single ladder (VTX-SL). It consists of 5 equally-spaced single layers. The radius of the first layer, is the same as the previous one, while the last layer has a radius of 60mm. The two geometries are shown in figure 3.3

| Layer No. | Inner Radius (mm) | Length $z$ (mm) | $\cos\theta$ | $\sigma$ ($\mu$m) |
|---|---|---|---|---|
| 1 | 16 | 62.5 | 0.97 | 2.8 |
| 2 | 18 | 62.5 | 0.96 | 6 |
| 3 | 37 | 125 | 0.96 | 4 |
| 4 | 39 | 125 | 0.95 | 4 |
| 5 | 58 | 125 | 0.91 | 4 |
| 6 | 60 | 125 | 0.90 | 4 |

TABLE 3.3: Dimensions of the different layers of vertex detector and the polar angle covered by them. The respective point resolution is also shown.

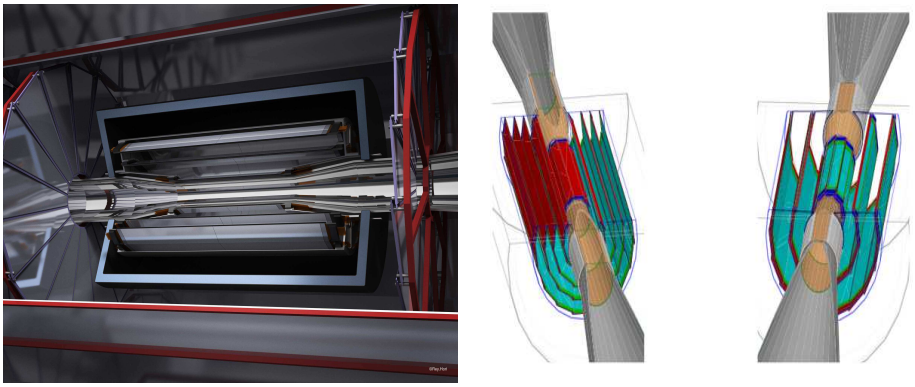

FIGURE 3.3: The vertex detector of the ILD. The left figure shows a view of the VTX around the beam pipe, at the interaction point. The right part shows two proposed geometries; Single Ladder and Double Ladder.

There are currently three readout technologies under consideration for VTX. The CMOS Pixel Sensor(CPS)[72], Fine Pixel CCD (FPCCD) [73] and Depleted Field Effect Transistor(DEPFET) [74] are the potential options.

The performance of the vertex detector with CMOS pixel sensor technology, is shown in figure 3.4. The single point resolution is plotted versus the signal to noise ratio [64]. Various colors represent different in-pixel circuits. The resolution is close to the required $\sim$3 $\mu$m. The chips of the VTX contain 1152 columns, each of 576 pixels. Each pixel has a 18.4 $\mu$m pitch. The VTX has also been tested for MIP detection efficiency. The efficiency is better than 99%.

### 3.4.2 Central Tracking

Track reconstruction for charged particles at the ILD consists of two parts, namely silicon tracking and central tracking. The silicon trackers are the Silicon Internal Tracker (SIT), the Silicon External Tracker (SET), the Endcap Tracking Detector (ETD) and the

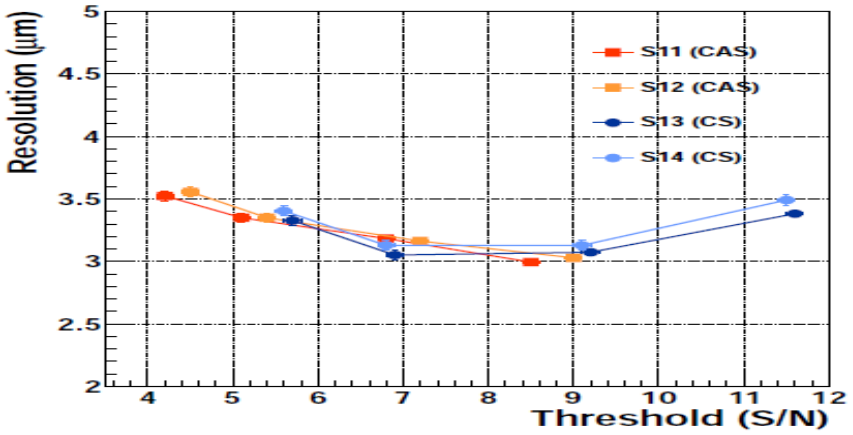


FIGURE 3.4: Single point resolution of the VTX with CMOS Pixel Sensor technology, as a function of the S/N ratio for different in-pixel circuits (S11-S14).

Forward Tracking Detector(FTD). The central tracking uses a Time Projection Chamber (TPC).

#### 3.4.2.1 Silicon Tracking

The SIT is placed between the TPC and the VTX. Its role is to provide the link between the TPC and the vertex detector. It consists of 2 silicon layers. The SET is located in the barrel part, between the TPC and the electromagnetic calorimeter (ECAL). It is the third silicon layer in the central barrel region and it provides outermost point of the track. The ETD is placed between the TPC end plate and endcap calorimeter system. It serves as an entry point to the ECAL. The SIT and SET also provide time-stamping of bunches, allowing for bunch tagging of each event. Time stamping of the bunches is particularly important to avoid the overlap of events.

SIT, SET and ETD consist of microstrip silicon sensors. The baseline sensors are $10 \times 10 cm^2$, with a $50 \mu m$ pitch. The sensors have a very thin edge, (inactive zone), ranging between a few 10s of $\mu m$ to a few 100 $\mu m$. These detectors are shown in figure 3.5. In the left part of the figure, the relative position of the silicon trackers can be seen with respect to the TPC and the ECAL, while the right part is a detailed 3D implementation in Geant4 of the TPC geometry, in a right-handed coordinate system with the origin at the interaction point(0,0,0).

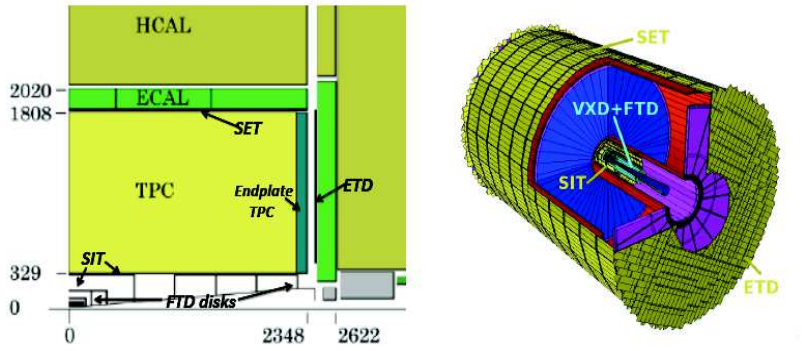


FIGURE 3.5: ILD tracking detectors. The left figure shows a quadrant of the tracking system where ETD, FTD, SIT and SET are visible, with their relative positions to the Vertex Detector (VXD), TPC and ECAL. The right side represents a Geant 4 Implementation of the silicon system.

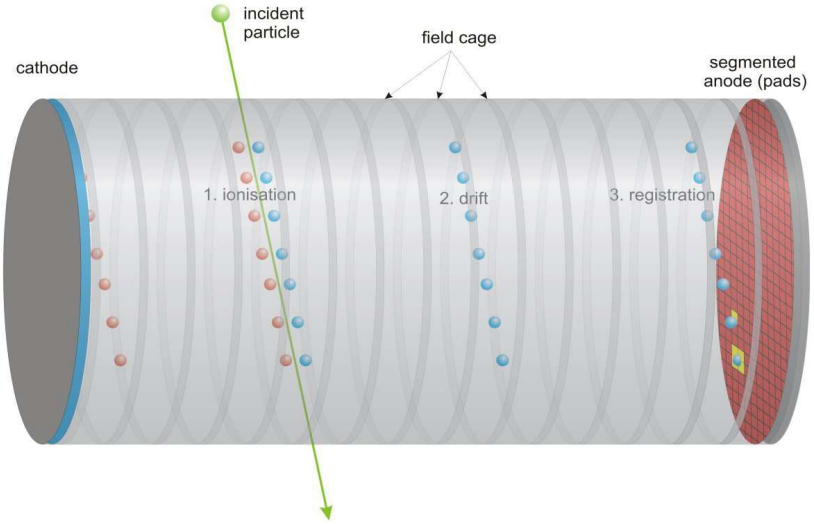


FIGURE 3.6: The working principle of a time projection chamber.

### 3.4.2.2 The Time Projection Chamber (TPC)

The Time Projection Chamber (TPC) is used to measure the trajectories of particles coming out of the vertex detector. The TPC is filled with a gas. When a charged particle enters the TPC, it ionizes the molecules of the gas. Due to the applied voltage, the released electrons drift towards the anode. At the anode, these electrons are detected on the readout plates, which are segmented perpendicular to the drift direction. In order to measure precisely the position of particle, the electric field needs to be homogeneous throughout the volume of the TPC. The working principle of a TPC is exhibited in figure 3.6.

The TPC of the ILD consists of two identical chambers filled with gas. The cathode is placed at the center of the TPC, while anodes occupy the ends of volume. These anodes are equipped with a readout system. A high voltage is applied, which creates an electric field across the TPC.

The TPC is expected to work in a magnetic field of 3.5 T. The main requirements on the design of the TPC are characterized by two parameters, the point resolution $\sigma_p$ and double hit separation. The objective is to achieve a point resolution less then 100 $\mu m$ and a double hit separation resolution of 2 mm.

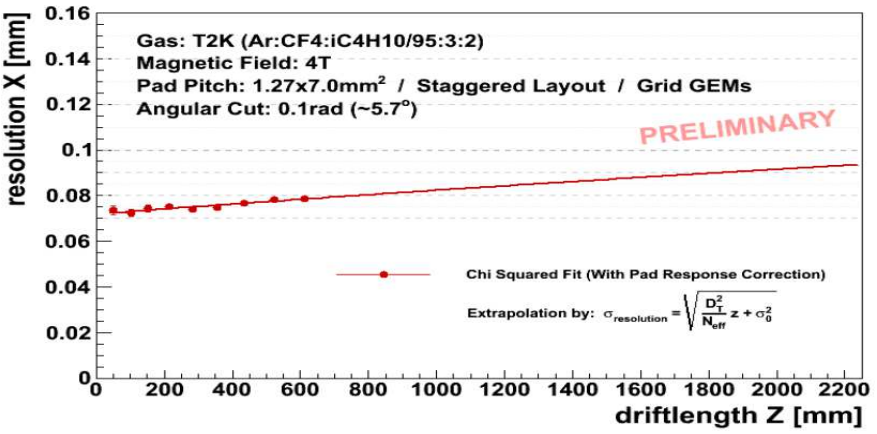


FIGURE 3.7: The single point resolution of the TPC prototype, with GEM readout, measured in a 4T magnetic field. The curve is extrapolated to full drift lengths.

The TPC will have an inner radius of 330 mm and an outer radius of 1808 mm. It will be 4.7 meters in length along the z-axis. It will cover an angle of $|\cos\theta| \simeq 0.98$.

The choice of the TPC gas is driven by the requirements on drift velocity and its diffusion properties. A drift length of 2 m and a magnetic field of 3.5 T are also taken into account. The gas considered for the TPC is called T2K gas, which is a Ar-CF4(3%)-isobutane(2%) mixture.

A prototype has been developed and has been tested at experimental facilities. Figure 3.7 shows the performance of this prototype operating in a 4T magnetic field. The single points resolution is shown against the drift length. The extrapolation of the curve to full drift lengths shows that a point resolution $\sigma_p \leq 100$ $\mu$m can be achieved [83].

### 3.4.3 The ILD Calorimeter System

In the PFA, as described earlier, the emphasis is placed on the full tracking of the shower particles in the calorimeter, rather than the energy resolution of individual particles. The

calorimeters should enable a full tracking of the shower particles in the calorimeter. The required high granularity implies a large number of cells and readout channels. The calorimeter system of the ILD is expected to have $\sim 10^8$ channels, with the current baseline design. The R&D for the calorimeter system is mainly done by the CALICE collaboration [76]. The calorimeters are described below, in more detail.

#### 3.4.3.1 The Silicon Tungsten Electromagnetic Calorimeter (Si-W ECAL)

The main role of the ECAL is to reconstruct photons and electrons. It must be able to measure their energy, position, and angle. To meet the performance goal, with the PFA, the ECAL needs to have a high granularity and to be placed inside the magnetic field. The latter requirement implies that it should be as thin as possible, for a compact and cost effective detector. In addition, it should also have a minimum insensitive area.

The ILD ECAL will have a barrel and endcap structure, divided into 8 staves in the barrel region. A schematic view of the ECAL and of one module are shown in fig 3.8.

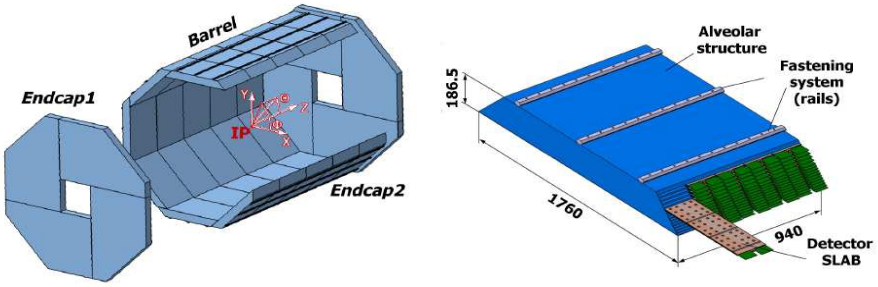


FIGURE 3.8: Si-W ECAL of the ILD. The left part of the figure is a depiction of Barrel Endcap structure of ECAL, while the right part shows one module, with alternate layers.

A Silicon Tungsten Calorimeter is one of the options for ILD. Silicon is chosen as active material, while Tungsten is the absorber material. The choice of absorber material is driven by the compactness of the detector and the need to separate particle which are close together. This implies that the absorber material should have a small radiation length $X_0$, a small Moliére radius and a high ratio of interaction length $\lambda_I$ to radiation length $X_0$. Tungsten meets these requirements, as outlined below.

- A small Moliére Radius $R_M$ of 9 mm helps to separate particle showers.
- A small radiation length $X_0 = 3.6$ mm helps to make a compact detector.
- A high $\lambda_I/X_0 = 27.5$ ratio helps to achieve the longitudinal separation electromagnetic and hadronic showers, by making sure that hadrons only start interacting in the later part of the ECAL.

| | |
|---|---|
| Number of Si Layers | 30 |
| Cell size | $5 \times 5$ mm$^2$ |
| Total Thickness | 185 mm |
| Inner Radius | 1843 mm |
| Outer Radius | 2028 mm |
| Radiation lengths | 24 $X_0$ |
| Total Surface Area of Silicon | 2500 m$^2$ |

TABLE 3.4: Major properties of the Si-W ECAL of the ILD.

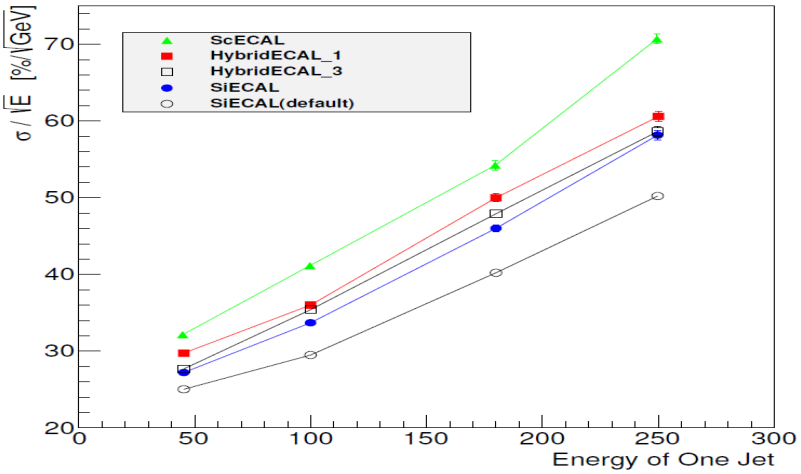


FIGURE 3.9: The performance of Electromagnetic Calorimeter for the ILD. The figure shows the energy resolution of various proposals for ECAL.

The important properties of the Si-W ECAL are summarized in the following table.

The choice of these parameters ensures 99% containment of 5GeV electromagnetic showers, while more than 98% of 50 GeV showers is contained in the ECAL.

According to the baseline design, the Si-W ECAL will comprise of 30 readout layers. Each silicon layer will be $\sim 300$ $\mu$m thick, and will consist of 4 wafers, per stave. Wafers of size $9\times9$ cm$^2$ will be segmented into $16\times16$ cells, each cell measuring $5 \times 5$ mm$^2$. This cell size has been decided after dedicated R & D studies to optimize the cell size.

The first Si-W ECAL prototype which was developed to test the proof of principle, was called the physics prototype. It was a 30 layer module with varying absorber thickness. Various tests at DESY, FNAL, and CERN were done with different incident particles and with different energy ranges. Analysis of this data determined an electromagnetic energy resolution of $\sigma_E/E$ =(16.6 $\pm$ 0.1) % $/\sqrt{E(GeV)}\oplus$ (1.1 $\pm$ 0.1) % with a MIP signal over noise ratio of S/N $\approx$ 7.5[77] [78]. This value is in good agreement with the ILD simulations.

One of the important objectives of the R&D is to optimize the cost to performance ratio of the ECAL. Along with considering alternative options (described in the next section), the efforts have also concentrated on minimizing the cost of the Si-W ECAL, by optimizing the number of layers (to make a cost effective ECAL without effecting the performance) and the size of the guard rings. The guard rings prevent the current leakage but are also dead zones which should be minimized. This optimization will be discussed in more detail in Chapter 4.

#### 3.4.3.2 Alternatives for ECAL

Besides the Si-W ECAL design, alternative technologies are proposed that could be more cost effective. One of them is the Scintillator ECAL(ScECAL). The idea is to use 5 × 45 $mm^2$ scintillator strips, arranged in alternating directions, to achieve an effective granularity, of 5 × 5 $mm^2$. One of the difficulties with developing the ScECAL, is the thickness of the scintillator strips. The silicon strips of a few hundred microns can be easily developed while scintillator strip needs to be at least 1mm thick. In order to conserve the total thickness of the ECAL, other components have to be made thinner.

Another proposal is a hybrid ECAL, which is a combination of the Si-W ECAL and ScECAL. Various configurations involving silicon and scintillator layers have been studied with the help of detailed simulations.

The performance of different options for the ECAL is shown in Figure 3.9. The energy resolution $\sigma_E/\sqrt{E}$ is plotted versus the jet energy. The default option, Si-W ECAL(SIECAL in the figure), has the best resolution.

#### 3.4.3.3 The Hadronic Calorimeter (HCAL)

The purpose of hadronic calorimeter is to separate the energy deposited by charged and neutral hadrons, and to precisely measure the energy deposited by the latter.

The HCAL of the ILD will be a barrel and endcap sampling calorimeter as shown in fig 3.10. Currently there are two options under study, namely analogue (AHCAL) and semi-digital (SDHCAL). It will consist of alternative layers of steel as absorber material, and scintillator tiles (AHCAL) or glass RPC (SDHCAL) as active material. Stainless steel has been chosen as absorber material. It has an interaction length of $\lambda_I$ = 17 cm and a radiation length of $X_0$ = 1.8 cm. The moderate ratio $\lambda_I/X_0$ allows for a fine sampling in the longitudinal direction. Steel is cheap and its rigidity helps to realize a self supporting structure, minimizing the dead areas due to auxiliary support structures. The HCAL has a total depth of $\sim 6\lambda_I$.

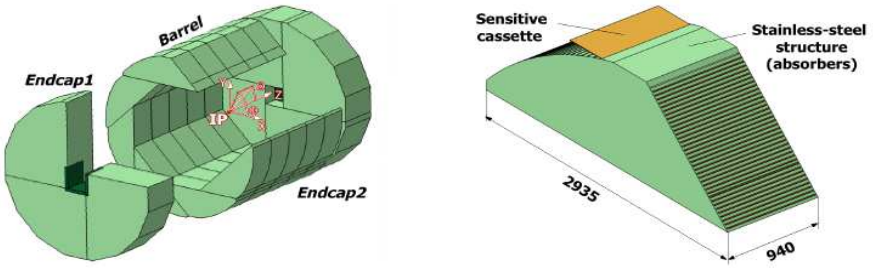


FIGURE 3.10: View of the HCAL. The barrel endcap structure is depicted in the left part, while the right part shows a module of the detector.

There are two options for the geometry of the HCAL. The first one has 2 rings in longitudinal direction and 16 modules in azimuthal direction, while the second one has 5 rings along the z-direction and 8 modules.

The optimization of the HCAL is driven by two parameters, the total depth and the cell size. The total depth contributes to the energy resolution by controlling the shower leakages beyond the HCAL. The cell size is important for the separation of particles. It also affects the cost of the detector, by increasing the number of readout channels. These parameters have been optimized with dedicated studies, using full detector simulations. This optimization has also taken into account the possibility of the ILC extension upto 1 TeV, where highly energetic jets are expected. These studies have shown the capability of a 48 layer ($6\lambda_1$) HCAL to absorb hadronic showers at these high energies. These studies have also shown that, for the AHCAL, a cell size of $3\times3$ cm$^2$ is the best compromise between a good energy resolution and a large number of channels. A smaller size will increase the number of readout channels, without providing any substantial gain on particle separation. A larger cell size will degrade the particle separation power of the HCAL. Similar studies for the SDHCAL resulted in a cell size of $1 \times 1$ $cm^2$ as the best option.

The energy resolution performance of the AHCAL physics prototype is shown in the left part of Figure 3.11. The resolution shown here is for charged pions. The figure represents three types of curves, the ones obtained with simple energy sums and those with local and global software compensation techniques. These techniques help to improve the resolution by 20%, and the stochastic term is reduced to $(45\pm0.3)\%/\sqrt{E_{beam}(GeV)}$ [84]. The right part of the figure shows the energy resolution of the SDHCAL as a function of beam energy.

The physics prototypes were developed to test the proof of principle. After having successfully tested these prototypes, the R&D program focuses on construction and testing

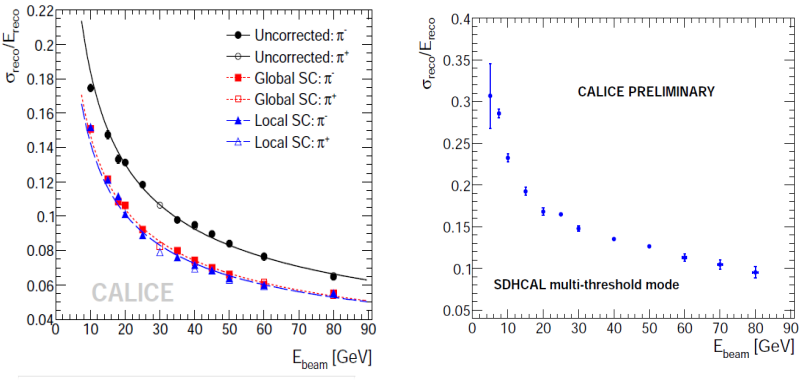


FIGURE 3.11: The HCAL energy resolution with pion showers. The left part shows the resolution as a function of beam energy for the AHCAL prototype, for showers starting in first 5 layers. The right part shows the energy resolution of the SDHCAL prototype.

of technological prototypes, and to address the engineering challenges of the proposed detectors.

### 3.4.4 The Magnetic Coil and The Muon Chamber

The ILD is designed to have a nominal magnetic field of 3.5 T with a maximal field of 4 T. The magnetic field is provided by a solenoid magnet, with a diameter of 6.88 m and a length of 7.35 m, placed between the HCAL and the muon chamber. The superconducting coil is made of 3 modules, which are electrically and mechanically connected. Each module has a length of 2.45 m and consists of 4 layers, with 105 turns per layer. An iron yoke will be used to provide flux return. It will consist of a barrel yoke and two endcap yokes. The total thickness will be 2.68 m in the barrel and 2.12 m in the endcaps. This iron yoke will also serve as the main mechanical structure of the ILD.

The Muon chamber/tail catcher will be used to detect muons and tails of hadronic showers. It is placed inside the iron return yoke. The iron serves as absorber material. The first section of the chamber consists of 10 layers, close together, separated by 10 cm thick iron layers. The second section of the chamber is used as a muon tracker, and these three layers are 60cm apart. Since the muon chamber/tail catcher system is situated after the magnetic yoke, which accounts for 2 $\lambda_I$ itself, it cannot contribute significantly to the jet energy reconstruction. To compensate for these limitations, the chamber starts with a sensitive layer, followed closely by several active layers.

## 3.5 Softwares and tools.

Software and simulation tools have been developed in the framework of the ILC. ILCSoft is the software framework used for analysis and simulation. It provides the main tools LCIO, GEAR, Mokka and Marlin. This set of tools has been used for the production of Monte Carlo events and for the results published in the Detector Baseline Design (DBD)[40]. The reconstruction tools have also been developed and tested with beamtest data. The PFAPandora package is used to apply the PFA to simulated data. Specific analysis oriented processors like LALLeptonFinder[79] and GARLIC[80] are also developed and tested.

The analysis presented in this thesis used LCFIPlus[105] and Zfinder processors in different sections. LCFIPlus is used for flavor tagging and locating the secondary vertex. The latest version of the software provides a good efficiency for both purposes. ZFinder was used to reconstruct the Z boson from its decay products and to correct for Bremsstrahlung.

The analysis tools have been regularly updated and improved. Since the release of LOI [63], the advanced techniques have been implemented to improve the analysis efficiency.

# Chapter 4

# Optimization of the Si-W ECAL guard ring size

## 4.1 Introduction

Optimization of the performance-to-cost ratio is one of the important aspects of the R&D program for the ILD. The Si-W ECAL 3.4.3.1 is the most expensive sub-detector of the ILD. An estimation published in the DBD [40], shows that the Si-W ECAL costs upto 40% of the total ILD cost. The design and cost of the Si-W ECAL has a strong impact on the overall cost of detector. The important parameters to optimize are the inner radius of Si-W ECAL, the number of layers, insensitive areas and sampling fraction. The cost of the detector varies with the total surface area of the detector and the number of channels, while its performance varies with the total thickness and sampling. The ILD Si-W will have a highly granular surface area of ~2500 $m^2$ in total.

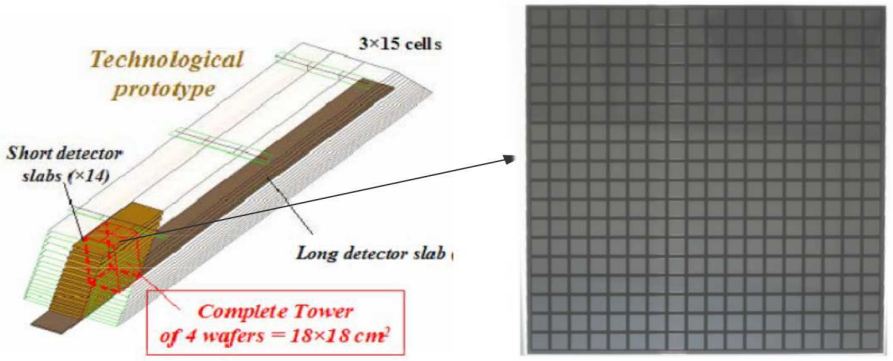


FIGURE 4.1: A schematic 3D view of the technological prototype of the Si-W ECAL. A silicon wafer is highlighted on the right.

Studies have been made to analyze the performance of the ECAL with a reduced number of layers and with different sampling fractions[87, 88]. Preserving the total thickness of absorber material, and varying its thickness in different stacks of layers has been studied. In this chapter, the optimization of the guard ring size will be discussed. The material used for guard rings is less expensive than the silicon used for the active layers. On the other hand, larger size of guard rings will result in an increase in dead zones in the ECAL, degrading its performance. To find a compromise between these two parameters, we study the physics performance of the ECAL, as a function of guard ring size.

Figure 4.1 shows an artistic view of a module of Si-W ECAL technical prototype. The left part shows a stack of layers, with four silicon wafer per layers. These wafers are separated by the guard rings between them. The red lines, drawn on the top layers, represent the position of guard rings. The gap between two consecutive wafers is called interwafer gap. The final design of ECAL of ILD will consist of 8 staves in the barrel region of the ILD. The gap between two staves is called interstave gap.

One wafer is highlighted in the right part, which is a matrix of silicon pixels, each measuring $5\times5$ mm$^2$. The wafer shown in figure, contains $18\times18$ cells, however, the final design will feature $16 \times 16$ cells.

The silicon wafers are surrounded by the floating guard rings. These guard rings are used to avoid leakage currents from one wafer to another and to allow the detector to operate in high voltage conditions. They are insensitive zones and their properties have been studied and understood [89]. In the Si-W ECAL of ILD, at their current size, guard rings occupy a total of 4.4% area.

## 4.2 Motivation

During the analysis of beamtest data of physics prototype of Si-W ECAL [96], an energy loss at the interwafer positions was observed. Figure 4.2 shows the mean value of raw energy as a function shower barycenter defined as:

$$(\bar{x}, \bar{y}) = \Sigma(E_i x_i, E_i y_i)/\Sigma E_i \tag{4.1}$$

It was estimated that the energy loss is 15% and 20% in x and y directions respectively. Comparatively smaller energy loss in x direction is due to the staggering of the gaps in this direction. A technique was devised to compensate for the energy loss at these positions and to have a rather uniform response from the calorimeter. This aspect emphasizes on the need of careful studies, to determine the effect of increasing the guard ring size, on

energy resolution of the ECAL. During this study we do not apply any corrections to the reconstructed energy, in order to see the effects of guard ring size.

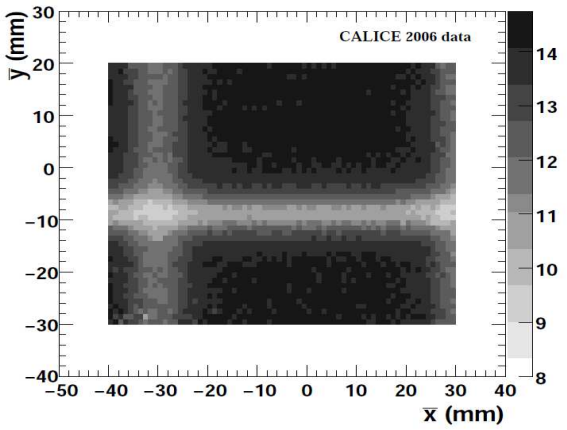


FIGURE 4.2: Energy loss at interwafer gaps of physics prototype of Si-W ECAL, during a beamtest in 2006. The incident beam consisted of electrons at 15 GeV. The figure is taken from [96].

The other aspect which makes it important to analyze the effect of guard rings, is the cross talk. The analysis of test beam data from physics prototype showed cross talk through the guard rings resulting in square events. In case of such events, we observe hits all around the edge of wafer, when shower hits the wafer. The frequency of these events was found to increase with the energy of primary electrons[102].

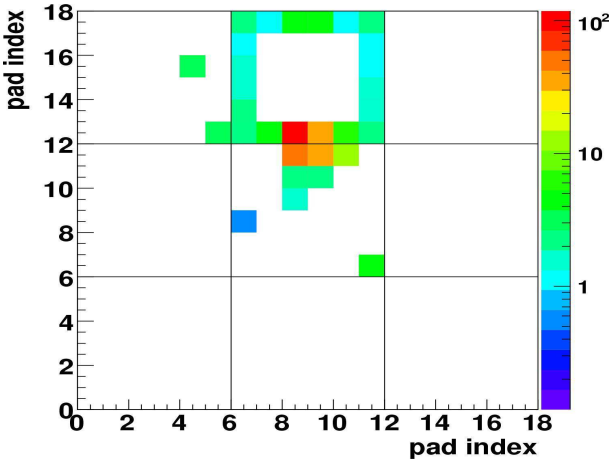


FIGURE 4.3: Example of square event along with normal event .

The figure 4.3 shows an example of a square event. The image is taken from [94].

## 4.3 Optimization studies of the guard rings

The goal of optimization studies is to study the physics performance of the Si-W ECAL with various guard ring sizes. In order to do that, two physics channels are studied. The contribution of ECAL to jet energy resolution is studied through the hadronic decay of Z boson at 91 GeV. The decay of Z boson to electrons, is used to study the electromagnetic energy resolution for various guard ring sizes.

The current guard ring size is 1 mm, called the standard size hereafter. The performance with this guard ring size will be compared with the previous results for a cross check.

A reasonable range for the guard ring size is between 0 and 2 mm but we include larger sizes (3, 5 and 8 mm) to see the propagation of effects on the energy resolution. The study is performed with Mokka 06-07 [97] and ILCSoft 01-10[98] is used for reconstruction. These are the standard simulation and analysis tools in the framework of ILD. The analysis part also uses Marlin and MarlinPandora and optimized reconstruction algorithms for different physics processes.

As described in the previous chapter, there are multiple options for the hadronic calorimeter of the ILD, including AHCAL, DHCAL and sDHCAL. For this study we use the AHCAL, as hadronic calorimeter.

## 4.4 Wafer Scan

Simulated photons, with an energy of 2 GeV, are sent into a specific part of the Si-W ECAL. These photons are smeared in polar angle $\theta$ and $\phi$ to target a selected region in the ECAL barrel.

As a cross check, Figure 4.4 shows the map of a layer hit by photons, where colors represent the number of hits in each cell. The inter-wafer and inter-stave gaps can be clearly seen. Along the $z - axis$, at 0 mm, the interwafer gap is narrower than the interstave gaps, at -90 and 90 mm respectively. The actual size of the guard ring for this image is 1 mm, but because the reconstruction of the hit position is done at the center of the cell, the gap appears to be bigger. It is also observed that gaps in y direction are more pronounced then those in $x-$direction. This is due to the staggering of the gaps in $x-$direction. The staggering is the relative shift in the position of layers to avoid the projected gaps.

After this cross check study, we proceed to look the their effect on the reconstruction of energy and hits.

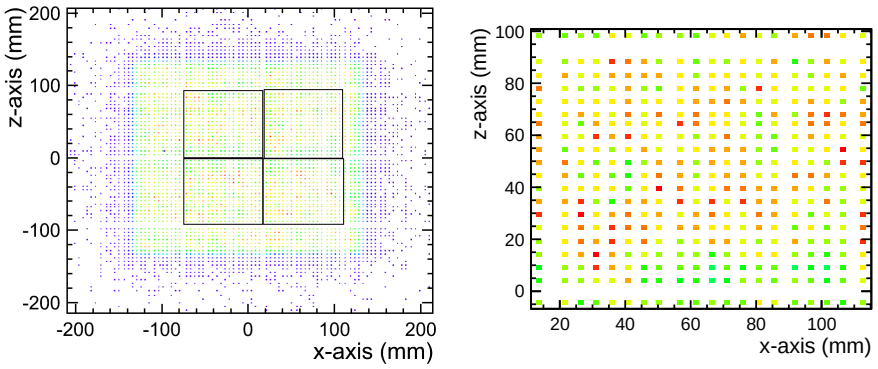


(a) (b)

FIGURE 4.4: A silicon layer hit by 2 GeV photons. In (a), the four wafers are separated by black lines, representing the position of the guard rings. The position of the interwafer and interstave gaps can be seen. In (b) a close-up of one wafer is shown.

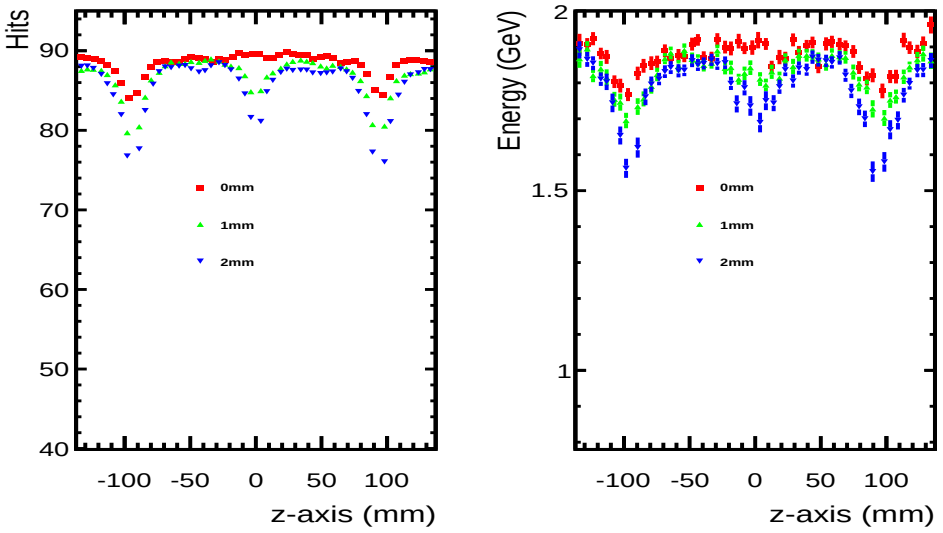


FIGURE 4.5: Reconstructed energy (right) and number of hits (left), for 2 GeV photons, as a function of position. Energy loss and hit loss can be seen at the interwafer and interstave gaps. The colors represent different guard ring sizes.

Figure 4.5 shows the number of reconstructed hits and reconstructed energy versus the position on z-axis. A drop in the number of hits and in the reconstructed energy is visible at the positions of the interwafer and interstave gaps. As expected, this drop increases with increasing guard ring size. In the absence of guard rings, the drop only occurs at the interstave gaps, as is shown by the red curve, representing the 0 mm guard ring size.

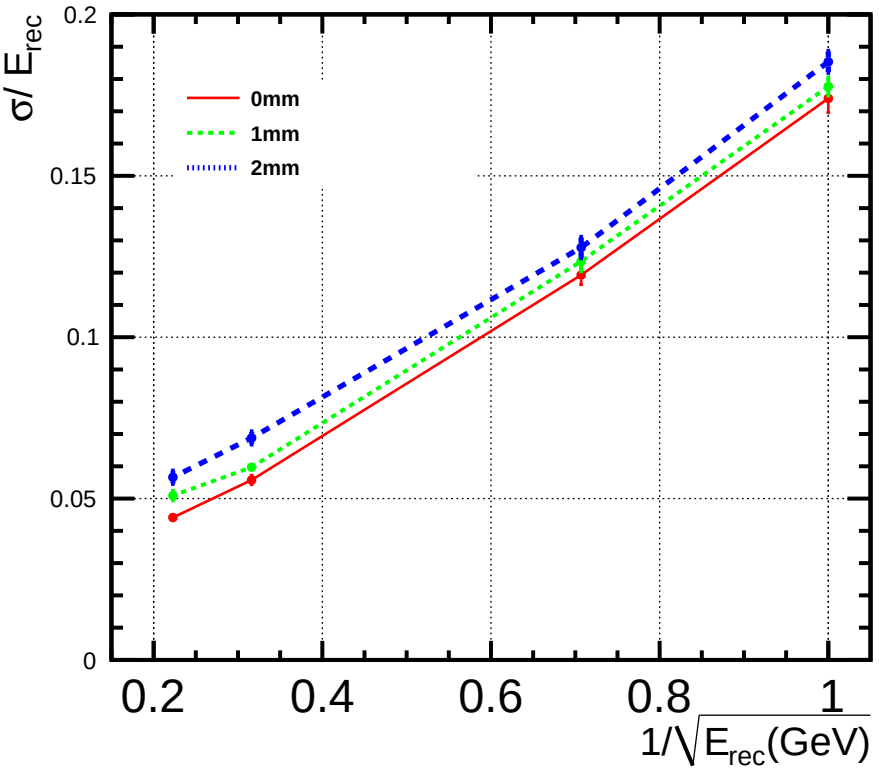


FIGURE 4.6: Variation in the electromagnetic energy resolution of the Si-W ECAL, for different guard ring sizes (0,1 and 2 mm). The energy of the incident photons varies between 1 and 20 GeV.

The energy loss at the interwafer and the interstave gaps degrades the electromagnetic energy resolution of ECAL. Figure 4.6 shows energy resolution for single photon events. It is clear that the energy resolution is degraded by the increase in guard rings size. The best energy resolution is naturally obtained without a guard ring as the the inactive area due to guard rings is minimum.

## 4.5 Physics Channels at the ILC

After the systematic studies with single photons we proceed now to study the impact of the guard rings on the physics performance of the Si-W ECAL. For this purpose, we investigate the hadronic ($Z \rightarrow uds$) and leptonic ($Z \rightarrow e^+e^-$) decays of Z. These two channels are of great importance at the ILC physics program.

### 4.5.1 $Z \rightarrow q\bar{q}$ Jets at 91 GeV

Many of the final states at the ILC will consist of hadronic jets. The ECAL plays an important part in the reconstruction of these jets. Jets contain photons coming from the decay of $\pi^0$. These photons carry ~30% of the total jet energy and are to be reconstructed in the ECAL. They may remain undetected due to non-sensitive detector parts. Therefore the jet energy resolution might be affected by the guard ring size.

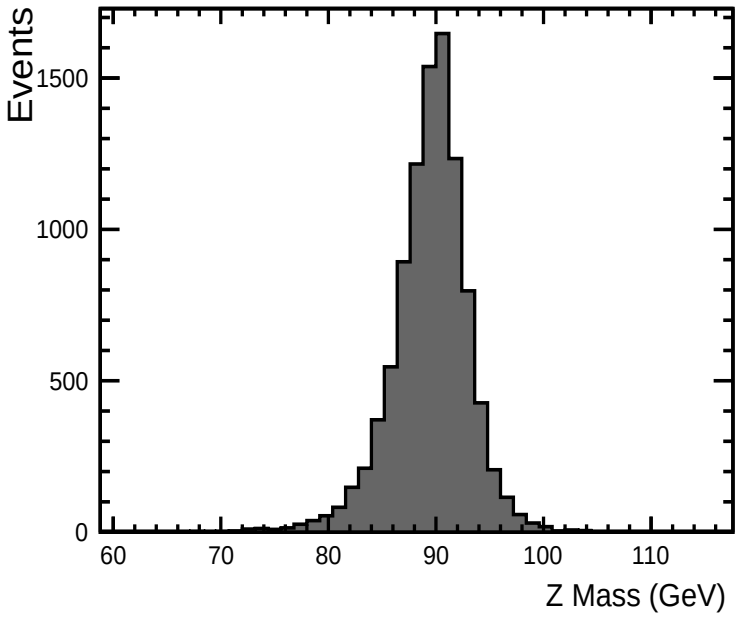


FIGURE 4.7: The reconstructed mass of Z decaying to $q\bar{q}$ pairs at $\sqrt{s}$ =91 GeV.

Moreover, ~50% of hadrons start showering in the ECAL[90]. A good energy resolution performance requires these showers to be reconstructed precisely. The inactive areas such as guard rings may compromise these measurements, even though most of the jet energy is deposited in the HCAL.

In order to see the impact on the jet energy resolution, we choose $Z \rightarrow u\bar{u}/d\bar{d}/s\bar{s}$ at a center-of-mass energy of 91 GeV. The Durham Jet algorithm [92] is used via the Satoru Jet Finder to reconstruct the jets. Figure 4.7 shows the reconstructed Z mass.

Two approaches are followed for the analysis: The Gaussian sigma and $\text{RMS}_{90}$. $\text{RMS}_{90}$ is the rms for the 90% events from the center of a Gaussian distribution. The purpose to use this approach is to reduce sensitivity to the non gaussian tails.

In order to see the effect of increasing guard ring size on the resolution, $\text{RMS}/\sqrt{E}$ and $\text{RMS}_{90}/\sqrt{E}$ are shown as a function of the cosine of the polar angle $\theta$ of the jets. From

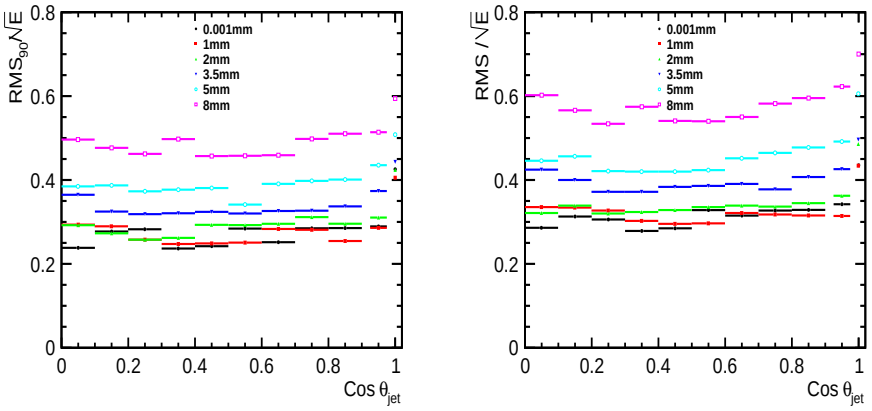


FIGURE 4.8: The jet energy resolution as a function of $\cos\theta_{jet}$, where $\theta_{jet}$ is the polar angle of jets along the z-axis. (a) shows the comparison of $RMS_{90}/\sqrt{E_{jet}}$ for various guard ring sizes. (b) is for the gaussian sigma ($RMS/\sqrt{E_{jet}}$).

figure 4.8, it can be seen that the energy resolution for jets degrades as the guard ring size increases, but up to 2 mm there is no significant degradation. For the standard size (1mm) the results for the jet energy resolution agree with those already published in the DBD [40].

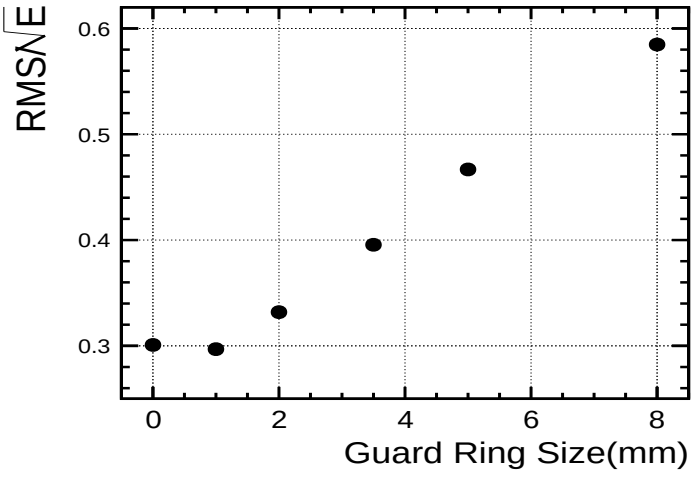


FIGURE 4.9: Jet energy resolution ( $\mathrm{RMS}_{90}/\sqrt{E}$) as a function of guard ring size.

Figure 4.9 shows the jet energy resolution, integrated over the polar angle, as a function of the guard ring size. For a guard ring size in range 0-2 mm, the degradation in resolution is very small.

### 4.5.2 $Z \rightarrow e^{-}e^{+}$ Channel.

The leptonic decay of the Z boson is one of the important channels for ILC physics. It is used for detector calibration, because of the high accuracy with which the Z mass (91.2 GeV) and its branching ratios are known. It is also a useful channel to evaluate the performance of the ECAL. At the ILC, this channel will be used to reconstruct the Higgs mass, by means of the Z recoil mass [100].

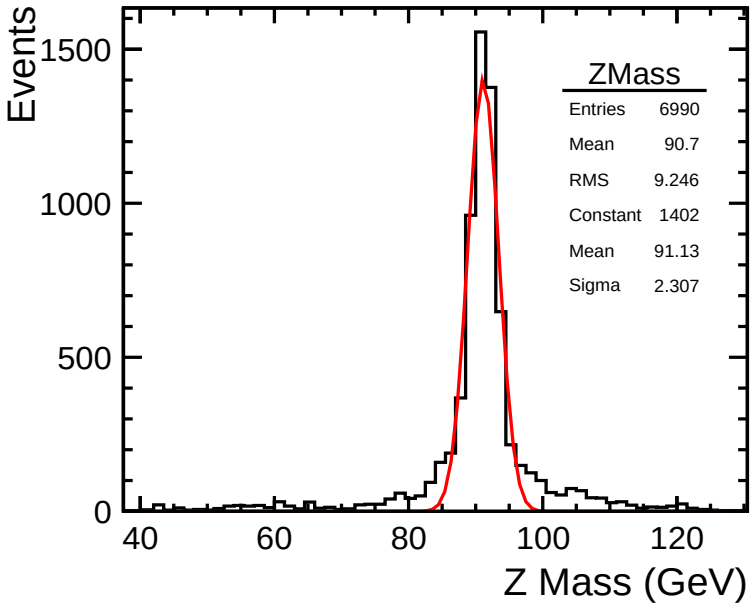


FIGURE 4.10: The Z mass from $Z \rightarrow e^{+}e^{-}$,fitted with a gaussian.

The leptonic decay of the Z bosons creates Bremsstrahlung photons, radiated by the electrons, that can be only reconstructed in the ECAL. The recovery of these photons is compromised due to the presence of inactive area.

We use polarized electron beams $(P_{e^-}, P_{e^+}) = (-0.8, +0.3)$ at $\sqrt{s} = 250GeV$ . The process studied here is $e^{-}e^{+} \rightarrow ZH$. The Z is reconstructed from its decay products using ZFinder[101], an algorithm to reconstruct the Z from electrons. It includes the recovery of Bremsstrahlung photons.

As this channel is very sensitive to modifications in the structure of the ECAL, we want to assure a good reconstruction. This is verified by a simple calculation for the resolution on the Z mass. As Z has a very mild boost, we can assume it is at rest and that its decay electrons have equal energy ($\frac{M_z}{2}$). The sigma for reconstructed Z mass can be expressed as:

$$\sigma(M_Z) = \frac{1}{2} \cdot \sigma(E_e) \cdot \left(\frac{M_Z}{E_e}\right)^2 \simeq 2 \cdot \sigma(E_e) \tag{4.2}$$

With the ECAL energy resolution $\sim 17\%$, we have

$$\sigma(E_e) = 0.17 \cdot \sqrt{E_e} = 1.15\,GeV \implies \sigma(M_Z) = 2.30\,GeV \tag{4.3}$$

The value found by the Gaussian fit in figure 4.10, is in agreement with this result. This cross check ensures the good performance of analysis and reconstruction tools. It also shows that the energy loss due to Bremsstrahlung photons is is well recovered by the reconstruction algorithm.

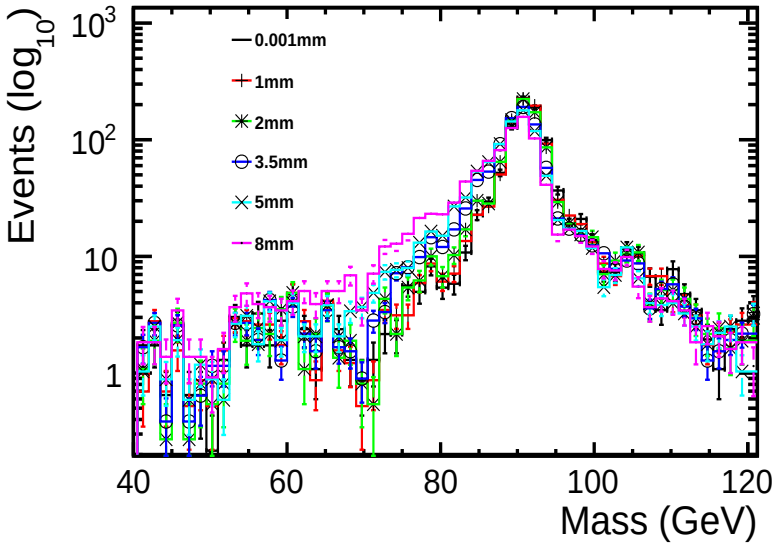


FIGURE 4.11: The distribution of mass of the Z, reconstructed from $e^+e^-$. The log scale is used to show propagation of tails with increasing guard ring size.

As is evident from the figure 4.10, the distribution of the mass of Z has tails on the right and left part, due to imperfections in the reconstructions. The propagation of these tails with the guard ring size has been studied, as is shown in the figure 4.11. The guard ring size within a reasonable range of 0-2mm has very little effect on the tails, how ever larger sizes increase the tails considerably. Although the difference is small for smaller sizes, but in order to preserve high precision the smallest possible guard ring size should be preferred.

As described earlier, the process studied here was $e^-e^+ \rightarrow ZH$, which is one of the benchmarks at ILC, for the reconstruction of Higgs boson. Although the main focus of

884 the studies was to reconstruct the Z from it's decay products, for the sake of completeness
885 the result Higgs recoil mass spectrum is also shown in figure 4.12.

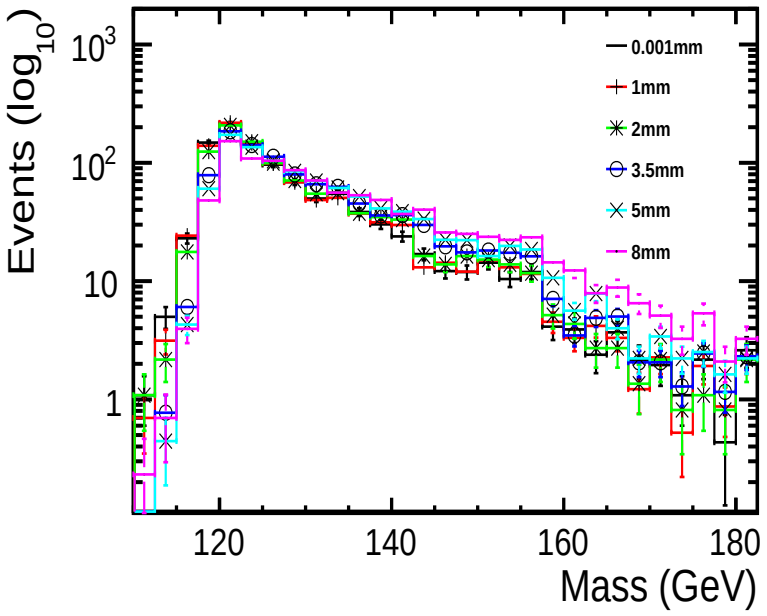


FIGURE 4.12: The Higgs recoil mass distribution, reconstructed using the method from [100]. The plot shows the effect on tails, with increasing guard ring size.

886 The electromagnetic energy resolution ($RMS/\sqrt{E}$) as a function of the guard ring size
887 is shown in figure 4.13. The effect is more pronounced, specially for smaller guard ring
888 sizes, as compared to the jet energy resolution. But again, we see that the resolution
889 degradation at smaller guard ring sizes is very small($\sim$ 2 %). Up to 2 mm, like in the
890 case of jets, the energy resolution of the ECAL is not affected severely.

## 891 4.6 Summary

892 We studied the energy resolution of the ECAL for hadronic and leptonic decays of Z for
893 different guard ring sizes ranging from 0 to 8 mm. In the case of jets we have studied
894 the energy resolution as a function of the jet polar angle. We observed that the energy
895 resolution depends on the guard ring size and that it is degraded when we go to larger
896 sizes, as we increase the dead area in the detector. We found that the energy resolution
897 varies very little for typical guard ring sizes i.e. between 0 and 2 mm. The study takes
898 into account the effects on physics performance. The effects on silicon wafers, for example
899 the square events, were not studied during this analysis.

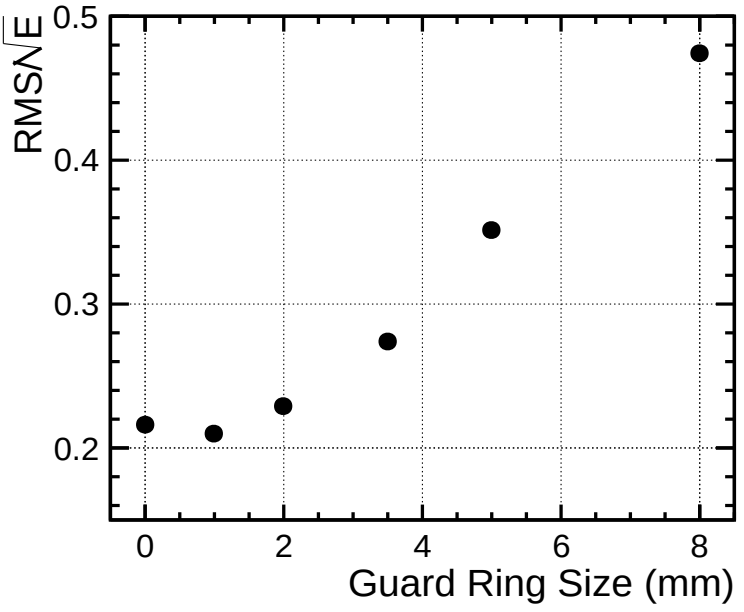


FIGURE 4.13: Electromagnetic energy resolution of ECAL as a function of guard ring size, for $Z \rightarrow e^+e^-$.

# Chapter 5

# Top quark forward backward asymmetry at the ILC

## 5.1 Introduction

As already explained in the section 2.5, the top quark is one of the important topics of study at the ILC. Due to its large mass, it is most strongly coupled to the mechanism of the electroweak symmetry breaking. For this and other reasons, the top quark is expected to be a window to any new physics at the TeV energy scale. In this chapter we will present the measurement of $t\bar{t}$ forward backward asymmetry at ILC, in hadronic decay channel.

## 5.2 Asymmetries at hadron colliders

The last few years were marked by a number of publications from the Tevatron experiments which reported on tensions with Standard Model predictions in the measurement of forward backward asymmetries $A_{FB}$. This observable counts the difference in the number of events in the two hemispheres of the detector. In hadronic collisions, the polar angle is typically expressed in terms of the rapidity $y$, which is invariant under longitudinal boosts.

Usually the analyses use the semi-leptonic decay channel, for example at the LHC and Tevatron. In this scenario, at least one member of the $t\bar{t}$ pair is required to decay leptonically to assure the particle identification. The average asymmetry reported by CDF is $0.201 \pm 0.065\,(\text{stat.}) \pm 0.018\,(\text{syst.})$ [112] which agrees with $0.196 \pm 0.060\,(\text{stat.})^{+0.018}_{-0.026}\,(\text{syst.})$ as reported by DØ [113]. These values can be compared with an asymmetry of about

922 0.07 predicted by the to Standard Model from NLO QCD and electroweak effects. This
923 result is difficult to verify at the LHC. The LHC is a proton-proton collider, so the two
924 hemispheres are intrinsically symmetric. Further, at the LHC at 7 TeV, only 15% of
925 the interactions arise from $q\bar{q}$ collisions; the 85% from $gg$ collisions can have no intrinsic
926 asymmetry. Still, in $q\bar{q}$ collisions at the LHC, it is likely that the $q$ is a valence quark
927 while the $\bar{q}$ is pulled from the sea. This implies that $t\bar{t}$ pairs produced from $q\bar{q}$ are
928 typically boosted in the direction of the $q$. This offers methods to observe a forward
929 backward asymmetry in $q\bar{q} \to t\bar{t}$. For example, a forward-backward asymmetry in the $\bar{q}$
930 reaction translates into a smaller asymmetry $A_C$ in the variable $\Delta|y| = |y_t| - |y_{\bar{t}}|$. For
931 this observable, CMS measures $A_C = 0.004 \pm 0.010\,(\text{stat.}) \pm 0.012\,(\text{syst.})$ [114], which
932 agrees with the Standard Model predictions within the relatively large uncertainties. So
933 far, the LHC experiments have not provided any independent evidence for asymmetries
934 outside the Standard Model predictions [104, 115]. The theoretical interpretation of
935 these asymmetries is also very uncertain. Many plausible models of the $t\bar{t}$ asymmetry
936 predict effects in top quark physics at high energy that are excluded at the LHC. For a
937 review of the current situation, see [116, 117].

## 938 5.3 Asymmetries at the ILC

939 The top quark physics program at ILC has been discussed in chapter 2. In this chapter,
940 the focus will be on studies carried out to measure the forward backward asymmetry in
941 top pair production at the ILC, with the help of full detector simulations.

942 Figure 5.1 shows the Born level $A_{FB}$ for different particles, as a function of center-of-
943 mass energy, with unpolarized beams and neglecting the effect of initial state radiation
944 (ISR).

945 It can be seen that the value of $A_{FB}$ for the top quark is around 0.40 at a center-of-mass
946 energy of 500 GeV. This value is however, for unpolarized beams. With polarized beams
947 the values of $A_{FB}^{top}$ are given below.

948 – $\{P_{e^-}, P_{e^+}\} = (-1, +1)$, $A_{FB}^{top} = 0.47$

949 – $\{P_{e^-}, P_{e^+}\} = (+1, -1)$, $A_{FB}^{top} = 0.38$

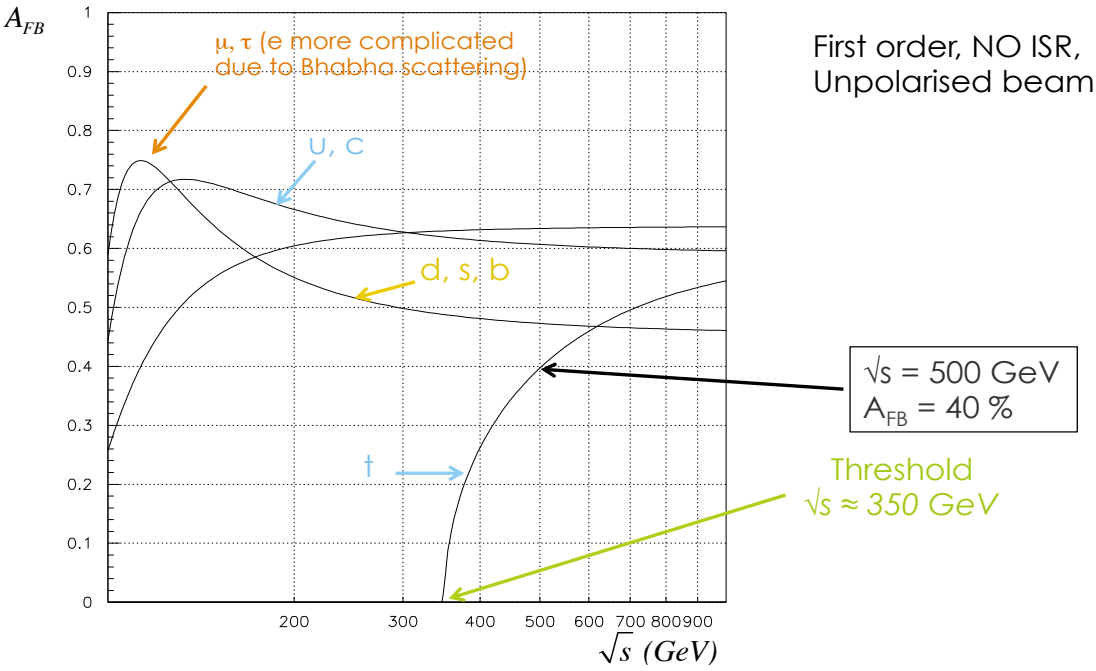


FIGURE 5.1: Forward Backward asymmetry $A_{FB}$ for different particles produced in Z decay, as a function of center-of-mass energy $\sqrt{s}$.

## 5.4 Production cross sections at the ILC and beam polarizations.

For polarized electron-positron beams, the production cross section for any particle through $e^-e^+ \to X$, can be expressed as[107]:

$$\sigma_{P_{e^-},P_{e^+}} = \frac{1}{4}\left[(1-P_{e^-}P_{e^+})(\sigma_{-,+}+\sigma_{+,-}) + (P_{e^-}-P_{e^+})(\sigma_{+,-}-\sigma_{-,+})\right] \tag{5.1}$$

Here, $P_{e^-}$ and $P_{e^+}$ represent the degree of polarization of electron and positron beams respectively. This expression assumes $m_e/E \to 0$, which is valid for $\sqrt{s} >> m_e$. In this case, the terms like $\sigma_{+,+}$ and $\sigma_{-,-}$ don't contribute to the cross section due to the helicity conservation in the massless limit. The cross section varies for different beam polarizations. The cross section for $t\bar{t}$ production for left-handed electron beam polarization is much larger than that for right-handed electron beam.

A graphical representation for the production cross section of different Standard Model physics channels at ILC, including $t\bar{t}$, is shown in figure 5.2, for an energy range between 0 and 1 TeV.

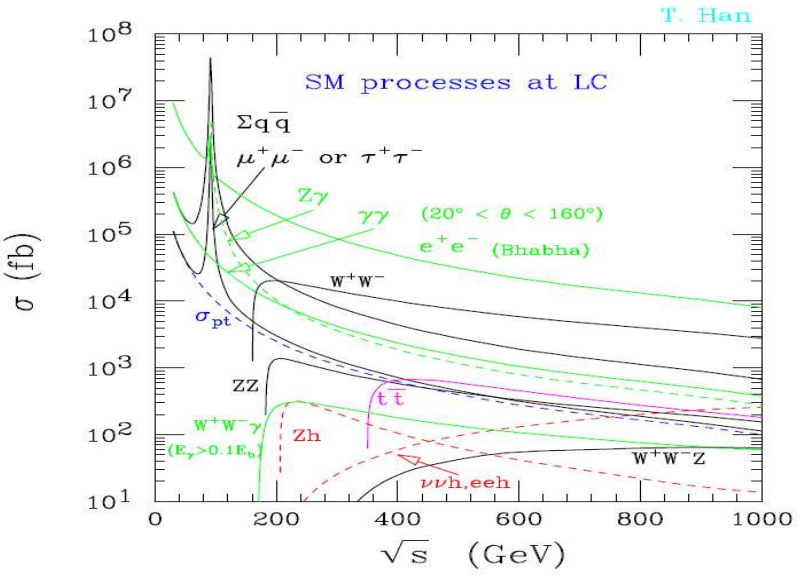


FIGURE 5.2: Unpolarized cross sections for different Standard Model processes at the ILC, as a function of center-of-mass energy $\sqrt{s}$. The image is taken from [106].

The numerical values for cross sections of some of these processes, including major background processes, for $t\bar{t}$ studies, are shown in Table 5.1. These values are for a center-of-mass energy $\sqrt{s} = 500\text{GeV}$.

| Channel | Unpolarized(fb) | $e^-_L e^+_R$ | $e^-_R e^+_L$ | $A^0_{LR}(\%)$ |
|---|---|---|---|---|
| $t\bar{t}$ | 572 | 1564 | 724 | 36.7 |
| $b\bar{b}$ | 372 | 1212 | 276 | 62.9 |
| $\sum_{u,d,s,c} q\bar{q}$ | 2208 | 6032 | 2793 | 36.7 |
| $\mu\mu$ | 456 | 969 | 854 | 6.3 |
| $WW$ | 6603 | 26000 | 150 | 98.8 |
| $ZZ$ | 422 | 1106 | 582 | 31.0 |
| $ZWW$ | 40 | 151 | 8.7 | 89 |

TABLE 5.1: Production cross-sections of some important channels at the ILC, with unpolarized and fully polarized beams, at a center-of-mass energy $\sqrt{s}$ =500GeV. The last column represents the left-right asymmetry $A^0_{LR}$. [120]

The fully hadronic decay of $t\bar{t}$ pairs, is a benchmark in the DBD [40]. It accounts for 46% of the total top quark decay. A schematic view of the process is shown in figure 5.3. The advantage of using this channel is that the kinematic variables of the top decay can be reconstructed more precisely, as the final state can be fully reconstructed. In the semi-leptonic or fully leptonic decays, the W boson decays into a lepton and it's corresponding neutrino. The reconstruction of this W becomes less precise since the neutrino escapes

the detector. The hadronic decay channel on the other hand, allows a full exploitation of $t\bar{t}$ sample.

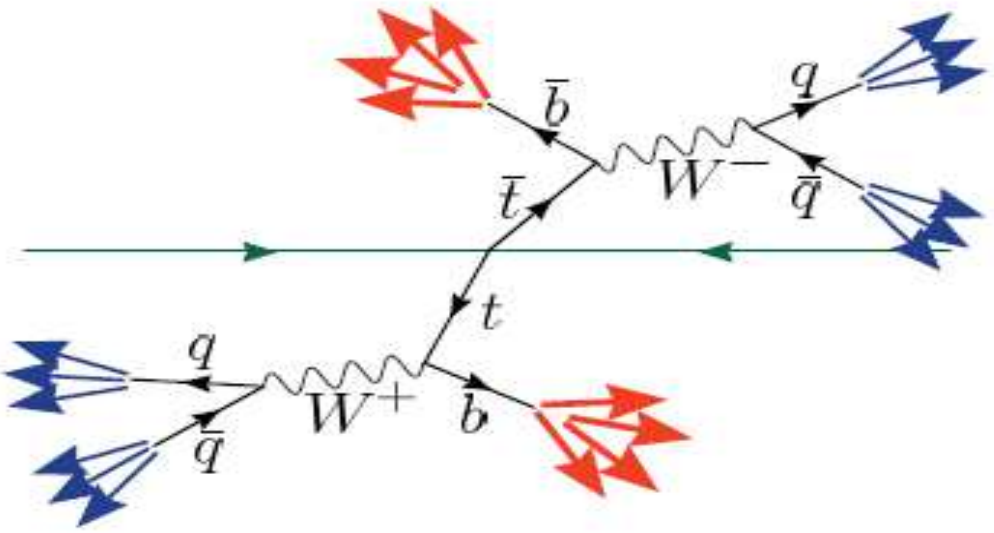


FIGURE 5.3: A schematic view of the fully hadronic decay of top quark pairs.

## 5.5 Studies

Fully polarized beams are used for the analysis of the fully hadronic decay mode of the top quark, to measure the forward backward asymmetry at the ILC, at 500 GeV center-of-mass energy. The following two beam polarization configurations are studied.

- For the left-handed electron configuration $e^-_L e^+_R$, we use $\{P_{e^-}, P_{e^+}\} = (-1, +1)$.
- While for the right-handed configuration $e^-_R e^+_L$, $\{P_{e^-}, P_{e^+}\} = (+1, -1)$

The beams at the ILC, will not be 100% polarized, rather the electron beam can be polarized upto 80%, and the positron beam upto 30%. This implies that the effective polarization $P_{eff}$, which is defined as follows,

$$P_{eff} = \frac{|P_{e^-}| + |P_{e^+}|}{1 + |P_{e^-}||P_{e^+}|} \tag{5.2}$$

will be around 90%.

The $t\bar{t}$ events are generated by `Whizard` version 1.95 [109, 110]. The parton showering and hadronization is done by PYTHIA 6.422 [93]. `Whizard` produces a six-fermion final state, of which $t\bar{t}$ is a sub-sample.

An integrated luminosity of 250 fb$^{-1}$, for each polarization configuration, is then subjected to a full detector simulation. The reconstruction is done with `ILCSoft v01-16`. Durham jet algorithm [92] is used for jet clustering. $K_t$ algorithms [82] are used to remove the gamma gamma background. The`LCFIPlus` package plays a central role in the analysis. A brief description of `LCFIPlus` is given in the next section.

## 5.6 LCFIPlus

`LCFIPlus`[105] is used for jet finding, vertex finding, flavor tagging and reconstruction of the vertex charge. Initially designed for the optimization of vertex detector design, the software package currently provides tools for reconstruction of all physics processes, where locating the vertex and reconstructing its charge is required. The package consists of multiple algorithms used for different tasks.

The jet finding part is based on the principle used in the Durham jet algorithm[92]. In the initial part, every hit or track is treated as jet, and starting from one such jet, the near by jets are added to the previous one, thus reducing the number of jets by 1, at each step. At each step, a distance $Y(i,j)$ between two jets $i$ and $j$ is computed for the pair of jets as follows:

$$Y(i,j) = \frac{2min(E_i, E_j)^2(1-\cos\theta_{ij})}{Q^2} \tag{5.3}$$

Where $E_i$ and $E_j$ are the jet energies, $\theta_{ij}$ is the angle between the two. $Q^2$ is constant, which is typically center-of-mass energy. Two jets with a minimal $Y(i,j)$ are combined into a single jet. The process is continued, till the required number of jets is achieved.

After finding the jets, the vertex finding is performed in two steps: namely finding the primary vertex, and the secondary vertex. The vertex locator part of the algorithm is a complete re-implementation of the vertex finder ZVTOP, developed at the SLD experiment [111]. For the most part the LCFIVertex algorithm is as the original ZVTOP. Improvements like using the Kalman vertex fit and adjustments to allow the use of ZVTOP for events at center-of-mass energies above the Z resonance are made to adopt to the requirements.

The tracks are combined to form a vertex, using $\chi^2$ minimization. The tracks with a $p_t$ less than 100 MeV, are discarded. Further parameters taken into account are the number of tracks, the distance from the IP, the probability of secondary vertex and the decay length.

The flavor tagging part of the algorithm uses the secondary vertex information, whenever available. A neural network uses separate sets of variables depending on whether a secondary vertex is found or not. The choice of the neural network architecture and input variables is flexible. The actual choice of these parameters is defined by the external weight files, produced by using dedicated samples, at the time of running the algorithm. These weight files are prepared to optimize the performance of the `LCFIPlus`, for different conditions like number of jets in final state, center-of-mass energy and detector geometry.

The discrimination of different types of jets uses the flavor of hadrons. The fact that *uds* jets do not contain vertices stemming from the decays of heavy flavor hadrons, helps to distinguish $c$ jets from them. Significant attention is also paid to sort out the unwanted vertices corresponding to photon conversions, and decay of $K_s$ and $\Lambda$ particles.

The discrimination of $b$ and $c$ jets is done using the output of dedicated neural networks. Three sets of neural networks are trained depending on whether 1, 2 or at least 3 vertices are found for the jet. The discrimination of the $c$ jets from the lighter quarks is easy. The "$b$ nets" are trained by providing $b$ jets as signal sample, and $c$ jets and lighter quarks as background. Similarly, "$c$ nets" are given $c$ jets as signal, and $b$ jets and lighter quarks as background.

A good flavor tag is a pre-requisite for the determination of the charge. This part of the reconstruction chain is the most crucial to analysis presented in this thesis. The b-quark decay chain is complex, and reconstruction of its charge is a difficult task in a multijet environment.

The measurement of the b-jet charge is done using the tracks associated to the vertex. The charge of individual tracks needs to be measured with good accuracy. Charge of all tracks, associated to the vertex of b-jet is summed to obtain the charge of b quark. During this analysis, the charge was measured at the secondary vertex, whenever available, to be used for identification of b-jets. The current version of the `LCFIPlus` is not yet optimized for the charge measurements.

## 5.7 Analysis and Kinematic Cuts

The $t$ quark decays nearly exclusively into a $b$ quark and a $W$ boson. The $b$ quarks hadronize into a jet, called $b$ jet hereafter, which contains a $B$ hadron. The six jet final state is reconstructed using the Durham jet finder [92]. Subsequently the jets are analyzed with the `LCFIPlus` package, which assigns a $b$ likeness called b-tag to the jet. Figure 5.4 shows the quality of b-tag as a function of polar angle of the jets. The two jets with the highest b-tag values are considered to be the jets from the $b$ quarks. The

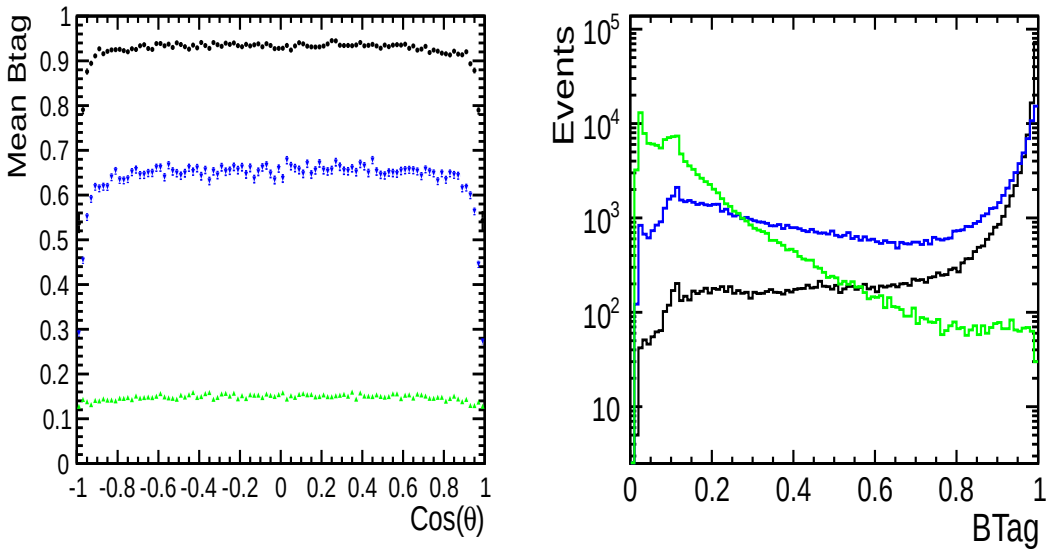


FIGURE 5.4: Left: The b-tag of the first three jets, classified on the basis of b-tag value, shown as a function of cos($\theta$) of the jets. Right: The distribution of b-tag, for three jets.

likelihood of third jet is also shown in the figure. As the figure shows, the mean value of the second highest b-tag is above 0.3. The right part of figure shows the distribution of b-tag. A little spike for the second $b$-jet, can be seen around btag value 0.2. These jets are either in very forward region, or soft $b$-jets.The events with b-tag values less than 0.3 are rejected, as a pre-selection for charge measurement.

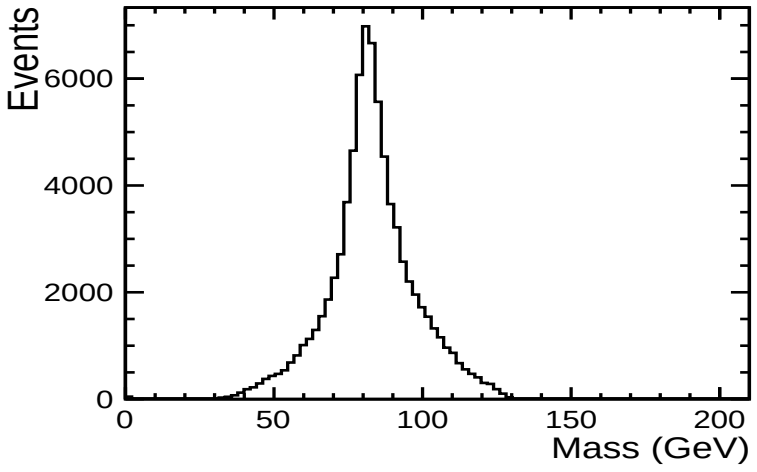


FIGURE 5.5: Reconstructed mass of the W bosons, from jets. Two Ws are selected from the combination of four jets, for which the variable $\psi$ has a minimum value

The possibility of $c$-jet being mistagged as a $b$-jet is also investigated. It was found that around 7% of the $b$-jets, could be the mis-tagged $c$-jets.

The two $W$ bosons are reconstructed from the remaining four jets. Different combinations of jets are checked for choosing the two Ws. A variable $\psi$ is defined as:

$$\psi = |m_{ij} - m_W| + |m_{kl} - m_W| \tag{5.4}$$

Here, ij and kl represent different possible combinations of jets and $m_W = 80.4$ GeV, is the mass of W boson. The minimum value of $\psi$ is used to reconstruct the required Ws. Figure 5.5 represents the mass distribution of the selected W candidates.

After having reconstructed the jets from $W$ bosons and $b$ quark jets, the jets are combined to form $t$ quarks. Out of two possible combinations of two $b$ jets with these Ws, $Top = W_i + b_k$ with $i, k = (1, 2)$, two tops are reconstructed with the minimal $\chi^2$.

$$\chi^2 = \left(\frac{m_t - 174GeV}{\sigma_{m_t}}\right)^2 + \left(\frac{E_t - 250GeV}{\sigma_{E_t}}\right)^2 + \left(\frac{p_b^* - 69GeV}{\sigma_{p_b^*}}\right)^2,$$

with

$$p_b^* = \gamma p_b(1 - \beta_t \cdot \cos(\theta_{tb}))$$

being the momentum of the $b$ quark in the rest frame of the $t$ quark, $E_t$ the energy of the $t$ quark candidate and $m_t$ the reconstructed mass of the $t$ quark. The variables $\sigma_{m_t}$, $\sigma_{E_t}$ and $\sigma_{p_b^*}$ expressed in the above equation are calculated from the distributions of $m_t$, $E_t$ and $p_b^*$, respectively. They take the following values.

$$\sigma_{m_t} = 6.3\,GeV, \quad \sigma_{E_t} = 8.0\,GeV, \quad \sigma_{p_b^*} = 10\,GeV. \tag{5.5}$$

The left part of figure 5.6 represents the value $\chi^2$ versus reconstructed mass of top, while right part shows $\chi^2$ versus the reconstructed energy of top. The concentration of events in the bottom part, around the nominal mass and energy values of top quark, shows the discrimination power of the $\chi^2$ method.

The defined $\chi^2$ is a quality criterion for the events and only events that satisfy $\chi_1^2 < 20$ and $\chi_2^2 < 40$ are retained. Systematic studies, performed by varying the $\chi^2$ cut, will be discussed in section 5.14. Finally, events are selected for which both $t$ quarks and both $W$ bosons are in the range $140 < m_t < 210$ GeV and $60 < m_W < 100$ GeV. The efficiency of these cuts is given in table 5.3.

The mass distribution of two selected top quarks is shown in figure 5.7.

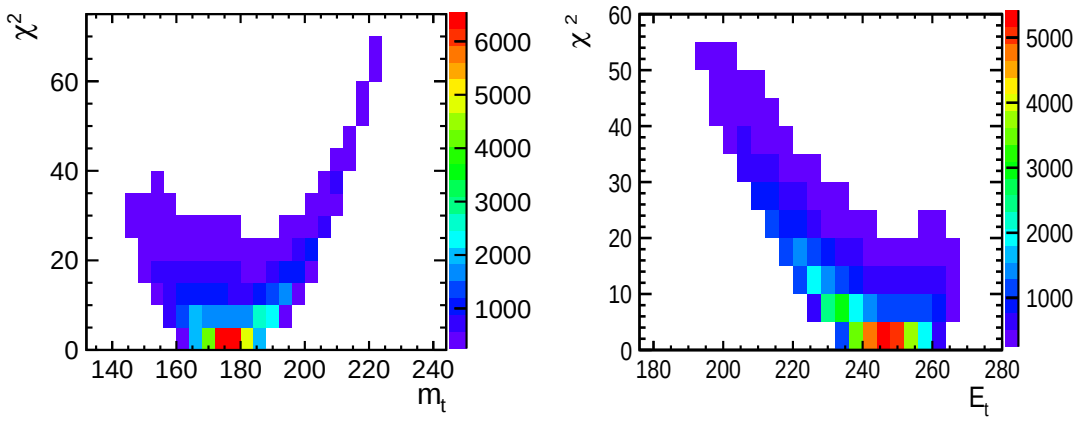


FIGURE 5.6: $\chi^2$ values plotted against the mass of the top quark candidate Left and it's energy Right. The $\chi^2$ distribution for maximum events is closed to the nominal values of mass and energy, as expected.

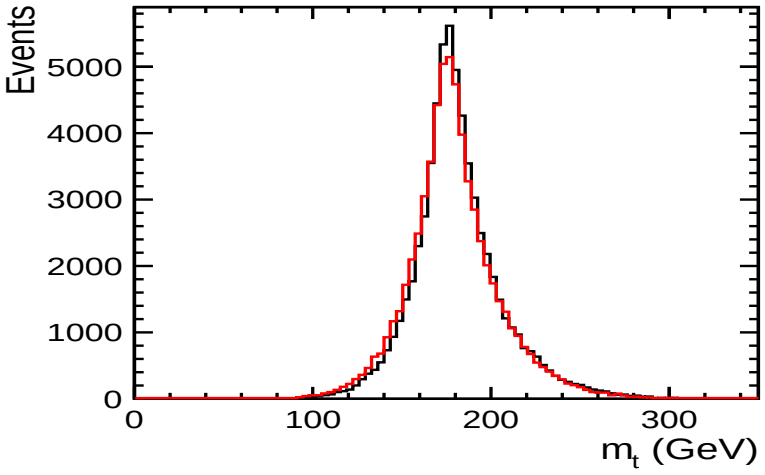


FIGURE 5.7: Mass distribution of the top quarks, selected using the $\chi^2$ criterian. Two curves represent the $t$ and $\bar{t}$ quarks.

All introduced event selection criteria are summarized in Table 5.2.

| Selection of the signal events | | |
|---|---|---|
| Cut number | Cut Name | *Type* |
| 1 | b-tag | $\mathrm{b\,tag_{1,2}} > 0.3$ |
| 2 | $\chi^2$ | $\chi^2 < 30$ |
| 3 | Kinematic | $140 < m_t < 210 GeV$ |
| Cuts used for the identification of the top quark charge | | |
| 4 | Jet Charge Cut | $Q_b < 5$ |
| 5 | Event Charge | $C \neq 0$ |

TABLE 5.2: Cuts as applied in this analysis in the sequence as they appear in the text.

The efficiency of the first set of cuts, used to select the signal events, will be given in table 5.3. The statistical error obtained for the cross section of $t\bar{t}$ hadronic decay, using these cuts, is 0.40% for the left-handed beam polarization, and 0.60% for the right-handed polarization.

## 5.8 Standard Model background

The backgrounds studied during the analysis are classified on the basis of the number of fermions. The background processes have already been shown in table 5.1, along with the corresponding cross sections.

The 6-fermion background is divided in two parts. The first part consists of $ZWW$, which can have a 6-jet final state. It has been shown that the rejection of this background can be easily done. One of the criteria to recognize such a background is the invariant mass of the $b\bar{b}$ system. As the figure 5.8 shows, there is a clear peak around the $Z$ mass.

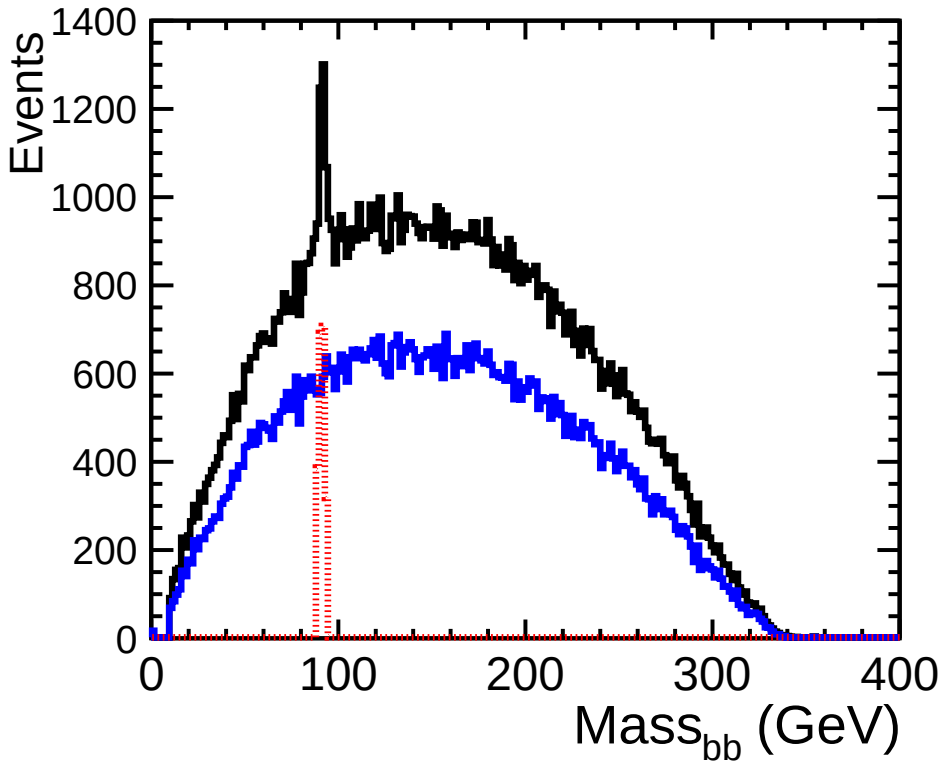


FIGURE 5.8: Mass distribution of $b\bar{b}$ system. The ZWW background can be seen peaking at $Z$ mass. The plot shows solid black line for all events, red dotted line is recognized as $ZWW$ background. The blue curve shows the events slected after removing the background.

The second part of 6-fermion background studied is the the semi-leptonic decay of $t\bar{t}$ pairs. The semi-leptonic events can migrate into hadronic due to multiple reasons, mainly hard gluon radiation, $\gamma\gamma$ background, and jets with multiple vertices. While studying this background, the reconstruction is forced to treat the leptons from the W decay, as jets.

The next type of background processes is 4-fermion background. Two processes are studied namely $WW$ and $ZZ$. The $WW$ background has the highest cross section, while the $ZZ$ background can be misleading, specially in cases where $Z$ decays to $b\bar{b}$. Only fully hadronic decay of the $Z$ and $W$ bosons are studied.

The requirement of two bjets with a b-tag value higher than 0.3, is a strong cut against the $WW$ background, which has the highest cross section among the background processes. Given that the $Z$ bosons can decay to $b\bar{b}$, this cut is less efficient in this case, but the next cuts on the kinematics of the top quark candidates and $\chi^2$ give good performance for rejection of this background.

| Process | Total Events | b-tag | Kinematic | $\chi^2$ | Efficiency |
|---|---|---|---|---|---|
| $t\bar{t}_{had}$ $(e^-_L e^+_R)$ | 162128 | 104710 | 80780 | 56598 | 34.90% |
| $t\bar{t}_{had}$ $(e^-_R e^+_L)$ | 63976 | 41325 | 32884 | 24228 | 37.87 % |
| $t\bar{t}_{sl}$ $(e^-_L e^+_R)$ | 102255 | 53090 | 26531 | 5280 | 5.16 % |
| $t\bar{t}_{sl}$ $(e^-_R e^+_L)$ | 52012 | 28722 | 14235 | 3084 | 5.92 % |
| $WW(e^-_L e^+_R)$ | $6.5 \times 10^{6}$ | 39084 | 7442 | 2163 | 0.03 % |
| $ZZ(e^-_L e^+_R)$ | 276500 | 35027 | 8770 | 2929 | 1.05 % |
| $ZZ(e^-_R e^+_L)$ | 145500 | 18006 | 4373 | 1501 | 1.03 % |
| $Z \to q\bar{q}$ $(e^-_L e^+_R)$ | $8.11 \times 10^6$ | 94226 | 21270. | 5530 | 0.06 % |
| $Z \to q\bar{q}(e^-_R e^+_L)$ | $4.5 \times 10^6$ | 31877 | 7874 | 2286 | 0.05 % |

TABLE 5.3: Efficiency of different cuts, for he signal and Standard Model background processes. The respective beam polarizations are shown in parentheses. The last column shows the final selection efficiency.

2-fermions background is also studied, for the sake of completeness. The hadronic decay of $Z$ boson is studied for both polarizations. Despite a high cross section, this process can be easily discriminated because of requirement of 6 jets. The final efficiency for this process is below 0.1%.

The efficiency of various cuts is summarized in the table 5.3. The number for background events are scaled to correspond to the same luminosity of 250 fb$^{-1}$.

## 5.9 Charge of the b quark

The $b$ quark charge $Q_b$ at the vertex is determined to identify whether it came from a $t$ or $\bar{t}$ quark. Technical details of measuring the vertex charge, are given in appendix A.

In this section the quality of charge reconstruction and the rejection of $\gamma\gamma$ background will be discussed.

### 5.9.1 Quality of the charge reconstruction

The charge at the vertex is reconstructed as the sum of the charge of all particles related to this vertex. For both jets $|Q_b| < 5$ is required, otherwise the event is rejected. The algorithm gives integral values for the quark charge instead of partial values for the charge of quark.

In order to verify the charge reconstruction it is compared with $b$ quark and $\bar{b}$ quark in the event generator record. Additionally, a cross check is performed using $B$ mesons, which are formed from the $b$ quark. The Fig. 5.9 shows in its left part the measured jet charges originating from $b$ or $\bar{b}$ quarks. The right hand part is the same but now the reference charge is given by a $B$ meson in the jet. For about 60% events, the charge of the original particle is reconstructed correctly. The distributions are compatible with those shown in Ref. [108]

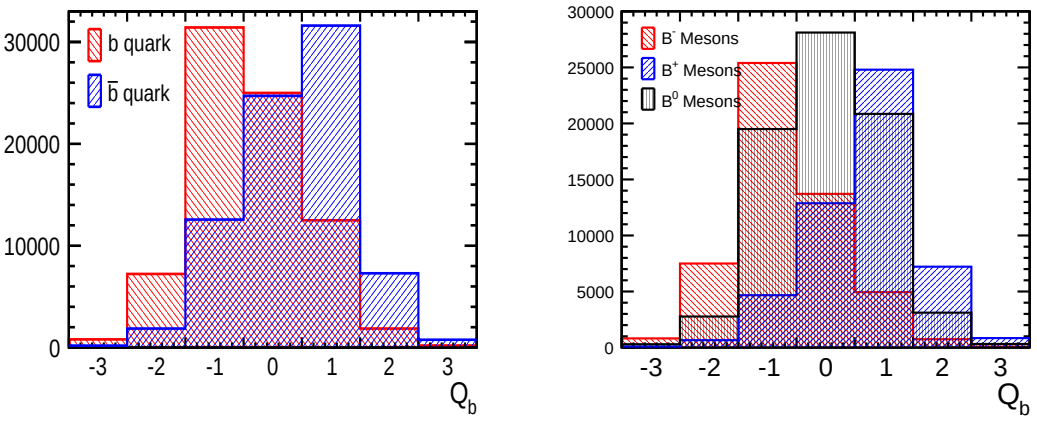


FIGURE 5.9: Left: Reconstructed charge for jets originating from $b$ or $\bar{b}$ quarks. Right: The charge of the $B$ meson is taken as a reference for the verification of the vertex charge measurement.

### 5.9.2 $\gamma\gamma$ background

One of the major backgrounds expected at the ILC stems from photon-photon collisions. These photons are radiated by electrons in the beam and are called Beamstrahlung photons. The cross section for such collisions is a few 100 nb, for incoherent photons. For each bunch crossing, approximately one such collision is expected. These collisions produce low $p_t$ hadrons. The data samples used for this study take this effect into

account. The samples were simulated with $\gamma\gamma$ collisions overlaid. The soft quark jets produced in this case are one of the sources of confusion for jet clustering and flavor tagging. Of special importance are the jets produced in the very forward region of the detector. To take away the effects of this background, we use the $k_t$ algorithm [82] to remove these low $p_t$ hadrons, before jet clustering and flavor tagging.

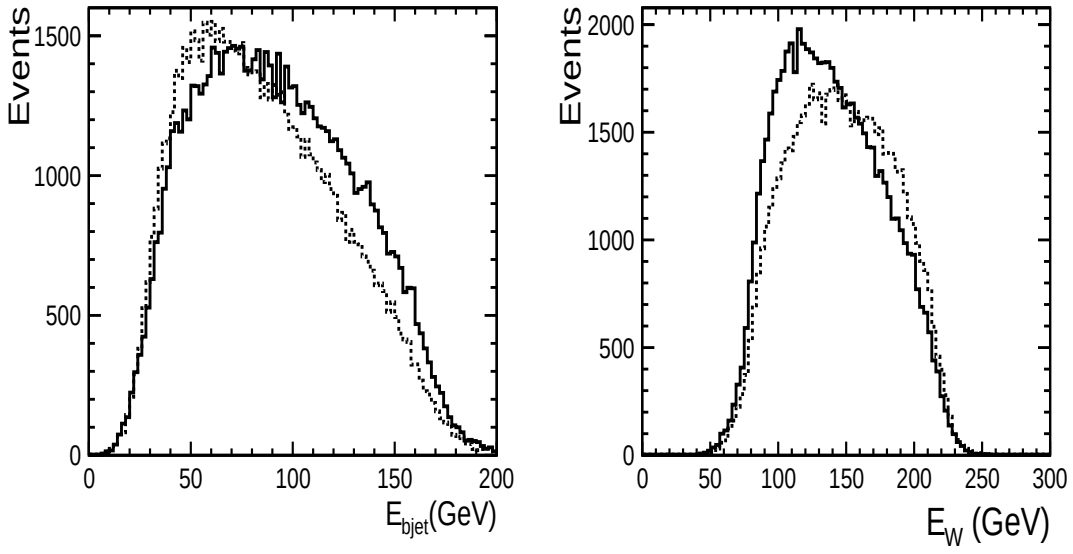


FIGURE 5.10: Comparison of the energy of the $b$ jets, and W bosons, in $t\bar{t}$ decay production, for left-handed and right-handed electron beams. The dotted line represents the right-handed electron beams, while solid lines are for left-handed electron beam case.

The effect of the background on b-charge measurement in both polarization configurations is not the same. The background affects the right-handed electron beam case in a stronger way as compared with the left-handed electron beam. The reason for this is that in case of left-handed electron beams, the b-jets are more energetic, while they are comparatively soft for right-handed electron beams. This is because of the $V-A$ structure of the $tWb$ decay vertex. On the other hand, the energy of the Ws behaves conversely i,e. Ws are more energetic in the right-handed electron beam case, as the figure 5.10 shows.

[106]

Figure 5.11 shows the effect of $\gamma\gamma$ background on the reconstruction of charge, for the right-handed electron beams with polarization $(P_{e^-}, P_{e^+}) = (+1, -1)$. However, the effect of background on left-handed polarization has also been studied, and it was found that the removal of background had a smaller effect as compared to right-handed polarization.

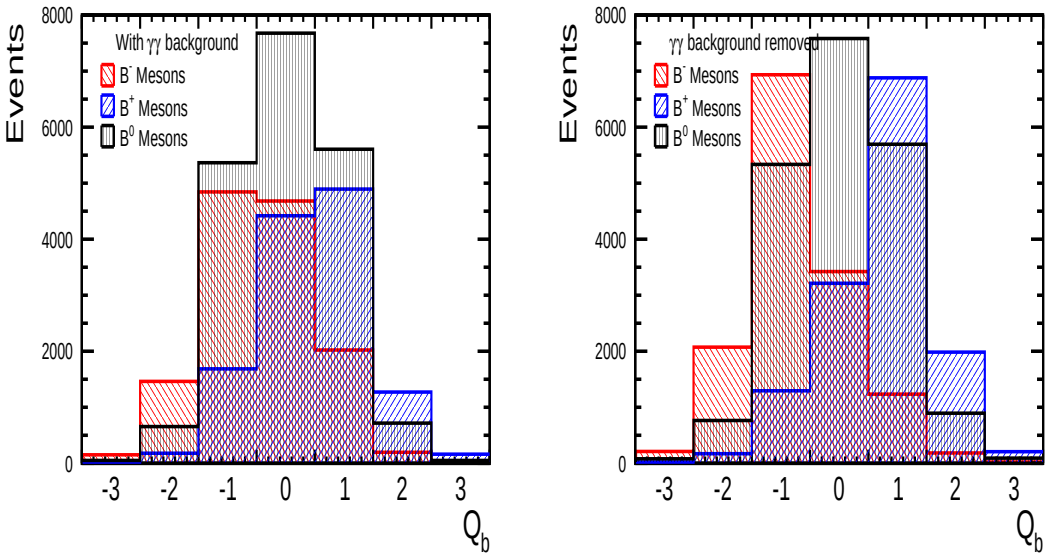


FIGURE 5.11: Left: Reconstructed charge for b-jets, using B-Meson charge for verification, with $\gamma\gamma$ background. Right: After removing the background using $k_t$ algorithm.

## 5.10 Mis-tagging of $c$-jets as $b$-jets

A clean reconstrcution of $b$-jets is vital to a good measurement of the direction of top quark, which is in turn used to calculate the forward-backward asymmetry. Separating the $b$-jets from $c$-jets is a difficult task, and there is always a probability of $c$-jet being mistagged as $b$-jet. A dedicated study is performed to understand this problem, with the help of the generated events. The studies are performed using the angle between the generated $b$,$c$ quarks and the reconstructed $b$-jets ($\theta_{b_{rec}b_{MC}}, \theta_{b_{rec}c_{MC}}$). Figure 5.12 shows the distribution of the cosine of these angles, versus each other. The figures shown here correspond to the $b$-jet, with second highest $b$-tag, in the left handed polarizatoin case.

For the purpose of defining the mis-taging, this figure is sub-divided into three parts, depending on the comparison of cosine of two angles, and later on putting a cut on the value of $\cos(\theta_{b_{rec}c_{MC}})$ . For convenience, three subdivisions are shown individually, in figure 5.13.

Figure contains three plots corresponding to following scenarios.

- First plot from left, contains events where $\cos(\theta_{b_{rec}c_{MC}})$ is bigger than $\cos(\theta_{b_{rec}b_{MC}})$, implying that the reconstructed $b$-jets is closer to the $c$ quark in generated sample, as compared to $b$ quarks.

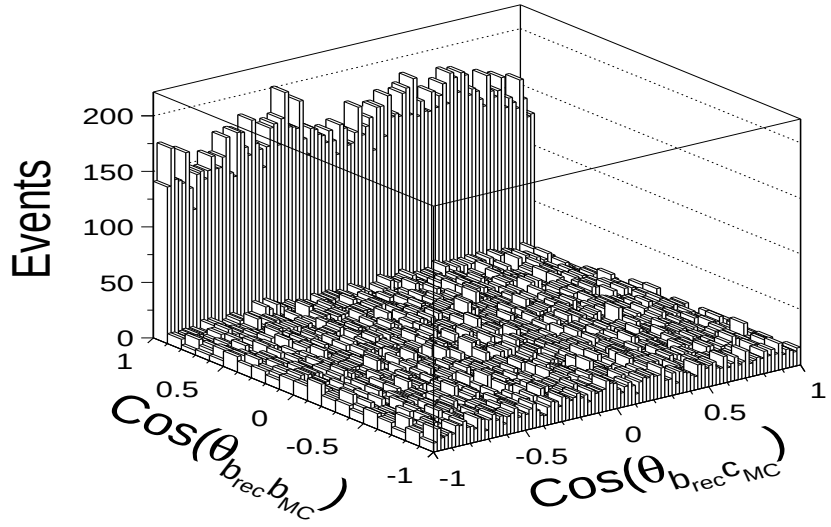


FIGURE 5.12: The *cosine* of the angle between reconstructed $b$-jets and generated $b$, $c$ quarks. Most of the reconstructed $b$-jets are closer to the generated $b$ quarks.

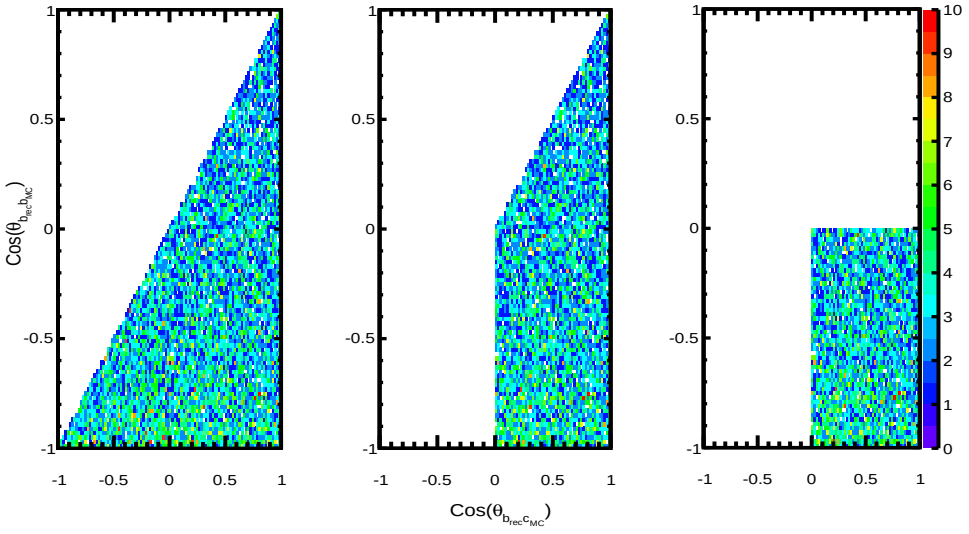


FIGURE 5.13: Subdivisions of figure 5.12. The figures correspond to three scenarios. Left: $\theta_{b_{rec}c_{MC}} < \theta_{b_{rec}b_{MC}}$, Center: $\theta_{b_{rec}c_{MC}} < \theta_{b_{rec}b_{MC}}$ and $\theta_{b_{rec}c_{MC}} < \pi/2$, and Right: $\theta_{b_{rec}c_{MC}} < \theta_{b_{rec}b_{MC}}$, $\theta_{b_{rec}c_{MC}} < \pi/2$, and $\theta_{b_{rec}b_{MC}} > \pi/2$.

– The plot in centre show the same, except for a cut, asking for $\theta_{b_{rec}c_{MC}}$ less than $\pi/2$.

– Right-most plot contains the events where the reconstructed $b$-jet is away from the generated $b$ quark by more than $\pi/2$, while it is closer to the generated $c$ quark,

by less than $\pi/2$. Events in this plot are recognized as $c$-jets, mistagged as $b$-jets (Quadrant 4).

The fraction of events corresponding to each of these plots, are shown in table 5.4 for both polarizations and both $b$-jets. In the table, the $b$-jet with the highest b-tag value is shown as Jet1, and the jet with second highest b-tag is called Jet2.

| Angle | Events Jet1 (%) All | Events Jet1 (%) Above b-tag 0.3 | Events Jet2 (%) All | Events Jet2 (%) Above b-tag 0.3 |
|---|---|---|---|---|
| **left-handed Polarization** ($e^-_L e^+_R$) | | | | |
| $\theta_{b_{rec}c_{MC}} < \theta_{b_{rec}b_{MC}}$ | 12 | 11 | 13 | 8 |
| $\theta_{b_{rec}c_{MC}} < \theta_{b_{rec}b_{MC}}$ $\theta_{b_{rec}c_{MC}} < \pi/2$ | 8 | 8 | 9 | 6 |
| $\theta_{b_{rec}c_{MC}} < \theta_{b_{rec}b_{MC}}$ $\theta_{b_{rec}c_{MC}} < \pi/2$ $\theta_{b_{rec}b_{MC}} > \pi/2$ | 6 | 6 | 6 | 4 |
| **right-handed Polarization** ($e^-_R e^+_L$) | | | | |
| $\theta_{b_{rec}c_{MC}} < \theta_{b_{rec}b_{MC}}$ | 12 | 11 | 12 | 8 |
| $\theta_{b_{rec}c_{MC}} < \theta_{b_{rec}b_{MC}}$ $\theta_{b_{rec}c_{MC}} < \pi/2$ | 8 | 8 | 9 | 6 |
| $\theta_{b_{rec}c_{MC}} < \theta_{b_{rec}b_{MC}}$ $\theta_{b_{rec}c_{MC}} < \pi/2$ $\theta_{b_{rec}b_{MC}} > \pi/2$ | 5 | 5 | 6 | 4 |

TABLE 5.4: Percentage number of events, as shown in the figure 5.13, for both polarizations.

From this study, it is concluded that 4-6 % of the $b$-jets are mistagged $c$-jets. It is seen that requirement of the $b\text{-}tag > 0.3$ helps to reject the mis-tagged events, more in the case of second $b$-jet than the first jet. It is also observed that the effect is almost independent of the polarization.

A part of $b$-jets could be indeed very close to the $c$-jets, making it difficulat to separate the two. For example, the distribution of the *cosine* of the angle, between generated $b$ and $c$ quarks is shown in left part of figure 5.14. Some of the $b$ quarks are very close to the $c$ quarks, which will be difficult to separate. The other reasons, for mis-tagging could be the soft $b$-jets and hard gluons, emitted by the $b$-jets. The hard radiations alter the direction of $b$ quarks. A distribution of the angle between two generated $b$ quarks, is shown in the right part of figure 5.14. Although, most of the $b\bar{b}$ pairs, are back to back, or close to that, there is a long tail, showing the comparatively small angles between $b$ and $\bar{b}$ quarks.

## 5.11 Identification of top quarks

For the association of the $b$ jets $b_1$ and $b_2$ having charge $Q_{b_1}$ and $Q_{b_2}$ to $t$ or $\bar{t}$ the event charge $C = Q_{b_1} - Q_{b_2}$ is defined. The Fig. 5.15 shows the distribution of the event charge.

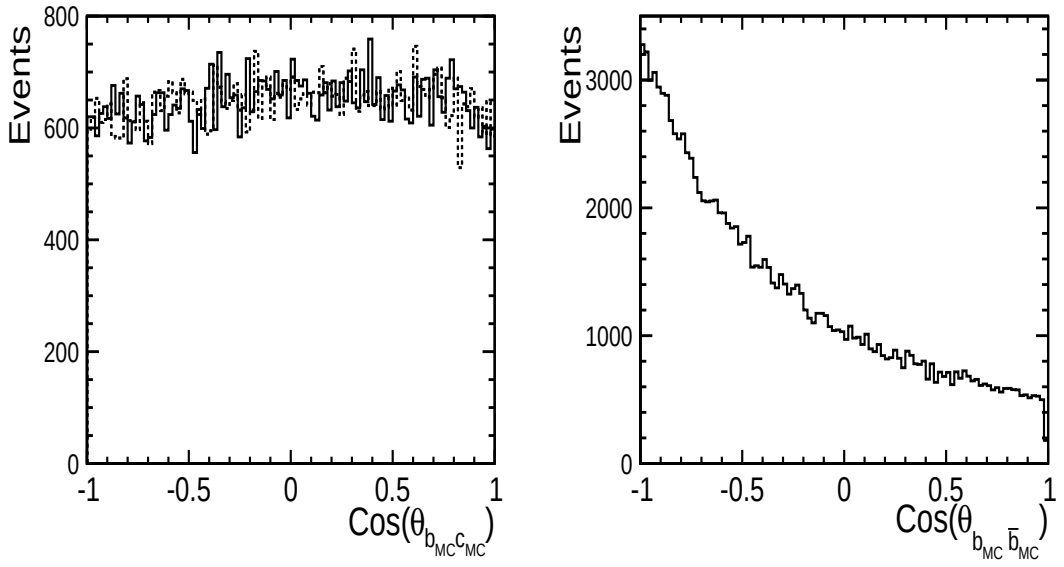


FIGURE 5.14: Left: The distribution of *cosine* of the angle between generated $b$ and $c$ quarks (solid line), and $\bar{b}$ and $c$ quarks ( dotted line). Right:. Thh distribution of *cosine* of the angle between generated $b$ and $\bar{b}$ quarks.

1179 As expected, most of the events have a non-zero $C$ value, which in turn implies that we can distinguish between a $t$ quark and a $\bar{t}$ quark. The following criteria are applied

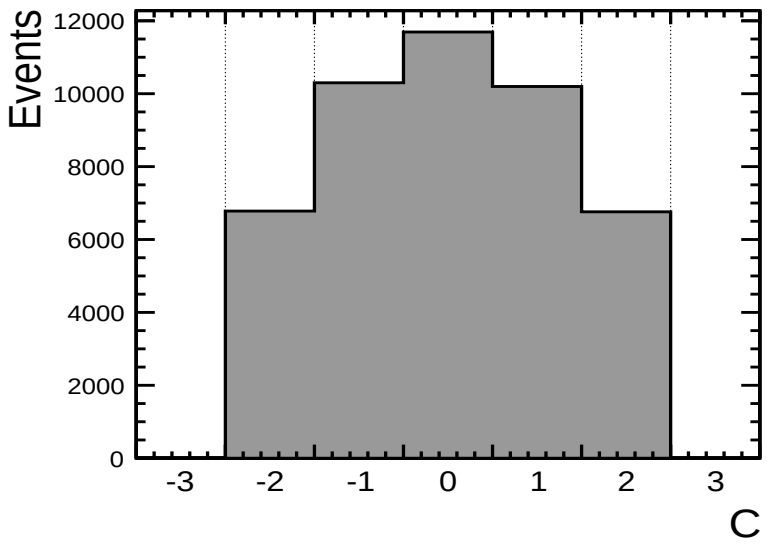


FIGURE 5.15: Event Charge $C = Q_{b_1} - Q_{b_2}$, the variable used to identify the charge of top quark.

1180

1181 – In case $C = 0$ an event is discarded;

- If $C < 0$ the $b_1$ is assumed to be produced in the decay of a $t$ quark;
- If $C > 0$ the $b_1$ is assumed to be produced in the decay of a $\bar{t}$ quark.

For the signal events, the further cuts are applied, in addition to the previously described cuts. One of the factors, that affects the purity is the wrong charge. The subtraction of events, where the charge is wrongly assigned, is done with the help of the MC events. For this purpose, the reconstructed bjets are compared with the bjets in MC events, by measuring the polar angle between the two. If the two jets do not satisfy the condition of $\cos(\theta) > 0.9$, the charge is assumed to be wrong. A distribution of cosine of the angle between $b$-jet and b partons in MC is shown in the figure 5.16. The reconstruction of direction works good for 60% events, while the remaining 40% events can be seen in the tail. One of the reasons for this long tail, and an imperfect reconstruction of the direction are the hard radiations. A b quark can radiate hard gluons, which can alter its direction. The change of direction is more significant if the $b$-jet has a low energy, which is particularly true for the right-handed polarization case.

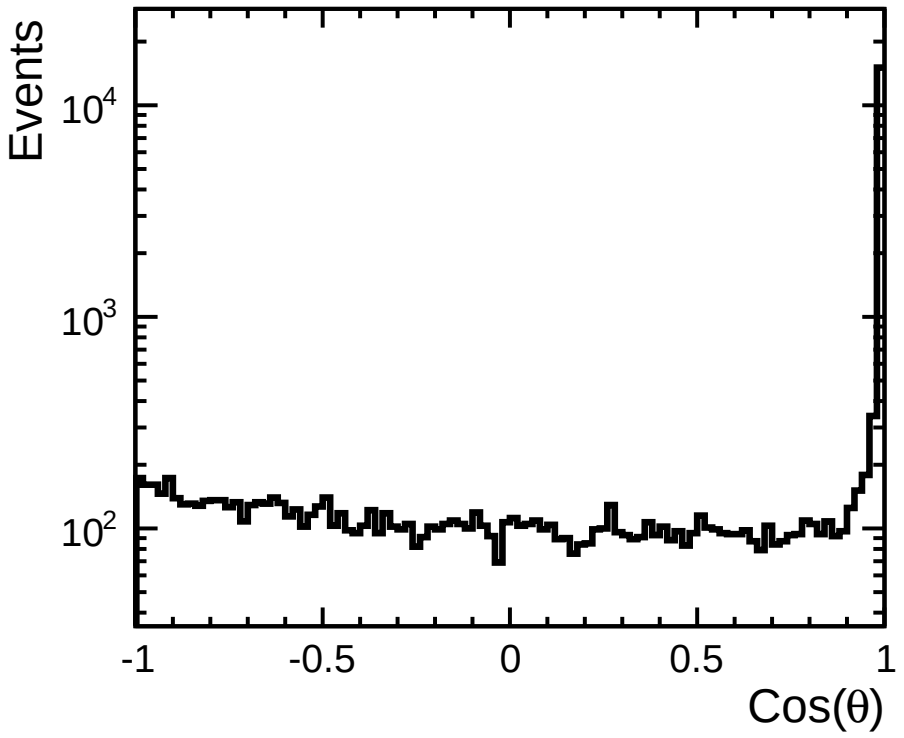


FIGURE 5.16: Cosine of the angle between reconstructed b jet and the Monte Carlo b jet. This parameter is used to identify the wrong charge assignments, and remove them.

The final selection efficiency, after subtraction of events with wrong charge, is 20% for left-handed electron beams, and 21.41% for the right-handed. This is in agreement with

1198 the one reported in [108]. The quality of reconstruction of top quarks, at the final stage,
1199 can be cross checked by comparing them to the top quarks at generator level. A difference
1200 of cosine of angle, of the reconstructed top quark, and the MC top quark is shown in
1201 figure 5.17.

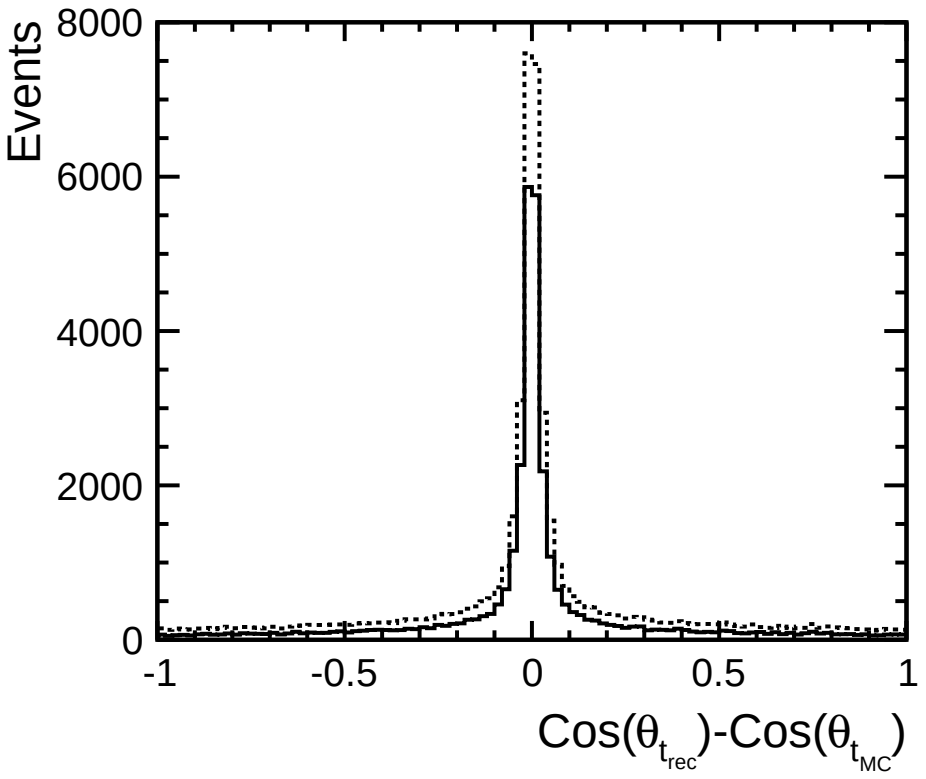


FIGURE 5.17: Difference in Cosine of angle between reconstructed and Monte Carlo $t$ quarks. The dotted line represented the number of quarks before the subtraction of events with wrong charge, while solid line shows the same after the correction.

## 1202 5.12 Determination of the forward backward asymmetry 1203 $\mathbf{A^t_{FB}}$

The forward backward asymmetry is defined as follows

$$A^t_{FB} = \frac{N(0 < \theta_{top} \leq \frac{\pi}{2}) - N(\frac{\pi}{2} < \theta_{top} \leq \pi)}{N(0 < \theta_{top} \leq \frac{\pi}{2}) + N(\frac{\pi}{2} < \theta_{top} \leq \pi)}$$

1204 The polar angle $\theta_{top}$ is defined w.r.t. to the incoming electron beam. The quantity $N$ is
1205 the number of events in the different detector hemispheres.

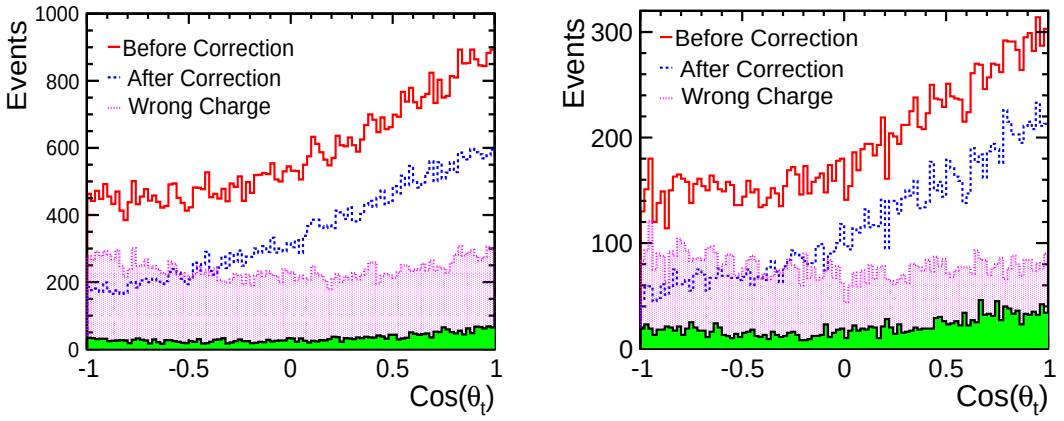


FIGURE 5.18: Left: Asymmetry for $P, P' = -1, +1$ after application of cuts in Tab. 5.2. The figure shows in addition the generated distribution and the events for which the $b$ quark charge is incorrectly reconstructed. The bottom fill shows the Standard Model background. Right: The same as left but for $P, P' = +1, -1$

A positive value of the asymmetry implies that the forward region of the detector is populated by the $t$ quarks, while there are more $\bar{t}$ in the other hemisphere. For convenience, the asymmetry is given for $t$ quarks only and the angle of $\bar{t}$ is inverted by $\pi$ to add it to the number of $t$ quarks.

$$\cos\theta_t = -1 * \cos\theta_{\bar{t}}$$

The Fig. 5.18 shows the forward backward asymmetry for the polarization $P, P' = -1, +1$ after the selection described in the previous section. A clear asymmetry is visible. The wrongly assigned charge of b quark, results in a lower asymmetry. They are shown in the bottom of Fig. 5.18.

For about 60% of the $t$ quarks the charge is measured correctly, depending on the various cut scenarios. For the final result events with wrong charge assignment are subtracted from the number of observed events. The resulting asymmetries for both beam polarizations are shown in Fig. 5.19 and the results are summarized in Tab. 5.6. Note, that 1/4 of the difference between generated and reconstructed $A^t_{FB}$ is taken as the systematic error. The error on the $A^t_{FB}$ is calculated as following:

$$\delta_{A_{FB}} = \sqrt{\frac{1 - A^2_{FB}}{N}} \tag{5.6}$$

Here, N is the number of events. The statistical error is shown for the number of events expected for $250\,\mathrm{fb}^{-1}$ and $P, P' = \pm 0.8, \mp 0.3$

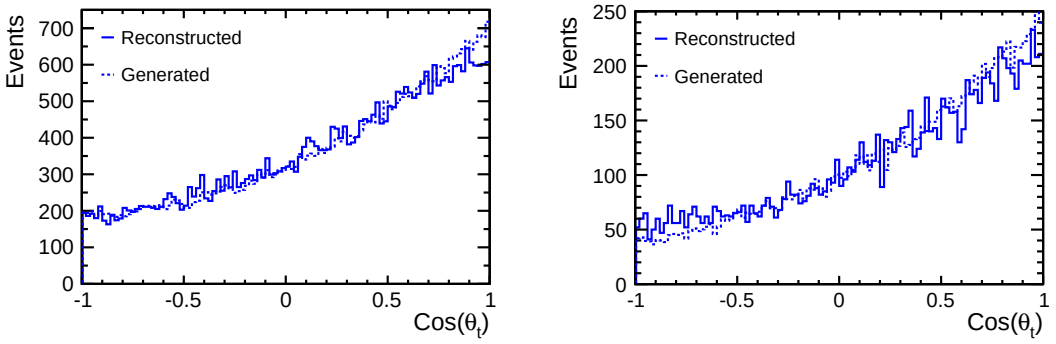


FIGURE 5.19: Left: Angular distribution of top quarks for $P, P' = -1, +1$ after application of cuts in Tab. 5.2 and correction for events in which the $b$ quark charge was incorrectly reconstructed. The corrected result is compared with the generated distribution. Right: The same as left but for $P, P' = +1, -1$

| $P, P'$ | $(A^t_{FB})_{gen.}$ | $A^t_{FB}$ | $\delta_{A_{FB}}$ | $(\delta_{A_{FB}}/A_{FB})_{stat.}$ [%] | $(\delta_{A_{FB}}/A_{FB})_{syst.}$ [%] |
|---|---|---|---|---|---|
| $-1, +1$ | 0.352 | 0.332 | 0.007 | 1.9 (corrected to $P, P' = -0.8, +0.3$) | 1.4 |
| $+1, -1$ | 0.439 | 0.388 | 0.009 | 2.01 (corrected to $P, P' = +0.8, -0.3$) | 2.9 |

TABLE 5.5: Precisions expected for $A^t_{FB}$ for different beam polarizations.

## 5.13 Form Factors

The precisions on the form factors, mentioned in 2.3, have been calculated using these results. Following four parameters are used to calculate the form factors.

- $\delta_\sigma(e^-_L e^+_R) = 0.40\%$
- $\delta_\sigma(e^-_R e^+_L) = 0.60\%$
- $\delta_{A_{FB}}/A_{FB}(e^-_L e^+_R) = 1.9\%$
- $\delta_{A_{FB}}/A_{FB}(e^-_R e^+_L) = 2.01\%$

While calculating the form factors, the CP violating form factors are fixed to their standard model values. The results for hadronic decay channel, are presented in the following table, along with semi-leptonic channel. For a comparison, the precisions expected from LHC, are also shown. The difference in the calculation method is that for LHC, only one form factor was allowed to vary at a time, while for calculations using our results for hadronic and semi-leptonic decay channels, two or four forms are allowed to vary simultaneously.

The $\gamma/Z$ mixing at a lepton collider allows to fix the sign of the form factors, while at the LHC, the top quark couples either to $\gamma$ or $Z$. This implies that the cross section $\sigma$ is

| Coupling | Standard Model value | LHC $\mathcal{L} = 300\, fb^{-1}$ | ILC (semi-leptonic) $\mathcal{L} = 500\, fb^{-1}$ $(P_{e^-}, P_{e^+}) = (\pm 0.8, \mp 0.3)$ | ILC (hadronic) $\mathcal{L} = 500\, fb^{-1}$ $(P_{e^-}, P_{e^+}) = (\pm 0.8, \mp 0.3)$ |
|---|---|---|---|---|
| $\Delta\tilde{F}^{\gamma}_{1V}$ | $-0.66$ | $^{+0.043}_{-0.041}$ | $\pm 0.002$ | $\pm 0.002$ |
| $\Delta\tilde{F}^{Z}_{1V}$ | 0.23 | $^{+0.240}_{-0.620}$ | $\pm 0.003$ | $\pm 0.003$ |
| $\Delta\tilde{F}^{Z}_{1A}$ | $-0.59$ | $^{+0.052}_{-0.060}$ | $\pm 0.006$ | $\pm 0.010$ |
| $\Delta\tilde{F}^{\gamma}_{2V}$ | 0.015 | $^{+0.038}_{-0.035}$ | $\pm 0.001$ | $\pm 0.001$ |
| $\Delta\tilde{F}^{Z}_{2V}$ | 0.018 | $^{+0.270}_{-0.190}$ | $\pm 0.002$ | $\pm 0.002$ |

TABLE 5.6: Precisions expected for different form factors, using semi-leptonic and hadronic decay channels of $t\bar{t}$, at $\sqrt{s} = 500\, GeV$, with polarized beams at the ILC. The same for the LHC, is also shown.

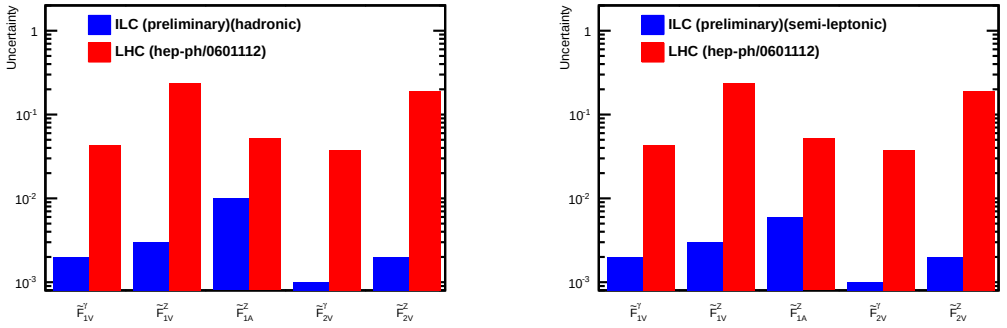


FIGURE 5.20: Left: A comparison of precisions for different form factors, for measurement of electroweak couplings of the top quark, at the ILC, using fully hadronic decay channel, and the LHC. Right: The same using semi-leptonic channel.

proportional to $(F^Z_{1V})^2 + (F^Z_{1A})^2$. Therefore the precisions expected at the LHC, cannot exclude the sign flip of the $F^Z_{1A}$ or $F^Z_{1V}$.

The results for both decay channels are consistent. The value of $\Delta F^i_2$ depend on the cross section, so there is no difference. $\Delta\tilde{F}^Z_{1A}$ is almost double as compared to the semi-leptonic channel, due the comparatively higher $\delta_{A_{FB}}/A_{FB}$ for the right-handed polarization in the hadronic decay channel. But this difference does not appear in $\Delta\tilde{F}_{1V}$ because the error on $A_{FB}$ for two polarizations is averaged in this case.

A graphic representation of these form factors is shown in figure 5.20.

## 5.14 Discussion of results

A major source of systematic error is that the final correction for wrongly measured $b$ quark charges is based on Monte Carlo truth information. This is one of the draw backs of this analysis scheme, as it would require a perfect modeling of the final state. However, the effect of systematics have been studied, by varying different cuts, on which the final measurement of the $A_{FB}$ depends.

The final results are shown to be robust against the $\chi^2$ cut. The final selection efficiency varies by 7%, while the purity varies by 2% only. The following table shows, the effect of variation of $\chi^2$, on purity and efficiency. Note that the values of $(\delta_{A_{FB}}/A_{FB})_{stat.}$ onwards, are corrected for luminosity 250 fb $^{-1}$.

| $\chi^2$ | $A^t_{FB}$ | $\delta_{A_{FB}}$ | $(\delta_{A_{FB}}/A_{FB})_{stat.}$ [%] | Purity [%] | Final Efficiency |
|---|---|---|---|---|---|
| **left-handed Polarization** $(e^-_L e^+_R)$ | | | | | |
| 30 | 0.332 | 0.007 | 1.9 | 59.42 | 20.02 |
| 20 | 0.333 | 0.008 | 1.9 | 60.60 | 16.00 |
| 15 | 0.330 | 0.008 | 2.06 | 61.68 | 13.37 |
| **right-handed Polarization** $(e^-_R e^+_L)$ | | | | | |
| 30 | 0.388 | 0.009 | 2.01 | 59.89 | 20.42 |
| 20 | 0.412 | 0.013 | 2.06 | 60.35 | 16.46 |
| 15 | 0.412 | 0.015 | 2.4 | 60.35 | 13.95 |

TABLE 5.7: Variation of the $\chi^2$ for two beam polarizations.

The effect of tightening the b-tag requirement is also studied. A tight cut on the b-tag, increases the purity by 4-5%, while decreasing the efficiency by the same amount. The numbers are given in the following table.

| b-tag$_{1,2}$ | $A^t_{FB}$ | $\delta_{A_{FB}}$ | $(\delta_{A_{FB}}/A_{FB})_{stat.}$ [%] | Purity [%] | Final Efficiency [%] |
|---|---|---|---|---|---|
| **left-handed Polarization** $(e^-_L e^+_R)$ | | | | | |
| 0.9,0.8 | 0.326 | 0.008 | 1.9 | 63.90 | 16.68 |
| **right-handed Polarization** $(e^-_R e^+_L)$ | | | | | |
| 0.9,0.8 | 0.390 | 0.013 | 2.17 | 63.85 | 16.80 |

TABLE 5.8: The purity is increased by tightening the cut on b-tag.

The major source of confusion in the charge measurement are the neutral $B$ hadrons. A zero jet charge makes the Event Charge $C$ biased as well, when combined with the other bjet charge. The studies showed that purity of the charge measurement varies for the values of Event Charge $C$, mainly because of this problem.

- $|C| = 1$, purity = 55.67 % , Efficiency = 8.46 %, for left-handed polarization, while $|C| = 1$, purity = 56.56% , Efficiency = 8.70 % for right-handed polarization.

– $|C| \geq 1$, purity = 62.53 %, Efficiency = 11.58 % in case of left-handed polarization, and $|C| \geq 1$, purity = 62.63 % , Efficiency = 11.70 %.

One of the outcomes of this aspect of the study was to propose further improvements in the LCFIPlus. Access to the Tertiary vertex will give a better control over precision in charge measurement. The $B^0$ mesons decay to $D$ mesons, which in turn decay to leptons. Measuring the charge of lepton will help to improve not only the efficiency, but also the purity. Using the muons for the vertex charge is easier, however the isolation of electrons, in a jet is a difficult task to accomplish.

The results are comparable to those obtained by using semi-leptonic channel [103]. The certainty of the charge measurement of a lepton is higher as compared to doing that for a bjet. The addition of the hadronic channel to the top quark pair decays studies adds to not only statistics, but also helps to calculate the total cross section. The relative error obtained in the hadronic channel is comparable with that in semi-leptonic. Following table shows a comparison of the numbers in both channels.

| Channel | $A^t_{FB}$ | $\delta_{A_{FB}}$ | $(\delta_{A_{FB}}/A_{FB})_{stat.}$ [%] | Final Efficiency [%] |
|---|---|---|---|---|
| **left-handed Polarization** $(e^+_L e^-_R)$ | | | | |
| hadronic | 0.332 | 0.007 | 1.9 | 20.02 |
| semi-leptonic | 0.326 | 0.005 | 1.7 | 28.5 |
| **right-handed Polarization** $(e^+_R e^-_L)$ | | | | |
| hadronic | 0.388 | 0.009 | 2.01 | 20.42 |
| semi-leptonic | 0.419 | 0.017 | 1.27 | 55.91 |

TABLE 5.9: A comparison of semi-leptonic and hadronic channels.

The performance for the right-handed polarization case, is better in case of semi-leptonic analysis, mainly because of the reason the semi-leptonic relies on the charge of lepton coming from the $W$ boson, which are more energetic in right-handed polarization electron beams case. The soft b-jets in this case lead to not only mis-identification of the charge, but also cause the problem for the reconstruction of kinematics, specially the direction of top quarks.

On the other hand, in the left-handed case, the performance is comparable, despite the lower efficiency in the case of hadronic decay channel. In this case, the reconstruction of the top quark direction is dominated by the bjets and Ws are comparatively less energetic. This leads to the migration effect, in semi-leptonic analysis. This problem is cured using the $\chi^2$ method, which has been detailed in [103].

The vertex charge measurement has also been applied to the semi-leptonic analysis, complementarily with the lepton charge. The application yields satisfactory results, and provides an alternative to the $\chi^2$ method used in that channel. It was found that the

method is equally efficient, and the statistical error obtained is the same as in hadronic decay channel. While using the b-jet charge method in the semi-leptonic channel, no corrections for the wrong charge assignments were made using the MC data. A cross check was performed using the charge of the lepton, only.

Another factor, limiting the efficiency, is that the LCFIPlus algorithm is not optimized for the charge measurement. One of the features of this is that while reconstructing the jet vertices, low $p_t$ tracks are dropped, without taking into consideration their effect on the total vertex charge. An improvement in the performance for the vertex charge will certainly help to improve the results.

The dedicated studies for mis-tagging of $c$-jets as $b$-jets, showed that around 5% of the $b$ jets were the mis-tagged $c$-jets. The reasons for this include the hard radiations, emitted by $b$ quarks. The treatment of these hard gluons, in the current versions of `Whizard`, could be improved in next versions. This will hopefully, provide a better performance for tagging the jets.

It is also proposed that the optimization of different cuts for two polarizations maybe done independently and could yield better results. One of the observation in this regard is the effect of tightening the b-tag cut, which effects the right-handed polarization more than the left-handed. Due to different kinematics in two cases, the kinematic cuts could also be differently applied to optimize the performance.

# Chapter 6

# Summary and outlook

The International Linear Collider is a proposed future electron positron collider, which will operate at a center-of-mass energy between 91 GeV and 500 GeV, later on extendable upto 1 TeV. ILC is proposed to have two detectors, namely International Large Detector (ILD), and Silicon Detector (SiD). This thesis is done in the framework of the ILD.

The thesis work can be summarized in two parts. The R & D project was aimed to optimize the Si-W Electromagnetic calorimeter's performance, which will be a subdetector of the ILD. The physics project was focused on analyzing the top quark production at the ILC.

## 6.1 The optimization of Si-W ECAL

The Si-W ECAL of ILC will consist of alternate Silicon and Tungsten layers. The silicon makes the active layers, while Tungsten acts as absorber material. Each silicon layers is divided into 4 wafers. The analysis focused on analyzing the performance of ECAL as a function of the guard ring size, an important component of the silicon wafers, used to prevent the current leakages. Several guard ring sizes ranging from 0 mm to 8 mm were studied, using two physics channels, namely the hadronic and leptonic decay of the Z boson. These are benchmark channels at the ILC, and of fundamental importance for many related studies. The precision available on the mass of Z boson, is used to calibrate the detectors.

Many final states at the ILC will consist of jets. The jets contain photons, which can disappear into inactive zones created by the guard rings, and therefore degrade the jet energy resolution of the ECAL. The studies for the hadronic decay channel, were carried out at the Z pole mass, with Z decaying to two quarks. The Z decay to electrons

$Z \rightarrow e^{-}e^{+}$ was studied for a center-of-mass energy of 250 GeV, in the Higgs-strahlung production. The channel $e^{-}e^{+} \rightarrow Zh$ will be used for the studies of the Higgs boson at the ILC. The model independent analysis of the properties of the Higgs boson make this channel a benchmark at the ILC.

The results for both the channels were consistent. Cross checks were performed during the analysis, to assure the quality of the analysis, with previously published results. The studies found that a guard ring size in range of 0-2 mm, does not degrade the energy resolution of the ECAL, significantly. The effect of the guard ring size, on the energy resolution of the ECAL, was studied as a function of the polar angle. It was found that the effect was independent of the position of the ECAL layers, in the detectors.

The results will be useful in future discussion with the manufacturers of the Silicon sensors for the ECAL. The studies are on going to analyze whether a guard ring is really needed to avoid the current leakages, or not. If needed, a guard ring of size upto 2mm, will not degrade the performance of the ECAL.

## 6.2 Forward-backward asymmetry in top quark pairs

The top quark is considered as a window to the new physics, due its distinguished properties like large mass, strong Yukawa couplings and link to the electroweak symmetry breaking. Measuring the electroweak couplings of the top quark, could hint at the existence of the new physics beyond Standard Model. The precise determination of these couplings is a benchmark at the ILC. In order to precisely measure the couplings, the forward-backward or left-right asymmetry of the top quark needs to be measured precisely. The hadronic decay channel was analyzed, using the vertex charge. The results of the study are part of the DBD[40].

Two beam polarization configurations $(P_{e^-}, P_{e^+}) = (-1, +1)$ and $(P_{e^-}, P_{e^+}) = (+1, -1)$ were studied at a center-of-mass energy of 500 GeV. Two parameters, cross section and the forward backward asymmetry were measured. Both are depend on the beam polarizations.

The 6-jet final states was analyzed using dedicated algorithms and full detector simulation. The identification of the top quarks was done by identifying the charge of the $b$ quark, at the vertex. The sum of the charge of all the tracks having a $p_t$ above 100 MeV, was taken as the vertex charge.

The final selection efficiency was 20% with a charge measurement purity of 60%. The statistical error on the cross section was estimated to be 0.40 % and 0.60% for the left-handed

and right-handed electron beam polarizations respectively. The relative statistical error $\delta A^t_{FB}/A^t_{FB}$ was found to be 1.9% for the left-handed electron beam configuration and 2.01% for the right-handed one. The systematic studies showed the robustness of the final results against the various selection cuts.

The analysis allowed for a full exploitation of the $t\bar{t}$ sample, and will help to calculate the total cross section. The precision on the form factors of the electroweak couplings, could be calculated more accurately, combined with the semi-leptonic results.

The prospect of vertex charge carries a lot of potential. The technique is also applied to the semi-leptonic analysis. The semi-leptonic analysis relies on the charge of the lepton, coming from the $W$ decay. In case of left-handed electron polarizations, the direction of the top quark is determined by the direction of the $b$ quark, which are comparatively more energetic. The use of vertex charge, could help to improve the performance.

Apart from the $t\bar{t}$ studies, the other charge measurements could also benefit from an improved measurement of the vertex charge. The benchmark process at the ILC include, 2 fermion processes, such as the hadronic decay of Z, and 4 fermion process such as $ZZ$ and $WW$. The hadronic decay of these bosons, can make use of the vertex charge.

# Appendix A

# Vertex Charge

We use the collection `RefindJets`, produced by the jet clustering algorithm. This collection contains the information on flavor tagging and other jet properties. The problem with this collection is that the jet charge is not well reconstructed. The algorithm drops some Particle Flow Objects (PFOs) for this collection, hence the charge values related to jets contained in this collection are not reliable.

On the other hand, the reliable information on the charge is contained in the collected `RefinedVertex`, which is `Vertex` type as an LCIO object, instead of being `ReconstructedParticle` type. The PID handler tool which acts to collect the information related to b-tag, does not work for the `Vertex` type object, therefore at the vertex, it is impossible to retrieve the information on b-tag value.

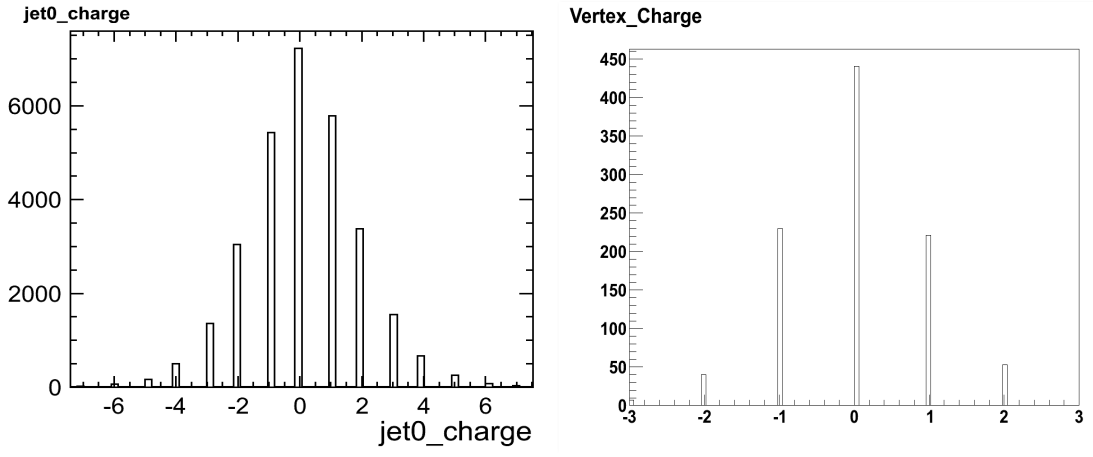


FIGURE A.1: Jet Charge vs Vertex Charge.

To sort this problem out, we use the `LCRelation` tool to pass from `RefinedJets` to `RefinedVertex` and vice versa. The LC Relation passed through another collection

which related jets to their vertices. The use of `LCRelation` in this way requires that we have credible information on the b-tag value of the jet under consideration. We use the cut $b - tag \geq 0.3$ at this stage, which is reasonably good as shown in figure 5.4.

A comparison of the charge of jets, as reconstructed from jets collection and vertex collection is shown in figure A.1.

# Bibliography


[1] S. L. Glashow.
Nucl. Phys 22(1961) 579
S. Weinberg.
Phys. Rev.Lett. 19(1967) 1264.

[2] J. Hasert *et al.*
1973 Phys. Lett. 46B 138-140.

[3] Makoto Kobayahi, Toshihide Maskwa.
Progress of Theoretical Physics Vol 49. Feb 1973.

[4] Nicola Cabibo.
Phys. Rev. Lett. 10 (1963) 531-533.

[5] S.L. Glashow.
Nuclear Physics, 22(4):579-588, 1961.

[6] S. Weinberg.
Physical Review Letters, 19(21):1264, 1967.

[7] A. Salam.
Elementary particle theory. Relativistic groups and analyticity.
Nobel Symposium. 1968

[8] Quantum Electrodynamics.
R.P. Feynman.

[9] A. Pich.
arXiv:hep-ph/9505231v1

[10] P. W. Higgs
Phys. Rev. Lett. 13, 508-509 (1964) .

[11] J. Iliopoulos.
arXiv:1305.6779v.

[12] K. A. Meissner, H. Nicolai
arXiv:hep-th/0612165

[13] N. Arkani-Hamed, S. Dimopoulos, G. Dvali.
arXiv:hep-ph/9803315.

[14] E. Bertuzzo, T. S. Ray, H. de Sandes, C. A. Savoy.
arXiv:1206.2623
L. Vecchi.
arXiv:1304.4579.

[15] K. Lane.
arXiv:hep-ph/0202255

[16] S. P. Martin.
arXiv:hep-ph/9709356.

[17] M. L. Perl.
SLAC-PUB-5937

[18] J. J. Aubert *et al.*
Phys. Rev. Lett. 33, 1404-1406 (1974).

[19] J. -E. Augustin *et al.*
Phys. Rev. Lett. 33, 1406-1408 (1974)

[20] L. M. Lederman,
Scientific American, October 1978, vol. 239, no. 4, pp. 72-80.

[21] J. H. Kuhn and G. Rodrigo.
arXiv:1109.6830[hep-ph]

[22] Oleg Brandt on behalf of the D0 collaboration arXiv:1209.4364v1[hep-ex]

[23] http://www-cdf.fnal.gov/physics/new/top/2009/tprop/Afb/cdfnote_9724_
public_v01.pdf

[24] J. Beringer *et al.* (Particle Data Group),
Phys. Rev. D86, 010001 (2012).

[25] CDF Collaboration.
Phys.Rev.Lett.74:2626-2631,1995. arXiv:hep-ex/9503002

[26] S. L. Glashow, J. Iliopoulos, L. Maiani.
Physical Review D, vol. 2, Issue 7, pp. 1285-1292

[27] R. Barate et al.
Phys. Lett., B565 (2003) 61-75.

[28] G. Degrassi *et al.*
arXiv:1205.6497v2.

[29] A. Juste *et al.*.
arXiv:hep-ph/0601112v2

[30] D0 Collaboration (S. Abachi et al.) [CDF Collaboration]
Phys.Rev.Lett. 74 (1995) 2632-2637
arXiv:hep-ex/9503003

[31] M. W. Grunewald and A. Gurtu.
http://pdg.lbl.gov/2010/reviews/rpp2010-rev-w-mass.pdf

[32] J. Beringer *et al.*
Phys. Rev. D86, 010001 (2012).
http://pdg.lbl.gov/2012/listings/rpp2012-list-z-boson.pdf

[33] M. Baaka, R. Kogle.
arXiv:1306.0571[hep-ph]

[34] S. Dimpoulos, H. Georgi.
Nuclear Physics B193 (1981) 150-162.

[35] Observation of a new boson at a mass of 125 GeV with the CMS experiment at the LHC.
Physics Letters B, Volume 716, Issue 1, 17 September 2012, Pages 30-61. arXiv:1207.7235[hep-ex]

[36] Observation of a new particle in the search for the Standard Model Higgs boson with the ATLAS detector at the LHC.
Physics Letters B, Volume 716, Issue 1, 17 September 2012, Pages 1-29. arXiv:1207.7214[hep-ex]

[37] M. Baak, R. Kogler (for the Gfitter group).
arXiv:1306.0571v2

[38] E. Ambler, R. W. Hayward, D. D. Hoppes, and R. P. Hudson
Phys. Rev. 105, 1413-1415 (1957)

[39] Carl R. Schmidt .
arXiv:hep-ph/9504434

[40] The International Linear Collider. Technical Desgin Report

[41] ATLAS Collaboration.
arXiv:1305.2756

[42] Michael E. Peskin.
SLAC-PUB-15178.

[43] OPAL Collaboration.
arXiv:hep-ex/0209076v1

[44] DELPHI Collaboration.
arXiv:hep-ex/0403041v1

[45] A. Djouadi,G. Moreau,F. Richard, and R. K. Singh.
PHYSICAL REVIEW D 82, 071702(R) (2010)

[46] Y. Hosotani and M. Mabe.
Physics Letters B, 615(3-4):257-265, 2005.

[47] Y. Cui, T. Gherghetta, and J. Stokes.
Journal of High Energy Physics, 2010(12):1-21, 2010.

[48] M. Carena, E. Ponton, J. Santiago, and C.E.M. Wagner.
Nuclear Physics B, 759(1-2):202-227, 2006.

[49] L. Randall and R. Sundrum.
Phys.Rev. Lett. 83, 3370 (1999) [hep-ph/9905221].

[50] L. Randall and R. Sun drum.
[hep-th/9906064]

[51] Filimon Gournaris. 01-04-2008. IoP HEPP Annual Meeting, Lancaster University.
http://indico.cern.ch/getFile.py/access?contribId=14&sessionId=
12&resId=0&materialId=slides&confId=27799

[52] J. Fleischer *el al.*
arXiv:hep-ph/0302259v1

[53] Ikematsu *et al.*
Phys.Rev.D84:014033,2011 arXiv:1104.5132

[54] H. Tabassam, Victoria Martin.
arXiv:1202.6013v1[hep-ex]

[55] Tony Price *et al.*
LC-REP-2013-004.
http://www-flc.desy.de/lcnotes/notes/LC-REP-2013-004.pdf

[56] M. Klute *et al.*
arXiv:1301.1322[hep-ph].

[57] S. Alekhin *et al.*
arXiv:1207.0980[hep-ph]

[58] K. W. Robinson.
Physical Review, Volume 111, Number 2. July 15 1958.
http://ab-abp-rlc.web.cern.ch/ab-abp-rlc/AP-literature/Robinson-1958.pdf

[59] M. Aicheler *et al.*
http://project-clic-cdr.web.cern.ch/project-clic-cdr/CDR_Volume1.pdf

[60] SiD Detector Outline Document.
http://hep.uchicago.edu/~oreglia/siddod.pdf

[61] http://ilcild.org/

[62] International Linear Collider.
Reference Design Report.
http://ilcdoc.linearcollider.org/record/6321/files/ILC_RDR_Volume_3-Accelerator.pdf

[63] The International Large Detector. Letter of Intent.
http://ilcild.org/documents/ild-letter-of-intent/LOI/20Feb2010.pdf

[64] The International Large Detector.
Detector Baseline Design (DBD).
https://svnsrv.desy.de/baswebsvn/wsvn/General.ilddbd/tags/V00-01/ilddbd/ILD-master.pdf

[65] W. Li *et al.*
http://accelconf.web.cern.ch/accelconf/IPAC2012/papers/tuppr042.pdf

[66] M. A. Thomson.
Nucl. Instr and Meth. A611 (2009) 25-40. arXiv:0907.3577

[67] M.A. Thomson.
http://www.hep.phy.cam.ac.uk/~thomson/publications/hsw06.pdf

[68] J-C Brient and H. Videau
:arXiv:hep-ex/0202004

[69] The CALICE Collboration.
arXiv:1105.3417v3

[70] CMS PAS PFT-10-002.
http://cms-physics.web.cern.ch/cms-physics/public/PFT-10-002-pas.pdf

[71] F. Beaudette. CMS Collaboration.
http://cds.cern.ch/record/1319088

[72] I. Valin, C. Hu-Guo, J. Baudot, G. Bertolone, A. Besson, et al.
JINST 7 (2012) C01102.
http://iopscience.iop.org/1748-0221/7/01/C01102/pdf/1748-0221_7_01_C01102.pdf

[73] E. Kato *et al.*
arXiv:1202.3017v1

[74] J. Velthuis *et al.*
Nucl. Instrum. Meth. **A579** (2007) 685-89.

[75] D. J. Jackson, D. Su, F. J. Wickens.
SLAC-PUB-13025. http://www.slac.stanford.edu/cgi-wrap/getdoc/slac-pub-13025.pdf

[76] https://twiki.cern.ch/twiki/bin/view/CALICE/WebHome

[77] CALICE Collaboration.
arXiv:0805.4833

[78] CALICE Collaboration.
arXiv:0811.2354

[79] J. Rouene.
http://ilcagenda.linearcollider.org/getFile.py/access?contribId=50&sessionId=10&resId=0&materialId=slides&confId=5468

[80] M. Reinhard, J. C. Brient. arXiv:0902.3042v1

[105] D. Bailey *et al.*
Nucl. Instrum. Meth. A610 (2009) 573-589. arXiv:0908.3019

[82] M. Cacciari, G. P. Salam.
Phys. Lett. B 641:57-61, 2006. arXiv:hep-ph/0512210

[83] P. Schade, J. Kaminski.
Nuclear Instruments and Methods in Physics Research **A628(2011)** 128-132.

[84] The CALICE Collaboration.
JINST 7 (2012) P09017 arXiv:1207.4210v2

[85] International Linear Collider. www.linearcollider.org. www.ilcild.org/

[86] CALICE Collaboration.
http://twiki.cern.ch/twiki/bin/view/CALICE/WebHome

[87] M.S. Amjad.
CALICE Collaboration Meeting, Casablanca, Morocco. 2010.

[88] T. H. TRAN.
Presentation at LCWS12. 2012.

[89] V. Mishra *et al.*
PRAMANA journal of physics. Vol. 65, No. 2. August 2005 pp. 259-272.
http://www.ias.ac.in/pramana/v65/p259/fulltext.pdf

[90] Naomi van der Kolk.
Publication in progress.

[91] Y. L. Dokshitzer,
Contribution cited in Report of the Hard QCD Working Group,
Proc. Workshop on Jet Studies at LEP and HERA, Durham,
December 1990, J. Phys. G17 (1991) 1537.

[92] S. Catani, Y. L. Dokshitzer, M. Olsson, G. Turnock, B. R.Webber.
Phys. Lett. B269 (1991) 432-438.

[93] PYTHIA 6.4 Physics and Manual.
T. Sjostrand, S. Mrenna, P. Skands.
arXiv:hep-ph/0603175.

[94] EUDET-Memo-2009-13.
P. Sicho et al.
http://www.eudet.org/e26/e28/e42441/e68274/EUDET-MEMO-2009-13.pdf

[95] CALICE Collaboration
arXiv:0805.4833v2[physics.ins-det]

[96] CALICE Collaboration
arXiv:0811.2354[physics.ins-det]

[97] P. de Freitas et al.
http://polzope.in2p3.fr:8081/MOKKA.

[98] ILCSOFT
http://ilcsoft.desy.de/portal

[99] Letter of intent. 2009.
http://ilcild.org/documents/ild-letter-of-intent.

[100] Hengne Li. 2009
http://tel.archives-ouvertes.fr/tel-00430432/fr/

[101] M. A. Thomson,
ZFinder: A Marlin processor for Bremsstrahlung recovery., (2009)

[102] R. Cornat.
Nuclear Science Symposium Conference Record. NSS'08 IEEE (2008).

[103] M.S. Amjad *et al.*,
arXiv:1307.8102

[104] K. Lannon, F. Margaroli and C. Neu,
arXiv:1201.5873v1[hep-ex]

[105] D. Bailey *et al.*
Nucl. Instrum. Meth. A610:573-589,2009. arXiv:0908.3019

[106] T. Han.
arXiv:hep-ph/0508097v1

[107] G. Moortgat-Pick *et al.*
Phys.Rept.460:131-243,2008 arXiv:hep-ph/0507011.

[108] Katsumasa Ikematsu *et al.*
arXiv:1005.4635v1[hep-ex]

[109] W. Kilian, T. Ohl, and J. Reuter,
Eur. Phys. J. **C21** (2011) 1742,
arxiv:0708.4233

[110] M. Moretti, T. Ohl, and J. Reuter.
arxiv:0102195.

[111] D. J. Jackson.
Nucl. Instrum. Meth. A 388 (1997) 247.

[112] T. Schwarz *et al.*, [CDF Collaboration], CDF-Note 10584,
http://www-cdf.fnal.gov/physics/new/top/2011/AfbComb/Afb_combo_5invfb.pdf

[113] V. M. Abazov *et al.* [D0 Collaboration],
Phys. Rev. D **84**, 112005 (2011) arXiv:1107.4995[hep-ex].

[114] CMS Collaboration, Physics Analysis Summary CMS-PAS-TOP-11-30 (2011).

[115] ATLAS Collaboration, ATLAS-CONF-2011-106 (2011).

[116] M. I. Gresham, I. -W. Kim and K. M. Zurek,
Phys. Rev. D **85**, 014022 (2012) arXiv:1107.4364[hep-ph].

[117] J. A. Aguilar-Saavedra,
arXiv:1202.2382v1[hep-ph].

[118] S. J. Brodsky and X. -G. Wu,
Phys. Rev. Lett. **109**, 042002 (2012) arXiv:1203.5312[hep-ph].

[119] M.S. Amjad *et al.*, LC-REP-2013-007,
http://www-flc.desy.de/lcnotes/notes/LC-REP-2013-007.pdf.

[120] P. Doublet.
PhD-Thesis Université de Paris XI.
LAL, LAL 11-222 (2011).

[121] P. Doublet, F. Richard, R. Poschl, T. Frisson and J. Rouene.
arXiv:1202.6659[hep-ex].